Structure and dynamics of fibrous calcium caseinate gels studied by neutron scattering

Tian, Bei

DOI

10.4233/uuid:90ed83af-4eca-45bc-af1a-816db85814d9

Publication date
2020

Document Version
Final published version

Important note
To cite this publication, please use the final published version (if applicable).
Please check the document version above.

STRUCTURE AND DYNAMICS OF FIBROUS CALCIUM CASEINATE GELS STUDIED BY NEUTRON SCATTERING

STRUCTURE AND DYNAMICS OF FIBROUS CALCIUM CASEINATE GELS STUDIED BY NEUTRON SCATTERING

Proefschrift

ter verkrijging van de graad van doctor
aan de Technische Universiteit Delft,
op gezag van de Rector Magnificus prof. dr. ir. T. H. J. J. van der Hagen,
voorzitter van het College voor Promoties,
in het openbaar te verdedigen op
maandag 27 januari 2020 om 15.00 uur

door

Bei TIAN

Master of Science in Food Technology,
Wageningen University, Wageningen, the Netherlands,
geboren te Beijing, China.

Dit proefschrift is goedgekeurd door de

Promotor: Prof. dr. C. Pappas & dr. W. G. Bouwman

Samenstelling promotiecommissie:

Rector Magnificus,   voorzitter
Prof. dr. C. Pappas,   Technische Universiteit Delft, promoter
Dr. W. G. Bouwman,   Technische Universiteit Delft, promoter

Onafhankelijke leden:
Prof. dr. K. Edler,   University of Bath
Prof. dr. L. Ahrné,   University of Copenhagen
Prof. dr. H. T. Wolterbeek,   Technische Universiteit Delft
Dr. V. García-Sakai,   ISIS Neutron and Muon Source

Overigelid:
Prof. dr. A. J. van der Goot,   Wageningen Universiteit

Reservelid:
Prof. dr. E. H. Brück,   Technische Universiteit Delft

Understand what I've become, it was not my design.

The Cranberries

CONTENTS

1

INTRODUCTION

By 2050, global demand for livestock products is estimated to increase by 70% to feed a population reaching 9.6 billion [1]. While livestock products provide highly nutritious food, they also have a negative impact on environmental resources. The livestock sector uses the world's largest agricultural land and is largely responsible for climate change [1]. As a result, measures need to be taken to mitigate human impact on the environment without jeopardizing food security. Besides adapting to a more sustainable animal production approach, promoting transition from a meat to a plant-based protein diet is another viable, long term solution [2].

People show a higher acceptance to meat analogues of structural resemblance to meat muscle fibres. This is likely due to their familiarity with the structure, together with the fact that it fits in with the meal formats [3, 4]. A structural resemblance presumes that the meat analogue contains fibres with a hierarchical and anisotropic structure. Given that this is the key to promoting a plant-based protein diet, much attention is paid to the making and characterisation of the fibre-like structure. Such research can on the one hand help to distinguish optimal product properties, and on the other hand shed light on the mechanism of structure formation in a meat analogue.

Soy protein is probably the most commonly used and studied meat analogue ingredient. It can be texturized through extrusion [5–7], spinning [8–10] or simple shear flow [11–13]. As promising as it sounds, texturizing soy protein alone would only result in an isotropic structure [14]. One or more additional phases, such as polysaccharides [13, 15] or gluten [14], are needed to introduce an anisotropic structure, thus suggesting the necessity of a multiphase system. Even though soy protein is a popular and preferred meat analogue ingredient, the resultant structure has two drawbacks, which renders it less suitable as a research subject. One is that the fibrous structure is only present at a millimetre length scale [16]. A lack of hierarchical structure may undermine the texture and consequently the chewing experience. The other drawback is that since the system is multi-phased, it is likely to bring in more complexity and pose more challenges to the understanding of

1

fibre formation.

Instead of using soy protein, this study approaches the mechanism of fibre formation from another perspective, which is to study the fibrous structure made from calcium caseinate. Its resultant structure has three prominent features that differentiate it from other meat analogue candidates. The first distinction is that calcium caseinate can form a pronounced anisotropic structure [17] at a condition that is milder and less energy consuming than it is required for soy protein. The second distinction is that unlike soy protein which needs an additional ingredient to form the multiphase, the dispersed phase in calcium caseinate gels is air bubbles, which makes the system, to a certain extent, simpler. The last and most significant distinction is that the fibres in calcium caseinate possess a hierarchical structure which prevails from nanometres to millimetres. Thus, even though calcium caseinate is in essence very different from soy protein, the knowledge gained from studying its fibrous structure can be transferred to other systems and provide valuable insight into the design of plant-based meat analogues with more pronounced anisotropic structures.

So far, the anisotropy of the fibres has been characterised by two techniques: tensile tests and scanning electron microscopy (SEM). In tensile test, the degree of anisotropy can be represented by a series of mechanical properties, calculated as the quotient of the fracture stress or fracture strain or Young's modulus between sample fractured parallel and perpendicular to the shear flow direction [17–19]. While this method quantifies the anisotropy macroscopically, it is inadequate to predict the fibre anisotropy at the microscopic scale. SEM shows that the protein aggregates indeed align at the nanometre length scale. However, since the area being probed is very small, the representativeness of the results is in doubt. Moreover, given the samples went through a series of pre-treatments before being imaged, it is possible that artefacts are induced during the process and being misinterpreted as protein alignment. As a result, the two techniques are insufficient and new methods are in need to quantify the degree of anisotropy of the fibres at the micro-scale.

The technique of small angle scattering (SAS) can be particularly powerful when it comes to the characterisation of structure at a sub-micron length-scale. It has been applied to many soft matter systems and provided valuable results [20–25]. A few of them are dedicated to the structure of casein micelles and sodium caseinate [26–30], but none is about the fibrous structure of calcium caseinate. The reason could be that SAS techniques are less known and less accessible to food scientists. Nevertheless, small angle neutron scattering (SANS) is considered as a suitable tool to offer insights into the structure of calcium caseinate. The degree of anisotropy can be obtained through analysing the 2D scattering patterns. Moreover, it is a non-invasive technique, the beam covers a fair amount of sample area and the measurement time is reasonably short, it takes around 10-20 min to measure one sample.

Besides SANS, there are many other neutron techniques that can share information about other aspects of a material. For instance, neutron reflectivity can be used to study the

kinetics and structure of thin films [31–33]; quasi-elastic neutron scattering (QENS) can access the dynamics of for example, protein powders [34–37]; and the spin-echo (SESANS) or ultra small angle neutron scattering (USANS) techniques are usually combined with SANS to provide information of the structure at a larger length scale [38–42]. The versatility of neutron techniques has thus extended the scope of this work to the characterisations of different aspects of calcium caseinate in different states.

The objective of this work is to study the sizes, structure and dynamics of calcium caseinate gels using a variety of neutron techniques. The outline is as followed. In chapter 2, the average size and deformation degree of the air bubbles dispersed in calcium caseinate gels are studied by the spin-echo small angle neutron scattering (SESANS) instrument, in combination with refractive microscopy and X-ray tomography; In chapter 3, the influence of D_2O and drying methods on the dynamics of calcium caseinate powders are studied by QENS; Chapter 4 proposes an anisotropic Guinier-Porod model which describes the anisotropic scattering from oriented objects. This chapter forms the basis for chapter 5, where the sizes, structure and extent of anisotropy of the fibres are studied. The results are further compared to those obtained from tensile tests and SEM, which show a good agreement of the anisotropy of the fibres at the micro- and macroscale. Lastly, chapter 6 summarises other experiments conducted during the course of this thesis, which have not yet turned into main findings, along with a discussion of the implication of this work.

1

REFERENCES

[1] *FAO's role in livestock and the environment,* http://www.fao.org/livestock-environment/en/, accessed: 2019-02-01.

[2] J. De Boer and H. Aiking, *On the merits of plant-based proteins for global food security: Marrying macro and micro perspectives,* Ecological Economics **70**, 1259 (2011).

[3] J. E. Elzerman, A. C. Hoek, M. A. Van Boekel, and P. A. Luning, *Consumer acceptance and appropriateness of meat substitutes in a meal context,* Food Quality and Preference **22**, 233 (2011).

[4] H. Schösler, J. De Boer, and J. J. Boersema, *Can we cut out the meat of the dish? Constructing consumer-oriented pathways towards meat substitution,* Appetite **58**, 39 (2012).

[5] J. Cheftel, M. Kitagawa, and C. Queguiner, *New protein texturization processes by extrusion cooking at high moisture levels,* Food Reviews International **8**, 235 (1992).

[6] S. Lin, H. Huff, and F. Hsieh, *Texture and chemical characteristics of soy protein meat analog extruded at high moisture,* Journal of Food Science **65**, 264 (2000).

[7] S. Lin, H. Huff, and F. Hsieh, *Extrusion process parameters, sensory characteristics, and structural properties of a high moisture soy protein meat analog,* Journal of Food Science **67**, 1066 (2002).

[8] E. W. Lusas and M. N. Riaz, *Soy protein products: processing and use,* The Journal of nutrition **125**, 573S (1995).

[9] H. Huang, E. Hammond, C. Reitmeier, and D. Myers, *Properties of fibers produced from soy protein isolate by extrusion and wet-spinning,* Journal of the American Oil Chemists' Society **72**, 1453 (1995).

[10] V. Rampon, P. Robert, N. Nicolas, and E. Dufour, *Protein structure and network orientation in edible films prepared by spinning process,* Journal of food science **64**, 313 (1999).

[11] G. A. Krintiras, J. Göbel, A. J. Van der Goot, and G. D. Stefanidis, *Production of structured soy-based meat analogues using simple shear and heat in a couette cell,* Journal of Food Engineering **160**, 34 (2015).

[12] K. J. Grabowska, S. Zhu, B. L. Dekkers, N. C. de Ruijter, J. Gieteling, and A. J. van der Goot, *Shear-induced structuring as a tool to make anisotropic materials using soy protein concentrate,* Journal of Food Engineering **188**, 77 (2016).

[13] B. L. Dekkers, C. V. Nikiforidis, and A. J. van der Goot, *Shear-induced fibrous structure formation from a pectin/spi blend,* Innovative Food Science & Emerging Technologies **36**, 193 (2016).

[14] K. J. Grabowska, S. Tekidou, R. M. Boom, and A.-J. van der Goot, *Shear structuring as a new method to make anisotropic structures from soy–gluten blends,* Food research international **64**, 743 (2014).

[15] B. L. Dekkers, R. Hamoen, R. M. Boom, and A. J. van der Goot, *Understanding fiber formation in a concentrated soy protein isolate-pectin blend,* Journal of Food Engineering **222**, 84 (2018).

[16] B. L. Dekkers, R. M. Boom, and A. J. van der Goot, *Structuring processes for meat analogues,* Trends in Food Science & Technology (2018).

[17] J. M. Manski, A. J. van der Goot, and R. M. Boom, *Formation of fibrous materials from dense calcium caseinate dispersions,* Biomacromolecules **8**, 1271 (2007).

[18] F. G. Evans, *Mechanical properties of bone* (Thomas Springfield:, 1973).

[19] M. M. Ak and S. Gunasekaran, *Anisotropy in tensile properties of mozzarella cheese,* Journal of food science **62**, 1031 (1997).

[20] G. Schmidt, A. I. Nakatani, P. D. Butler, and C. C. Han, *Small-angle neutron scattering from viscoelastic polymer- clay solutions,* Macromolecules **35**, 4725 (2002).

[21] A. Lopez-Rubio and E. P. Gilbert, *Neutron scattering: a natural tool for food science and technology research,* Trends in Food Science & Technology **20**, 576 (2009).

[22] K. M. Weigandt, D. C. Pozzo, and L. Porcar, *Structure of high density fibrin networks probed with neutron scattering and rheology,* Soft Matter **5**, 4321 (2009).

[23] K. M. Weigandt, L. Porcar, and D. C. Pozzo, *In situ neutron scattering study of structural transitions in fibrin networks under shear deformation,* Soft Matter **7**, 9992 (2011).

[24] B. I. Zielbauer, A. J. Jackson, S. Maurer, G. Waschatko, M. Ghebremedhin, S. E. Rogers, R. K. Heenan, L. Porcar, and T. A. Vilgis, *Soybean oleosomes studied by small angle neutron scattering (sans),* Journal of colloid and interface science **529**, 197 (2018).

[25] Y. Wang, B. Eastwood, Z. Yang, L. de Campo, R. Knott, C. Prosser, E. Carpenter, and Y. Hemar, *Rheological and structural characterization of acidified skim milks and infant formulae made from cow and goat milk,* Food Hydrocolloids **96**, 161 (2019).

[26] A. Shukla, T. Narayanan, and D. Zanchi, *Structure of casein micelles and their complexation with tannins,* Soft Matter **5**, 2884 (2009).

[27] A. Bouchoux, J. Ventureira, G. Gésan-Guiziou, F. Garnier-Lambrouin, P. Qu, C. Pasquier, S. Pézennec, R. Schweins, and B. Cabane, *Structural heterogeneity of milk casein micelles: a sans contrast variation study,* Soft matter **11**, 389 (2014).

[28] B. Ingham, A. Smialowska, G. D. Erlangga, L. Matia-Merino, N. Kirby, C. Wang, R. G. Haverkamp, and A. Carr, *Revisiting the interpretation of casein micelle saxs data,* Soft Matter **12**, 6937 (2016).

1

[29] A. Smialowska, L. Matia-Merino, B. Ingham, and A. Carr, *Effect of calcium on the aggregation behaviour of caseinates,* Colloids and Surfaces A: Physicochemical and Engineering Aspects **522**, 113 (2017).

[30] L. Day, J. Raynes, A. Leis, L. Liu, and R. Williams, *Probing the internal and external micelle structures of differently sized casein micelles from individual cows milk by dynamic light and small-angle x-ray scattering,* Food Hydrocolloids **69**, 150 (2017).

[31] B. Wallet, E. Kharlampieva, K. Campbell-Proszowska, V. Kozlovskaya, S. Malak, J. F. Ankner, D. L. Kaplan, and V. V. Tsukruk, *Silk layering as studied with neutron reflectivity,* Langmuir **28**, 11481 (2012).

[32] M. Campana, S. Hosking, J. Petkov, I. Tucker, J. Webster, A. Zarbakhsh, and J. Lu, *Adsorption of bovine serum albumin (bsa) at the oil/water interface: a neutron reflection study,* Langmuir **31**, 5614 (2015).

[33] T. Saerbeck, R. Cubitt, A. Wildes, G. Manzin, K. H. Andersen, and P. Gutfreund, *Recent upgrades of the neutron reflectometer d17 at ill,* Journal of Applied Crystallography **51**, 249 (2018).

[34] M. Bee, *Quasielastic neutron scattering: principles and applications in solid state chemistry,* Biology and Materials Science, Adam Hilger, Bristol , 193 (1988).

[35] D. Russo, J. Pérez, J.-M. Zanotti, M. Desmadril, and D. Durand, *Dynamic transition associated with the thermal denaturation of a small beta protein,* Biophysical journal **83**, 2792 (2002).

[36] J. Sjöström, F. Kargl, F. Fernandez-Alonso, and J. Swenson, *The dynamics of water in hydrated white bread investigated using quasielastic neutron scattering,* Journal of Physics: Condensed Matter **19**, 415119 (2007).

[37] C. S. Kealley, A. V. Sokolova, G. J. Kearley, E. Kemner, M. Russina, A. Faraone, W. A. Hamilton, and E. P. Gilbert, *Dynamical transition in a large globular protein: Macroscopic properties and glass transition,* Biochimica et Biophysica Acta (BBA)-Proteins and Proteomics **1804**, 34 (2010).

[38] R. H. Tromp and W. G. Bouwman, *A novel application of neutron scattering on dairy products,* Food Hydrocolloids **21**, 154 (2007).

[39] D. P. Kalman and N. J. Wagner, *Microstructure of shear-thickening concentrated suspensions determined by flow-usans,* Rheologica acta **48**, 897 (2009).

[40] A. J. Jackson and D. J. McGillivray, *Protein aggregate structure under high pressure,* Chemical Communications **47**, 487 (2011).

[41] R. M. Shah, J. P. Mata, G. Bryant, L. de Campo, A. Ife, A. V. Karpe, S. R. Jadhav, D. S. Eldridge, E. A. Palombo, and I. H. Harding, *Structure analysis of solid lipid nanoparticles for drug delivery: A combined usans/sans study,* Particle & Particle Systems Characterization **36**, 1800359 (2019).

[42] M. Mulder, X. X. Li, M. M. Nazim, R. M. Dalgliesh, B. Tian, M. Buijse, J. van Wunnik, and W. G. Bouwman, *Systematically quantifying oil–water microemulsion structures using (spin-echo) small angle neutron scattering,* Colloids and Surfaces A: Physicochemical and Engineering Aspects **575**, 166 (2019).

1

2

AIR BUBBLES IN FIBROUS CASEINATE GELS INVESTIGATED BY NEUTRON REFRACTION, X-RAY TOMOGRAPHY AND REFRACTIVE MICROSCOPE

Fibrous protein gels have the potential to form the basis for the next-generation of meat analogue. It is suggested that fibre anisotropy is related to air bubbles present in the gel. Given the complexity and heterogeneity of the sample, several quantitative techniques are needed to ensure a comprehensive understanding of the air bubbles. We conducted neutron refraction experiments to study the size and shape of the air bubbles in three calcium caseinate samples containing different H_2O to D_2O ratios. Refractive microscopy and X-ray tomography (XRT) analysis were performed on the same sample to provide complementary information. The degree of deformation and average width of the air bubbles were obtained from both the XRT and neutron refraction experiment. A neutron refraction model calculates the average area and volume of a single air bubble, which correspond to the largest area and volume fractions of all the air bubbles from the XRT analysis. Additionally, we found that the H_2O to D_2O ratio in the sample largely influences the size, number distribution and degree of deformation of the air bubbles. The neutron refraction technique can be a simple and complementary method to help understanding the role of air bubbles in meat analogues.

2.1. Introduction

Many food products can be seen as composite materials whose textures are determined synergistically by the fillers (dispersed phase) and the matrix (continuous phase) [2, 3]. For example, the viscoelastic properties of a dough change after the inclusion of air [4]; the hardness of a cheese increases with decreasing fat content [5], and the rheological and sensory properties of a chocolate rely on the subtle balance between sugar, cocoa butter and cocoa powder [6]. Characterizing the microstructure of the dispersed phase is crucial to understanding the macroscopic properties of the food product.

An interesting composite food material is a fibrous protein gel made of calcium caseinate [7, 8]. Since the fibrous structure resembles real meat, calcium caseinate is considered as a promising candidate for the next-generation meat analogue [9]. Air is the only dispersed phase in such a fibrous protein gel. It has always been present in different types of meat analogues [10, 11], but it was not until recent that its contribution to the fibres' mechanical properties was discussed [12]. The air bubbles are elongated along the shear rate direction and their maximum length correspond to the highest anisotropy index of the fibres. This suggests that characterising the air bubbles can provide complementary information on the anisotropy of the fibres. However, not many techniques are available for characterisation.

X-ray computed tomography (XRT) is a common and non-destructive technique used to study the size, shape and amount of air in composite materials [13–15]. The contrast in XRT comes from the absorption difference between the protein matrix and the air. XRT has been applied to demonstrate how gelatin peptide fortified the microstructure of frozen mousses against the freeze-thaw cycle [16], to evaluate the performance of different gluten [17] or gluten-free dough recipes [18], and to support a new preparation method for making a soy-protein based hydrogel [19, 20]. As powerful as XRT can be, a composite food system is inherently heterogeneous and complex [21], so no single technique is sufficient to provide a complete view of the sample. The drawbacks of XRT are the large datasets; possible imaging artefacts, and that the treatment of the raw data can depend on the operator [22–24]. To ensure a comprehensive and unbiased understanding of the sample, we need several quantitative approaches to characterize the air bubbles.

Neutron refraction is another suitable technique to study the air bubbles. It is performed by the Spin-Echo Small Angle Neutron Scattering (SESANS) instrument [25]. The SESANS instrument measures the change in neutron direction. This results in a decrease of the polarisation of the neutron beam. When the size of an object is small (e.g., up to a few micrometers), the change in polarisation is mainly due to the scattering of the object. The scattering depends on the dimensions of the scattering particle, the volume fraction and the scattering length density contrast. Thus, the size information is readily present in the measured depolarisation curve [26, 27]. This techniques has been applied to quantify the micro-structure of globular protein gels [28], to explain the mechanical properties of cross-linked casein micelles [29], and to compare the gel structure between curdling and acidified milk [30]. When the size of an object is large (e.g., over tens of mi-

crometers), neutrons passing through the object will be rather refracted than scattered [27, 31]. The amount of refraction depends on the geometry of the object instead of the size, so the size information is not directly visible in the detected signal. The neutron refractive index difference between the object and its surrounding matrix determines the contrast. Neutron refraction has been less explored than neutron scattering. To our knowledge, it has only been used in food-related research once, to characterise the number of layers in a fibrous structure made of soy protein isolate and gluten [32]. The fibre was approximated as infinitely long cylinders with a spread in orientation. However, the geometry of a fibre is very different from that of an elongated air bubble. As a result, another model is needed so that the information obtained from the neutron refraction technique is comparable to the others.

In this study, we demonstrated that a combination of neutron refraction, XRT and refractive microscopy add more certainty to a comprehensive understanding of the air bubbles dispersed in the fibrous calcium caseinate gel. To have different contrasts, we prepared three samples using 100% H_2O, 50%v/v H_2O+50%v/v D_2O and 100% D_2O. An improved model based on the microscopy images was proposed to fit the neutron refraction data. Parameters such as the degree of deformation, average width and orientation of the air bubbles can be extracted from the model, which agrees with the XRT results.

2.2. MATERIAL AND METHODS

2.2.1. MATERIALS
Roller dried calcium caseinate powder was provided by DMV International, Veghel, The Netherlands. The calcium caseinate powder contains 90%wt protein and 1.2%wt calcium according to the manufacturer's specification. Heavy water (deuterium oxide, D_2O, $\rho = 1.107$g/mL) with 99.9% deuterium was used(Sigma-Aldrich, Canada).

2.2.2. PREPARATION OF THE STRUCTURE
Protein premixes were prepared by manually mixing 30 g calcium caseinate powder with 70 g demineralized water (100% H_2O), 35 g demineralized water+38.9 g heavy water (50%v/v H_2O+50%v/v D_2O) or 77.7 g heavy water (100% D_2O). The premixes were transferred to a pre-heated (50°C), custom built shearing device (Wageningen University, the Netherlands). It consists of a rotating cone (the bottom cone, angle = 105°) and a stationary cone (the top cone, angle =100°). Both cones were thermostatted with a circulating water bath. More details are described in earlier publications [33, 34]. Well-defined shear flow was applied to the premixes with a rotating speed of 150 rpm at 50°C for 5 min. After processing, the samples were cooled to 4°C in 10 min before removal from the device. They were stored at −20°C for further analysis. Samples stored at this temperature have the closest mechanical properties as to the freshly made ones [35]. Two sets of samples were made for duplicate measurements.

2.2.3. NEUTRON REFRACTION
The effect of the refracted neutron is measured by the SESANS instrument at the neutron source in Delft University of Technology, the Netherlands [36]. The measurements were

done at room temperature. The principle of this instrument involves the Larmor precession of a polarised neutron beam in magnetic fields, where the angular deviations of the neutron trajectory due to scattering or refraction are encoded by the measured polarisation P. More details of the instrument are described in earlier publications [37, 38]. When the air bubble is small (e.g., up to a few μm), only elastic scattering contributes to the change in polarisation. However, when the air bubble is large (e.g., over tens of μm), refraction of the neutrons becomes the dominant cause of change in polarisation. The transition from scattering to refraction is continuous. For the cross-over region, we need more advanced theory, such as the phase-object approximation [26, 31], to calculate the angle distribution function. Nevertheless, we can estimate a size limit for this transition. It is calculated by the phase change of the neutron wave function when going through the air and protein interface. When the phase change is of the order of π, refraction becomes dominant [31]. The neutron wave phase change η is calculated as

$$\eta = \left| \frac{4\pi\delta R}{\lambda} \right| \tag{2.1}$$

where R is the radius of a sphere, λ is the wavelength of the neutron, the SESANS instrument in Delft uses thermal neutrons with a wavelength of 2.1 ± 0.1 Å, δ is the difference between the neutron refractive index and 1.

$$\delta = \frac{\Delta\mathrm{SLD}\cdot\lambda^2}{2\pi} \tag{2.2}$$

ΔSLD is the scattering length density contrast: it is the difference between the scattering length density (SLD) of the protein matrix and that of the air bubbles. For the samples made of 100% D_2O, its value is $5.02 \times 10^{14} \mathrm{m}^{-2}$, for the sample made of 50% v/v H_2O+50% v/v D_2O, ΔSLD $= 2.74 \times 10^{14} \mathrm{m}^{-2}$, and ΔSLD equals to $0.208 \times 10^{14} \mathrm{m}^{-2}$ for the sample made of 100% H_2O. Knowing λ and δ, we calculated the minimum air bubble size, and can be sure that refraction dominates the measured signal when the size is around 30μm.

The fibrous protein gels were prepared in their frozen state for optimal sample manipulation. They were cut into approximately $15 \times 12 \times 2.5$mm ($L \times H \times W$) pieces, where the length corresponds to the shear flow direction, the height corresponds to the vorticity direction and the width corresponds to the velocity gradient. Neutrons enter the sample along the velocity gradient with a beam size of 10×8mm. We define the direction of the neutron beam as the x-axis, and the direction perpendicular to the horizontal plane as the z-axis. To see the anisotropy of the air bubbles, the cut gel pieces were first placed with their lengths perpendicular to the xz-plane (Fig. 2.2B). We denoted this as the horizontal orientation. Afterward, the sample was rotated 90° along the yz-plane and measured with its length parallel to the z-axis. This will be further referred to as the vertical orientation.

The sample made of 100% H_2O was measured both as such and with solvent exchange using D_2O to increase the contrast. It was soaked in pure D_2O for 4 hours before the measurement and sealed in a quartz container filled with D_2O during the measurement.

2.2.4. X-RAY TOMOGRAPHY (XRT)

The samples were cut into approximately $7\times4\times3$mm ($L\times H\times W$) pieces, where the length corresponds to the shear flow direction, the height corresponds to the vorticity direction and the width corresponds to the velocity gradient. A GE Phoenix v|tomex|m tomographer (General Electric, Wunstorf, Germany) set at 80 kV/90 μA, was used to scan the samples at room temperature. The system contains two X-ray sources. The 240kV micro focus tube with tungsten target was employed. The images were recorded by a GE DXR detector array with 2024 × 2024 pixels (pixel size 200μm). The object and detector were located 28.55mm and 815mm from the X-ray source. This results in a spatial resolution of 7.00μm. A full scan consists of 750 projections over 360°. GE reconstruction software (Wunstorf, Germany) was used to calculate the 3D structure via back projection. The 3D images were analyzed using Avizo imaging software version 9.3.0. The area and volume fraction, average width as well as degree of deformation (DoD) of the air bubbles were calculated from the program. DoD is defined as the average of DoD_x and DoD_z, where

$$DoD_x = \frac{y-x}{y+x} \tag{2.3a}$$

$$DoD_z = \frac{y-z}{y+z} \tag{2.3b}$$

$$DoD = \frac{DoD_x + DoD_y}{2} \tag{2.3c}$$

Here, y is the length of a deformed air bubble parallel to the shear flow direction, x is the width of the air bubble parallel to the velocity gradient, and z is the height of the air bubble parallel to the vorticity direction. An illustration can be found in Fig. 2.2B.

2.2.5. REFRACTIVE LIGHT MICROSCOPY

The samples were imaged at room temperature, using a Digital Microscope (Keyence VHX-2000E) with a magnification of ×100 times.

2.3. THE REFRACTION MODEL

The refraction model is built based on the observation from the refractive microscopy pictures in Fig. 2.1. These show that the air bubbles are prolate spheroid-like. Hence we approximate the bubble as a spherocylinder which is a cylinder with spherical end caps. We could also do the analysis with elliptical shapes, where we expect similar descriptions of the signals, but the calculation with the spherocylinder is easier. The cross-section of the cylinder parallel to the neutron beam is assumed to be circular (which means the cylinder is perpendicular to the beam). This circular cross-section is confirmed by microscopy picture and 2D x-ray radiography, as presented in the supplementary information.

We present the expected polarisation due to the refraction of the air bubbles as Eq. 2.4, with a schematic illustration in Fig. 2.2. Suppose the protein slab is composed of n layers. Within each layer, the projected area fraction of the air bubbles is defined as α, so $1-\alpha$ represents the fraction of the non-refracting protein gel. The area fraction of the
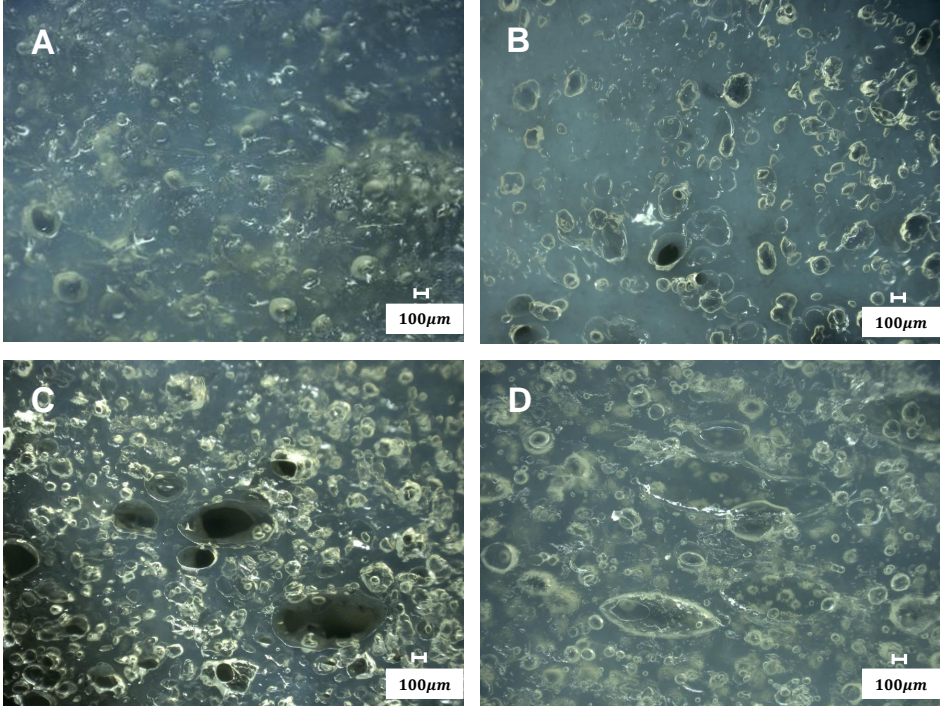
Figure 2.1: Optical microscopy pictures of samples made of A: 100% H_2O, B: 100% H_2O after the solvent exchange with D_2O, C: 50% v/v H_2O+50% v/v D_2O, D: 100% D_2O.

cylinder is defined as β in Eq. 2.5, so $\alpha \cdot \beta \cdot P_{cylinder}$ represents the effect of refraction on the polarisation from cylinders, and $\alpha \cdot (1 - \beta) \cdot P_{sphere}$ represents the refraction from spherical end caps. The total refraction equals to the product of n layers.

$$P_{air\,bubbles} \approx P_{Spherocylinder} = [1 - \alpha + \alpha \cdot \beta \cdot P_{cylinder} + \alpha \cdot (1 - \beta) \cdot P_{sphere}]^n \qquad (2.4)$$

$$\beta = \frac{A_{cylinder}}{A_{cylinder} + A_{spheres}} = \frac{2l}{2l + \pi R} \qquad (2.5)$$

The effect of refraction of the cylinder on the polarisation [25] can be calculated as:

$$P_{cylinder}(B, \gamma) = \kappa(\gamma) \cdot K_1[\kappa(\gamma)] \qquad (2.6)$$

where K_1 is the first-order modified Bessel function of the second kind and

$$\kappa = 4\delta \cdot cos(\gamma) \cdot c \cdot L \cdot cot\theta_0 \cdot B \cdot \lambda \qquad (2.7)$$

in which B represents the magnetic field, the independent variable when using a monochromatic beam; $c = 4.632 \cdot 10^{14} T^{-1} m^{-2}$, which is the Larmor precession constant; $L = 1.31$m,

Figure 2.2: A: A projection of the air bubbles onto the zy-plane. It is approximated by a cylinder with spherical end caps, which equals to the sum of the refraction from a cylinder and a sphere. B: A schematic drawing of one layer of the sample, with the coordinate axis on top. The neutron enters along the x-axis. The grey prolate spheroid-like particles represent the air bubbles. C: The total refraction is contributed by n layers stacked together.

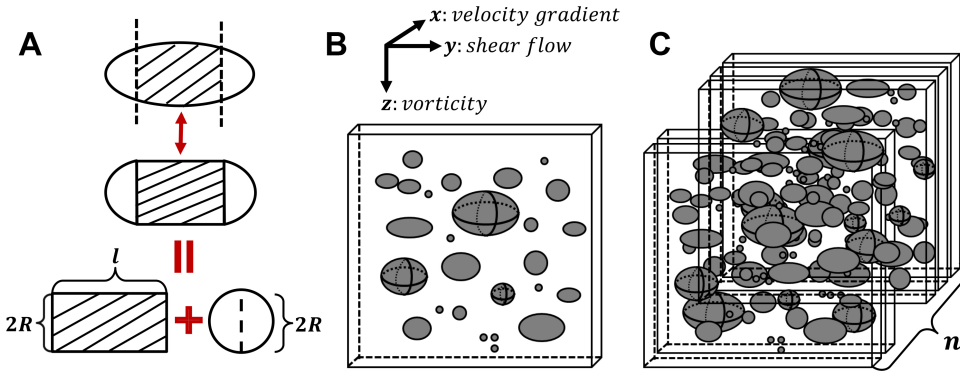it is the length between the magnets and $\theta_0 = 5.5°$, it is the inclination angle of the π flipper in the SESANS instrument; γ is the angle between the axis of the cylinder and the y-axis in the yz-plane, depicted in Fig. 2.3. $cos(\gamma)$ takes care of the slit smearing due to the rotation of the cylinder. As the SESANS instrument in Delft is sensitive to refraction in the z-direction, the change in polarisation will be the largest when the axis of the cylinder is placed parallel to the y-axis, i.e $\gamma = 0°$. Conversely, when it is placed parallel to the z-axis, i.e $\gamma = 90°$, no change in polarisation is expected.

The refraction of the sphere can be calculated from the cylinder by numerically integrating γ over 2π:

$$P_{sphere}(B) = \frac{1}{2\pi} \int_0^{2\pi} P_{cylinder}(B, \gamma) d\gamma \qquad (2.8)$$

An illustration can be found in Fig. 2.3. When the neutron enters the sphere with an angle of γ (dot in Fig. 2.3A), its refraction is equivalent to a cylinder with its axis tilted with γ (Fig. 2.3B). Rotating this cylinder over 360° (Fig. 2.3C), the averaged total refraction of the cylinder equals to the refraction of a sphere. To validate the refraction of a sphere, we applied the model to some glass microspheres that can be find in the supplementary information.

A comparison between Eq. 2.6 and 2.8 reveals that the refraction of the cylinder is dependent on the angular orientation, while not for the sphere. This means if we measure the sample horizontally and vertically, Eq. 2.4 will be specified into two:

$$P_{hor}(B) = [1 - \alpha + \alpha \cdot \beta \cdot P_{cylinder}(B) + \alpha \cdot (1 - \beta) \cdot P_{sphere}(B)]^n \qquad (2.9)$$

and

2. AIR BUBBLES IN FIBROUS CASEINATE GELS INVESTIGATED BY NEUTRON REFRACTION,
16   X-RAY TOMOGRAPHY AND REFRACTIVE MICROSCOPE

2
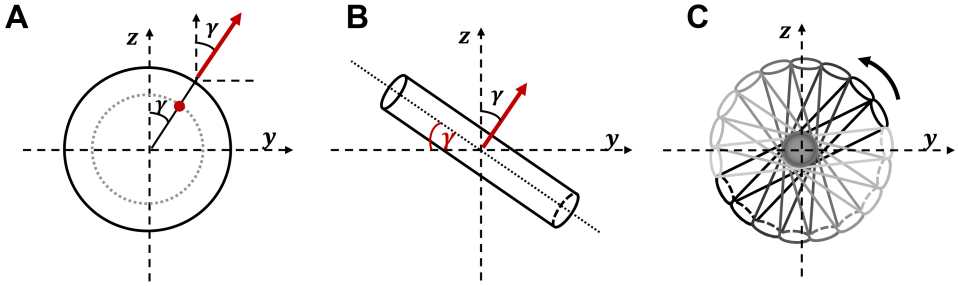
Figure 2.3: Schematic drawings compare the refraction of a sphere to the refraction of a cylinder. A: the neutron (red dot) enters a sphere with an angle of γ. B: the neutron enters a cylinder with its axis tilted with γ. C: The refraction of a sphere (grey circle) equals to the axially averaged refraction of a cylinder.

$$P_{ver}(B) = [1 - \alpha + \alpha \cdot \beta + \alpha \cdot (1 - \beta) \cdot P_{sphere}(B)]^n \qquad (2.10)$$

Eq. 2.9 and 2.10 will use the same α, β and n to fit the horizontal and vertical orientation of the sample.

2.4. RESULTS

2.4.1. NEUTRON REFRACTION

Two sets of calcium caseinate (CaCas) fibrous gels were measured. Each set contains three samples made of 100% H_2O, 50%v/v H_2O+50%v/v D_2O (this sample will be further referred to as 50% D_2O) and 100% D_2O. Since the model is sensitive to the orientation and shape of the air bubbles, each sample was measured in two directions: horizontally (shear flow direction being parallel to the y-axis) and vertically (shear flow direction being parallel to the z-axis). Eq. 2.9 and 2.10 were used to fit the data.
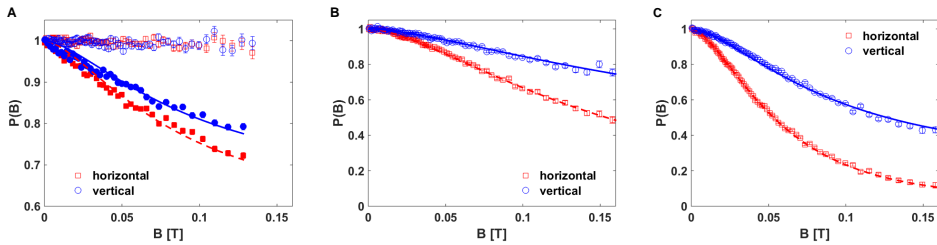
Figure 2.4: Polarisation as a function of applied magnetic field. A: CaCas made of 100% H_2O; B: CaCas made of 50% D_2O; C: CaCas made of 100% D_2O. The square symbols represents the horizontal orientation of the sample, and the circles represents the vertical orientation. The hollow symbols are sample measured ex-situ whilst the filled symbols are measured with the sample sealed in D_2O. Lines are the fitted results using the refraction model.

Fig. 2.4 shows the results of one set of samples. The depolarisation is measured as a

function of magnetic field. The duplicate samples give a similar result. The 100% H_2O sample measured ex-situ (hollow symbol in Fig. 2.4A) gives no signal, probably due to the low contrast. To increase the contrast, we put the sample in a quartz cell filled with pure D_2O and measured it again. The estimated new contrast is $\approx 5.7 \times 10^{14} m^{-2}$, taking into account 10% of the hydrogen in the sample exchange with deuterium in D_2O. A clear signal can be obtained this way (filled symbol in Fig. 2.4A).

For all three samples, the horizontal orientation depolarises more than the vertical orientation. As mentioned, the instrument in Delft is sensitive to the z-axis, meaning that the air bubbles are elongated in the shear flow direction (y-axis). The difference in depolarisation between the horizontal and vertical orientation is the largest in the sample made of 100% D_2O, indicating the air bubbles in this sample are elongated to a higher extent than the others. Furthermore, the 100% D_2O sample contained more air bubbles than the 100% H_2O one, given the fact that after the solvent exchange, the sample made of 100% H_2O depolarised less than the 100% D_2O one, despite a similar contrast. This finding is supported by Fig. 2.1, where the air bubbles in the 100% H_2O samples (Fig. 2.1A) are less elongated and somewhat smaller than the other two (Fig. 2.1C and D). Fig. 2.1B is the 100% H_2O sample after the solvent exchange. It shows that the shape and size of the air bubbles remained intact, suggesting that solvent exchange has little impact on their morphologies.

The first three rows in Table 2.1 show the area fraction of the air bubbles in one layer α, the number of layers n and area fraction of the cylinder β fitted from the refraction model. The standard deviation of the 100% H_2O sample is very large. It appears α and n are highly correlated for this particular sample. It could be due to an inaccurate estimation of the contrast since only this sample was soaked in D_2O.

Looking at the 50% and 100% D_2O samples, the fitted results of α and n vary considerably between duplicates. However, this does not mean the model is unconvincing, since the standard deviation of each parameter remained small. As a result, we owe the large variation to the heterogeneous character of the sample itself.

Though α and n can describe the effect of refraction very well, they don't necessarily contain any direct size information of the sample. Fortunately, the product of α and n contains such information. It is because size information such as dimension and shape is reflected in the total area fraction ($=\alpha \times n$) instead of area fraction in one layer, which means they are convolved in the product of α and n. Thus we need to rewrite $\alpha \times n$ into other expressions in order to derive the dimension and shape of the air bubbles. Based on its definition, $\alpha \times n$ is expressed as:

$$\alpha \times n = \frac{(\pi R^2 + 2Rl) \cdot N}{A_s} \tag{2.11}$$

Where $\pi R^2 + 2Rl$ is the cross-section area of one spherocylinder, N is the total number of spherocylinders in the sample, A_s is the area of the sample covered by the neutron beam. A_s can be expressed as the volume V_s of the sample divided by its thickness t:

Table 2.1: α, n and β are fitted from the refraction model, ϕ from the XRT data. DoD and $2R$ are calculated using $\alpha \times n$, β and ϕ. The errorbars are the standard deviations calculated using the Bootstrap methods [39]. The 100% H_2O sample substituted with D_2O was measured only once.

	100% H_2O	50% D_2O–1	50% D_2O–2	100% D_2O–1	100% D_2O–2
α	0.014 ± 0.009	0.87 ± 0.07	0.38 ± 0.04	0.74 ± 0.02	0.79 ± 0.02
n	40.0 ± 13.8	1.4 ± 0.1	3.9 ± 0.4	3.1 ± 0.1	1.6 ± 0.1
β	0.184 ± 0.003	0.414 ± 0.008	0.437 ± 0.006	0.447 ± 0.002	0.476 ± 0.002
ϕ	0.023	0.142	0.160	0.154	0.122
$\alpha \times n$	0.560 ± 0.002	1.25 ± 0.01	1.48 ± 0.01	2.23 ± 0.01	1.29 ± 0.01
$2R$ (μm)	147 ± 1	332 ± 3	302 ± 1	239 ± 1	390 ± 2
DoD	0.081 ± 0.002	0.217 ± 0.006	0.233 ± 0.004	0.241 ± 0.002	0.263 ± 0.001

$A_s = V_s/t$. V_s can be expressed into the total volume of the spherocylinder divided by its volume fraction ϕ:

$$V_s = \frac{(\frac{4}{3}\pi R^3 + \pi R^2 l) \cdot N}{\phi} \tag{2.12}$$

Where $\frac{4}{3}\pi R^3 + \pi R^2 l$ is the volume of one spherocylinder. Inserting Eq. 2.12 into Eq. 2.11 yields:

$$\alpha \times n = \frac{\phi \cdot t \cdot (\pi R + 2l)}{\frac{4}{3}\pi R^2 + \pi R l} \tag{2.13}$$

Substituting l with β and R using Eq. 2.5 yields:

$$\alpha \times n = \frac{\phi \cdot t}{R} \cdot \frac{1}{\frac{4}{3}(1-\beta) + \frac{\pi}{2} \cdot \beta} \tag{2.14}$$

Eq. 2.14 shows that the product of α and n is related to the volume fraction ϕ of the air bubbles, thickness t, area fraction of the cylinder β and radius of the sphere R. Given ϕ and t are measurable and $\alpha \times n$ and β can be fitted, we can extract a size parameter R from the above equation. As for β, Eq. 2.5 shows that β is essentially related to the dimensions of the spherocylinder. We rewrite this parameter into the earlier defined 'Degree of Deformation' (DoD) so that it becomes comparable to the XRT data in section 2.4.2. $DoD = \frac{l}{l+4R} = \frac{\pi}{\pi+8(\frac{1}{\beta}-1)}$. A larger DoD means the air bubbles are more elongated. $\alpha \times n$, $2R$ and DoD can be found in Table 2.1.

From the fitted parameters, we learned that the average width ($2R$) of the air bubbles in the 100% D_2O sample is almost the same as the 50% D_2O. Both are much larger than the 100% H_2O sample. The bubbles in the 100% D_2O and the 50% D_2O samples are also deformed to a similar extent, suggesting that they are more affected by the shear flow. Whereas for the 100% H_2O sample, the DoD index is quite small, suggesting the air bubbles mostly remained spherical.

Our initial assumption when preparing the samples with different H_2O to D_2O ratios was that the only difference between them is the contrast. The fitted results suggest otherwise. It seems that D_2O had an unexpected influence on the size and shape of the air

bubbles in the final structure. In the next section, we will present XRT data to support these findings.
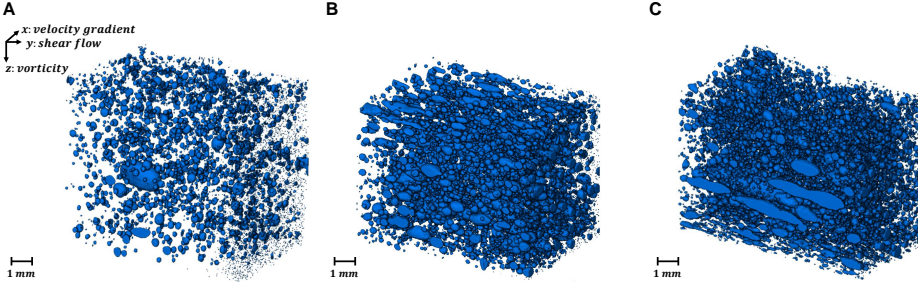
2.4.2. X-RAY TOMOGRAPHY

Figure 2.5: 3D reconstructed tomography of one set of the samples. The samples are made of A: 100% H_2O; B: 50% D_2O and C: 100% D_2O.

In neutron refraction, the parameters $2R$ and DoD are an average representation of all the air bubbles in the sample. With XRT, the $2R$ and DoD of every single air bubble can be obtained. We first present the 3D reconstructed tomography of the three samples in Fig. 2.5. It is clear that the sample made of 100% H_2O contains fewer air bubbles than the other two. The air bubbles are also smaller, which corresponds to the fitted width($2R$) of the spherocylinder. Next, we present the distributions of the number of air bubbles ($Number$) and the degree of deformation (DoD) based on the cross-section area. The cross-section area is defined as $\frac{\pi}{4} \cdot a \cdot b$, where a and b is the length of the long and short axes of an ellipsoid. The results are shown in Table 2.2.

Table 2.2: XRT results: the distribution of the $Number$ of bubbles per volume and the DoD calculated based on the cross-section area. The values are an average of two measurements, the errorbars are differences from the mean.

	cross-section area (mm^2)	100% H_2O	50% D_2O	100% D_2O
$Number$	≤ 0.01	11103 ± 5495	5900 ± 945	8116 ± 1648
	$0.01 \sim 0.1$	1287 ± 33	2326 ± 41	3012 ± 13
	$0.1 \sim 1$	31 ± 2	201 ± 18	211 ± 46
	≥ 1	1 ± 0	8 ± 3	6 ± 1
DoD	≤ 0.01	-0.067 ± 0.021	-0.009 ± 0.002	-0.001 ± 0.002
	$0.01 \sim 0.1$	-0.019 ± 0.019	0.063 ± 0.016	0.058 ± 0.019
	$0.1 \sim 1$	-0.015 ± 0.007	0.207 ± 0.000	0.210 ± 0.076
	≥ 1	0.338 ± 0.011	0.522 ± 0.035	0.417 ± 0.090

Similar to the neutron refraction data, the differences between the two sets of samples are large, suggesting inhomogeneities in the samples. For all three samples, the number

of air bubbles decreased with increasing cross-section area, while the *DoD* increased with increasing cross-section area. The few large air bubbles are more susceptible to shear than the smaller ones. Further, both parameters are much larger when D_2O is present in the system. D_2O seemed to be responsible for larger air bubbles sizes and higher extent of elongation.
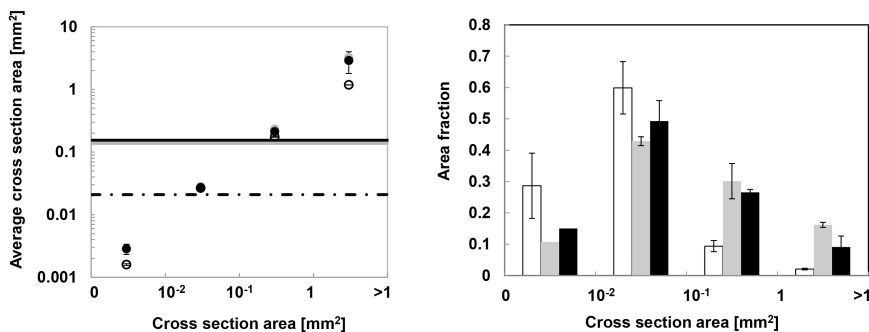

Figure 2.6: Left: average cross-section area of the air bubble calculated from the neutron refraction model (lines) versus the cross-section areas from the XRT data (symbols). The 100% H_2O sample is represented by the dash-dot line and hollow circles; the 50% D_2O sample is represented by the grey line and grey circles; The 100% D_2O sample is represented by the black line and black circles; Right: area fraction based on cross-section area. The white, grey and black bars correspond to sample made of 100% H_2O, 50% D_2O and 100% D_2O, respectively.

Figure 2.7: Left: average volume of the air bubble calculated from the neutron refraction model (lines) versus the volumes from the XRT data (symbols). The 100% H_2O sample is represented by the dash-dot line and hollow circles; the 50% D_2O sample is represented by the grey line and grey circles; The 100% D_2O sample is represented by the black line and black circles; Right: volume fraction based on cross-section area. The white, grey and black bars correspond to sample made of 100% H_2O, 50% D_2O and 100% D_2O, respectively.

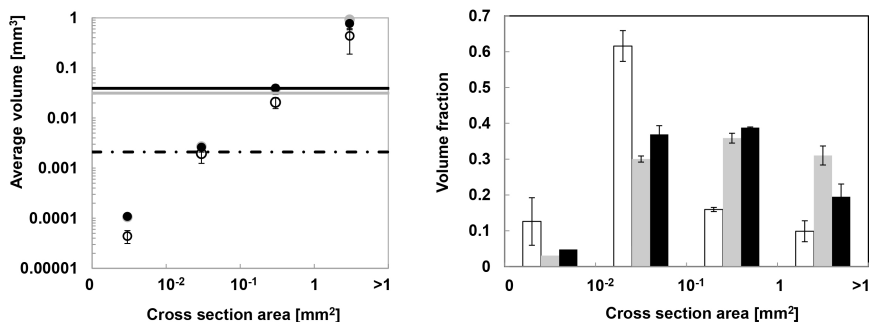Since the *Numbers*, sizes and *DoD* affect the area and volume of the air bubbles simultaneously, we plotted the average area, volume and their fractions in Fig. 2.6 and 2.7. For comparison, we also included the calculated average area and volume in the

figure using the fitted results from the refraction data. The average area and volume of the spherocylinder are calculated as $\pi R^2 + 2Rl$ and $\frac{4}{3}\pi R^3 + \pi R^2 l$ respectively. In Fig. 2.6 left, the calculated average area of the air bubble from the refraction model in the 100% H_2O sample corresponds well to the cross-section area between $0.01 \sim 0.1$ mm^2. This cross-section area happens to take up the largest area fraction (Fig. 2.6 right). Similarly, the average area of the 50% and 100% D_2O samples fall in between $0.01 \sim 1$ mm^2, the sum of the two area fractions takes up around 75%. This trend applies to volume fraction as well. Fig. 2.7 shows that the calculated average volume of the air bubble falls into the cross-section area who takes up the largest volume fraction for all samples. To summarise, the fitted parameters from the refraction model are representative of the air bubbles that take up the largest area and volume.

2.5. DISCUSSION

"Foods are a complex and heterogeneous system." [21], because of this, we utilized several techniques to ensure an objective and thorough understanding of the system. The refractive microscopy provides valuable, descriptive information of the air bubbles. However, the sample volume that can be probed by the microscope is very limited, thus the information may not be representative of the whole system. To quantify the sample with a larger volume, we used two complementary techniques: neutron refraction and XRT. They are compared in the following aspects:

1) Sensitivity to contrast: XRT can distinguish well between the protein matrix and air bubbles without any pretreatment, while the initial contrast for neutron refraction is insufficient. Two methods can be used to increase the neutron refraction contrast. One is solvent exchange after obtaining the sample, the other one is replacing H_2O with D_2O during the production of the sample. In our study, the first method worked better, since it has little perturbation on the structure, as shown by the microscopy image of the 100% H_2O sample after soaking in D_2O. The latter method highlighted the unwanted influence of D_2O on the morphology of the air bubbles, probably because the structure of the protein matrix was changed. It could be that D_2O has a stronger D-D bond than H_2O, which imposes a more hydrophobic environment onto the calcium caseinate. The consequences are delayed wetting of the protein powder, the hydrophobic parts of the protein become more compact and more rigid aggregates [40]. These factors contribute to a more elastic gel network that will be more susceptible to shear [11]. In addition, an increase in elasticity is related to a better air entrapping ability. As a result, when applying the neutron refraction technique, the choice of method to increase the contrast depends on the susceptibility of the food building blocks to the solvent environment.

2) Advantages and Drawbacks: For neutron refraction, the advantages are i) objectivity of the method in sense of data processing and interpretation; ii) only a few parameters are needed to give a quantitative description of the sample; iii) it can probe a relatively large sample size. The advantages of XRT are i) no pre-treatment is needed prior to the measurement; ii) higher accessibility to the instrument and iii) the 2D/3D reconstructed results are straightforward. The drawback of neutron refraction is the potential effect of D_2O on the morphology of the air bubbles. Though we suspect the effect will be negligi-

ble in other food materials such as fat or cellulose. For XRT, the drawbacks are the imaging artefacts during image acquisition and operator dependency during image analysis. Both may render the results less reproducible. This is also why we promote utilizing multiple techniques to increase certainty in the interpretation of a complex system.

3) Future prospects: currently, XRT has far more applications in food products compared to neutron refraction. Nevertheless, the neutron refraction technique has the potential to be applied to other composite food materials, as long as there is sufficient contrast between the filler and the matrix, and the filler has a desired size range. For instance, it can be used to study the distribution of fat in different types of sausages [41], or the stability of aerated food products [42].

2.6. Conclusion

Air bubbles in a composite meat analogue made of calcium caseinate are studied by the neutron refraction technique, XRT and microscope. A model was constructed to calculate the depolarisation of the neutrons refracted by air bubbles in fibrous protein gels. Average width, deformation direction and degree of the air bubbles can be obtained from the model which agreed well with the XRT data and microscopy image. These parameters represent an average of the system given they correspond to the largest area and volume fraction of the air bubbles in the XRT data. This technique may be a standard routine in future and has the potential to be applied to other composite food systems, as long as structural differences caused by D_2O are taken into account.

2.7. Supplementary information

Refraction of spherical objects

Before the refraction model was applied to the air bubbles, we first measured some glass microspheres as a model system to validate the refraction model. These microspheres have a narrow diameter distribution of $1 - 1.18mm$, according to the manufacturer's specification.

$$P_{ver}(B) = [1 - \alpha + \alpha \cdot \beta + \alpha \cdot (1 - \beta) \cdot P_{sphere}(B)]^n \qquad (2.15)$$

Equation 2.15 can be used to calculate the theoretical refraction of the sphere given $\beta = 0$ (no contribution from the cylinder) and $\alpha = 0.785$. The value of α is chosen based on the fact that unlike a cylinder, the area fraction of the sphere will not cover the beam fully and the maximum area fraction for closely packed spheres equals to $\frac{\pi}{4} \approx 0.785$. Figure 2.8 compares the measurements and the theoretical calculation, illustrating the validity
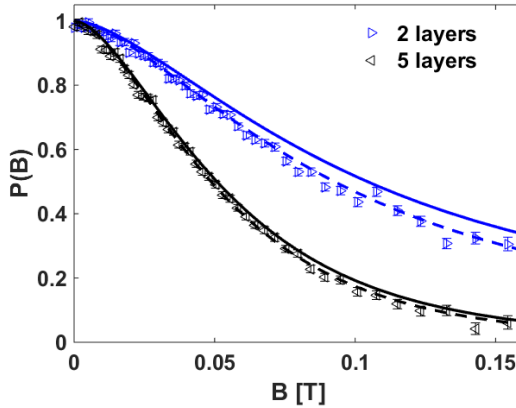
Figure 2.8: Polarisation $P(B)$ as a function of magnetic field strength B. Two layers (right-pointing triangles) and five layers (left-pointing triangles) of glass micro-sphere were measured. The solid lines are the corresponding polarisations calculated from the refraction model, with n = 2 and n = 5. The dashed lines represent polarisations with adjusted n = 2.3 and n = 5.3.

of the model. The deviation between the measured data and the theoretical calculation can be minimized with a slight increase of n. A systematic deviation could either be due to imperfections of the sample or to the limitation of the model, in our case, we suspect it is related to the surface roughness of microspheres.

CROSS-SECTION OF THE AIR BUBBLES

In the neutron refraction model, the cross-section of the cylinder parallel to the neutron beam is assumed to be circular (which means the cylinder is perpendicular to the beam). In figure 2.9, we provide the microscopy picture and 2D x-ray radiography to show that the cross-section of the air bubbles along the neutron beam is indeed circular.

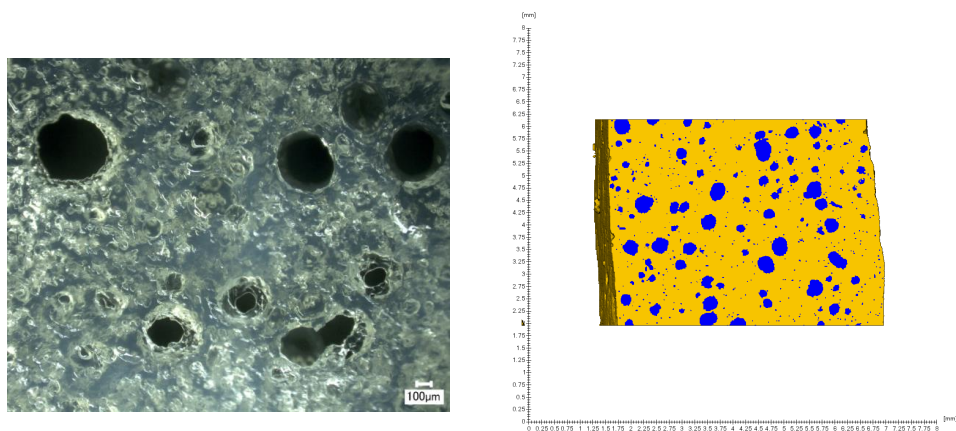Figure 2.9: Pictures showing the shape of the cross-section of the air bubbles along the neutron beam. Left: light microscopy picture of sample made with 50% D_2O; right: 2D x-ray radiography of sample made of 50% D_2O.

REFERENCES

[1] B. Tian, Z. Wang, A. J. van der Goot, and W. G. Bouwman, *Air bubbles in fibrous caseinate gels investigated by neutron refraction, x-ray tomography and refractive microscope,* Food Hydrocolloids **83**, 287 (2018).

[2] G. A. van Aken, L. Oliver, and E. Scholten, *Rheological effect of particle clustering in gelled dispersions,* Food Hydrocolloids **48**, 102 (2015).

[3] R. van der Sman, *Filler functionality in edible solid foams,* Advances in colloid and interface science **231**, 23 (2016).

[4] B. Dobraszczyk and M. Morgenstern, *Rheology and the breadmaking process,* Journal of cereal Science **38**, 229 (2003).

[5] A. Bryant, Z. Ustunol, and J. Steffe, *Texture of cheddar cheese as influenced by fat reduction,* Journal of Food Science **60**, 1216 (1995).

[6] E. O. Afoakwa, A. Paterson, and M. Fowler, *Factors influencing rheological and textural qualities in chocolate–a review,* Trends in Food Science & Technology **18**, 290 (2007).

[7] K. J. Grabowska, A. J. van der Goot, and R. M. Boom, *Salt-modulated structure formation in a dense calcium caseinate system,* Food hydrocolloids **29**, 42 (2012).

[8] J. M. Manski, A. J. van der Goot, and R. M. Boom, *Formation of fibrous materials from dense calcium caseinate dispersions,* Biomacromolecules **8**, 1271 (2007).

[9] J. M. Manski, A. J. van der Goot, and R. M. Boom, *Advances in structure formation of anisotropic protein-rich foods through novel processing concepts,* Trends in Food Science & Technology **18**, 546 (2007).

[10] G. A. Krintiras, J. G. Diaz, A. J. Van der Goot, A. I. Stankiewicz, and G. D. Stefanidis, *On the use of the couette cell technology for large scale production of textured soy-based meat replacers,* Journal of Food Engineering **169**, 205 (2016).

[11] J. M. Manski, L. E. van Riemsdijk, A. J. van der Goot, and R. M. Boom, *Importance of intrinsic properties of dense caseinate dispersions for structure formation,* Biomacromolecules **8**, 3540 (2007).

[12] B. L. Dekkers, R. Hamoen, R. M. Boom, and A. J. van der Goot, *Understanding fiber formation in a concentrated soy protein isolate-pectin blend,* Journal of Food Engineering **222**, 84 (2018).

[13] G. van Dalen, H. Blonk, H. van Aalst, and C. L. Hendriks, *3-d imaging of foods using x-ray microtomography,* GIT Imaging and Microscopy **3**, 18 (2003).

[14] S. Das, A. Maroli, S. S. Singh, T. Stannard, X. Xiao, N. Chawla, and N. Neithalath, *A microstructure-guided constitutive modeling approach for random heterogeneous materials: Application to structural binders,* Computational Materials Science **119**, 52 (2016).

[15] X. Kuang, G. Ying, V. Ranieri, and J. Sansalone, *Examination of pervious pavement pore parameters with x-ray tomography,* Journal of Environmental Engineering **141**, 04015021 (2015).

[16] B. Duquenne, B. Vergauwen, C. Capdepon, M. A. Boone, T. De Schryver, L. Van Hoorebeke, S. Van Weyenberg, P. Stevens, and J. De Block, *Stabilising frozen dairy mousses by low molecular weight gelatin peptides,* Food Hydrocolloids **60**, 317 (2016).

[17] G. G. Bellido, M. G. Scanlon, J. H. Page, and B. Hallgrimsson, *The bubble size distribution in wheat flour dough,* Food Research International **39**, 1058 (2006).

[18] I. Demirkesen, S. Kelkar, O. H. Campanella, G. Sumnu, S. Sahin, and M. Okos, *Characterization of structure of gluten-free breads by using x-ray microtomography,* Food Hydrocolloids **36**, 37 (2014).

[19] J. Guo, Y.-C. Jin, X.-Q. Yang, S.-J. Yu, S.-W. Yin, and J.-R. Qi, *Computed microtomography and mechanical property analysis of soy protein porous hydrogel prepared by homogenizing and microbial transglutaminase cross-linking,* Food Hydrocolloids **31**, 220 (2013).

[20] B. L. Dekkers, R. Hamoen, R. M. Boom, and A. J. van der Goot, *Understanding fiber formation in a concentrated soy protein isolate-pectin blend,* Journal of Food Engineering **222**, 84 (2018).

[21] A. Donald, *Food for thought,* Nature Materials **3**, 579 (2004).

[22] L. Schoeman, P. Williams, A. du Plessis, and M. Manley, *X-ray micro-computed tomography (μct) for non-destructive characterisation of food microstructure,* Trends in Food Science & Technology **47**, 10 (2016).

[23] E. Maire and P. J. Withers, *Quantitative x-ray tomography,* International materials reviews **59**, 1 (2014).

[24] V. Cnudde and M. N. Boone, *High-resolution x-ray computed tomography in geosciences: A review of the current technology and applications,* Earth-Science Reviews **123**, 1 (2013).

[25] J. Plomp, J. Barker, V. De Haan, W. Bouwman, and A. van Well, *Neutron refraction by cylindrical metal wires,* Nuclear Instruments and Methods in Physics Research Section A: Accelerators, Spectrometers, Detectors and Associated Equipment **574**, 324 (2007).

[26] V.-O. d. Haan, J. Plomp, W. G. Bouwman, M. Trinker, M. T. Rekveldt, C. P. Duif, E. Jericha, H. Rauch, and A. A. van Well, *Phase-object approximation in small-angle neutron scattering experiments on silicon gratings,* Journal of Applied Crystallography **40**, 151 (2007).

[27] N. Berk and K. Hardman-Rhyne, *Analysis of sas data dominated by multiple scattering,* Journal of Applied Crystallography **21**, 645 (1988).

[28] C. Ersch, M. B. Meinders, W. G. Bouwman, M. Nieuwland, E. van der Linden, P. Venema, and A. H. Martin, *Microstructure and rheology of globular protein gels in the presence of gelatin,* Food Hydrocolloids **55**, 34 (2016).

[29] M. Nieuwland, W. G. Bouwman, M. L. Bennink, E. Silletti, and H. H. de Jongh, *Characterizing length scales that determine the mechanical behavior of gels from crosslinked casein micelles,* Food biophysics **10**, 416 (2015).

[30] R. H. Tromp and W. G. Bouwman, *A novel application of neutron scattering on dairy products,* Food Hydrocolloids **21**, 154 (2007).

[31] V.-O. de Haan, J. Plomp, and A. A. van Well, *Real-space form factor of spherical particles in kinematic and dynamic scattering,* Journal of Applied Crystallography **40**, 756 (2007).

[32] G. A. Krintiras, J. Göbel, W. G. Bouwman, A. J. Van Der Goot, and G. D. Stefanidis, *On characterization of anisotropic plant protein structures,* Food & function **5**, 3233 (2014).

[33] A. Van der Goot, S. Peighambardoust, C. Akkermans, and J. van Oosten-Manski, *Creating novel structures in food materials: The role of well-defined shear flow,* Food Biophysics **3**, 120 (2008).

[34] E. van der Zalm, J. Berghout, A. van der Goot, and R. Boom, *Starch–gluten separation by shearing: Influence of the device geometry,* Chemical engineering science **73**, 421 (2012).

[35] Z. Wang, *Multiphase effects in forming anisotropic calcium caseinate materials,* DOI10.18174/477977 (2019), dissertation.

[36] M. T. Rekveldt, J. Plomp, W. G. Bouwman, W. H. Kraan, S. Grigoriev, and M. Blaauw, *Spin-echo small angle neutron scattering in delft,* Review of Scientific Instruments **76**, 033901 (2005).

[37] M. T. Rekveldt, W. Bouwman, W. Kraan, O. Uca, S. Grigoriev, K. Habicht, and T. Keller, *Elastic neutron scattering measurements using larmor precession of polarized neutrons,* in *Neutron Spin Echo Spectroscopy* (Springer, 2002) pp. 87–99.

[38] W. G. Bouwman, T. V. Krouglov, J. Plomp, S. V. Grigoriev, W. H. Kraan, and M. T. Rekveldt, *Sesans studies of colloid phase transitions, dairy products and polymer fibres,* Physica B: Condensed Matter **350**, 140 (2004).

[39] B. Efron, *Bootstrap methods: another look at the jackknife,* in *Breakthroughs in statistics* (Springer, 1992) pp. 569–593.

[40] D. Oakenfull and A. Scott, *Gelatin gels in deuterium oxide,* Food hydrocolloids **17**, 207 (2003).

[41] P. Frisullo, J. Laverse, R. Marino, and M. Del Nobile, *X-ray computed tomography to study processed meat microstructure,* Journal of Food Engineering **94**, 283 (2009).

2

[42] A. Ellis, A. Norton, T. Mills, and I. Norton, *Stabilisation of foams by agar gel particles,* Food Hydrocolloids **73**, 222 (2017).

2

3

Fibre formation in calcium caseinate influenced by solvent isotope effect and drying method - A neutron spectroscopy study

We present an investigation of the dynamics of calcium caseinate as a function of hydration, solvent isotope (H_2O and D_2O) and drying methods (roller drying and spray drying), using quasi-elastic neutron scattering (QENS). These factors are key to the formation of fibres in this material which makes it a potential candidate as a next-generation meat analogue. Using a phenomenological model, we find that the relaxation times of the dry spray dried powder decrease with increasing temperatures, while they do not change for the roller dried powder. The spectra of the hydrated samples reveal two independent picosecond processes, both reflecting localized re-orientational motions. We hypothesize that the faster motion is due to the external protein groups that are hydrophilic and the slower motion is due to the internal groups that are hydrophobic. The solvent effect of D_2O is not limited to the external groups but prevails to the internal groups where less protons are mobile compared to the H_2O hydrated samples. Higher temperatures narrow the number difference in mobile protons, possibly by altering the weak interactions inside the protein aggregates. These findings suggest that a harsh and longer drying process contributes to less active protein side-groups and highlight the hydrophobic effect of D_2O on the fibre formation in calcium caseinate.

3.1. Introduction

The mechanism of fibre formation in calcium caseinate has been at the focus of research interest during the last decade, as these fibrous structures are promising candidates for the production of next-generation meat analogues [2, 3]. The fibrous calcium caseinate gel has good mechanical properties, and its structure is much more anisotropic [4] than plant-based meat analogue candidates [5]. In view of potential applications, it is therefore important to investigate the structure and dynamics of the fibrous structure in calcium caseinate, as these studies provide valuable insight into the design of plant-based meat analogues with more pronounced anisotropic structures.

Recently, we came across an interesting observation: the calcium caseinate fibre formation is strongly influenced by the solvent isotope effect [6]. 30%w/w spray dried calcium caseinate (SCaCas) mixed with H_2O gives more anisotropic fibres, while roller dried calcium caseinate (RCaCas) processed under the same condition results in a homogeneous gel. When D_2O is used to mix with the calcium caseinate powder, the fibres in SCaCas do not form, while RCaCas does show some fibres. Given that the only variable is the solvent, we assume that both the molecular motions of the protein and the interactions between the solvent and protein (e.g. hydrogen bonds) change because of the solvent isotope effect. To test the validity of this hypothesis, we used quasi-elastic neutron scattering (QENS) to investigate the dynamics of both SCaCas and RCaCas on a molecular level.

QENS has been successfully applied to study the dynamics at the atomic scale of many biological systems: from globular protein such as lysozyme, myoglobin and green fluorescent protein (GFP) [7–10] to bio macro-molecules like tRNA, DNA and membranes [11–14]. The technique probes timescales and amplitudes of the dynamics and gives insights into the interactions with hydration water. The application of QENS on food materials is much less explored than on biological systems. The few existing examples focus on the hydration water dynamics. For instance, the self-diffusion constant of water in fresh bread was obtained by fitting the self-intermediate scattering function with a stretched exponential function at room temperature [15]; A similar approach has been applied to study dehydrated fresh strawberry and rehydrated freeze-dried strawberry [16]. A study on a larger globular glycinin showed that its dynamic transition is similar to that observed in smaller proteins[17]. These investigations hint to a relation between the food matrix and the hydration water.

Until now, most of the QENS measurements were conducted on samples obtained through freeze-drying [18–20], as it is assumed that this process affects less the denaturation and aggregation of the protein [21–24]. Though lyophilisation has its advantages, it is not used by the food industry due to its high operational costs and low throughput [25]. Furthermore, lyophilisation is not representative of the effect of other drying methods on the protein dynamics. As a result, investigations of the influence of spray and roller drying on the protein structure and dynamics are of great importance to the field of food science, given that these methods are commonly used for the industrial production of food biopolymers [26].

Our QENS investigation probes for the first time, the protein dynamics of industrially produced food powders, which can potentially mimic real meat. The experiments were performed on dry SCaCas and RCaCas powders, as well as on powders hydrated with either D_2O or H_2O, to a hydration level of h=0.4 (weight solvent/weight dry protein powder), which is generally considered to be a full hydration level [27]. The measurements were performed at 293 K, i.e. at room temperature, at 320 K, the temperature at which the fibres are obtained, and at 340 K where protein aggregates form reversible agglomerates.

One of the strengths of neutron scattering is the possibility to highlight, by deuteration, certain parts of the hydrogen containing samples. However, in our study, it was not possible to deuterate the caseinate. One reason is that it is an industrial product obtained from casein curd and there is a batch to batch variation. Another reason is that caseinate is composed of four sub-caseins, its structure is not well-defined and still under debate [28, 29]. Therefore, unlike other model systems, it would have been very challenging to deuterate a specific part of the caseinate. Nevertheless, we were able to investigate the solvent isotope effect and compare the effect of hydration by using either H_2O or D_2O. Through the data analysis we can assign the dynamics to certain protein groups and correlate them to the macroscopic observations of fibre formation.

3.2. Material and Methods

3.2.1. Sample preparation

Roller and spray dried calcium caseinate powders were provided by DMV International, Veghel, The Netherlands. The solvent used throughout the drying process was H_2O. As their names suggest, the powders were obtained through roller drying or spray drying, which resulted in different powder morphologies. Scanning electron microscopy images were taken using JEOL JSM-IT100. The secondary electron detector was used with 1.6 kV, a probe current of 20 nA, and the magnification was 200.

For the QENS measurements, the powders were first dehydrated in a vacuum oven at 60°C for 2 days. The dried samples were then hydrated in hydration chambers with either D_2O or H_2O. All samples reached a hydration level of ~0.4 (weight solvent/weight dry protein powder). Approximately 400 mg of powder was loaded and sealed in an annular aluminum sample holder with a thickness of 2 mm.

The scattering cross sections of the samples were calculated according to the specifications provided by the manufacturer and are shown in Table 3.1. The incoherent cross section of the dry powder accounts for up to 89.6% of the signal. After hydration with H_2O, the scattering contribution from the protein decreased to 63.1%. After hydration with D_2O, assuming 20% of the hydrogen has exchanged with deuterium, the contribution of the protein to the scattering still accounts for up to 81.9%.

Table 3.1: Incoherent, coherent and absolute scattering cross sections (σ) of the dry and hydrated samples calculated based on the amino acid compositions of calcium caseinate provided by the supplier.

	Dry powder	Hydrated with 0.4 g/H_2O g		Hydrated with 0.4 g/D_2O g	
		Protein	Solvent	Protein[*]	Solvent
σ_{inc}%	89.6	63.1	27.8	81.9	1.2
σ_{coh}%	8.0	5.6	1.3	10.1	4.4
σ_{abs}%	2.4	1.7	0.4	2.4	0

[*]Assuming 20% of the H exchanged with D.

3.2.2. QUASI-ELASTIC NEUTRON SCATTERING EXPERIMENTS

The QENS experiments were performed at the time-of-flight inverted geometry spectrometer IRIS [30] at the ISIS neutron facility, as a function of both energy (ω) and momentum transfer (Q). We used the [002] reflection of the pyrolytic graphite analyser, which gives an energy resolution of 17.5 μeV, and covers an energy range from -0.5 to 0.5 meV. The scattered neutrons were measured by 51 detectors that cover a Q-range from 0.42 to 1.85 Å^{-1}. During fitting of the elastic incoherent structure factor (EISF), the signals of the these 51 detectors were regrouped into 15 Q values to improve statistics.

The samples were measured at 293 K, 320 K and 340 K for around 5 hours, respectively. So-called elastic scans were conducted from 20 K to 340 K with an increment step of 10 K. The detector efficiency was corrected by measuring a vanadium standard. The resolution function was obtained by measuring the corresponding sample at 20 K. The data reduction was performed with the Mantid software [31], and the reduced spectra were analyzed using the software DAVE [32].

3.3. RESULTS

3.3.1. QUASI-ELASTIC WIDTHS AND AMPLITUDES

After initial fitting, we found that two uncoupled Lorentzian functions are needed to describe the quasi-elastic contribution. For a detailed documentation of the fits, the reader is referred to the supplementary information. Our initial results also show that the full width half maximum (FWHM) Γ of the two Lorentzian functions are Q-independent (supplementary information), suggesting that we observe either re-orientational or localised motions. In order to obtain accurate values of Γ, we summed the intensity of all detectors and fitted the data with the scattering function:

$$S(\omega) = [A_0 \cdot \delta(\omega) + A_{slow} \cdot L_{slow}(\omega) + A_{fast} \cdot L_{fast}(\omega)$$
$$+ a\omega + b] \otimes R(\omega). \tag{3.1}$$

where $A_0 \cdot \delta(\omega)$ is the elastic scattering contribution with A_0 the elastic amplitude and $\delta(\omega)$ the Dirac delta function. A_{slow} and A_{fast} are the quasi-elastic amplitudes, $L_{slow}(\omega)$ and $L_{fast}(\omega)$ are the Lorentzian functions, and $R(\omega)$ is the resolution function. Any inelastic contributions that are outside the energy window of the instrument are accounted for
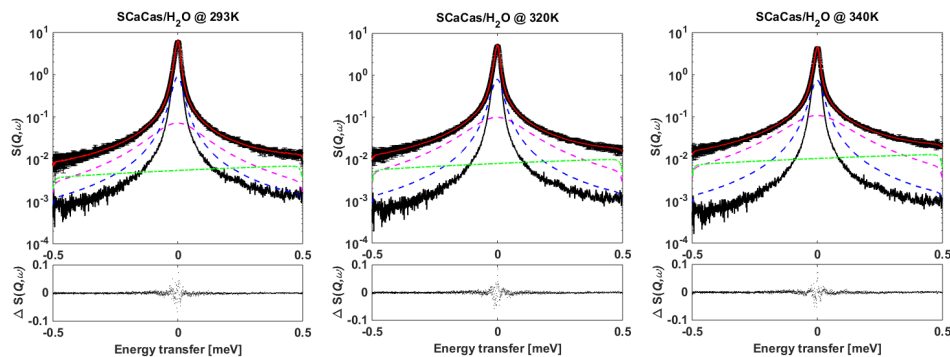
by the linear background $a\omega + b$.

Figure 3.1: From left to right: QENS spectra of SCaCas powder hydrated with H$_2$O measured at 293 K, 320 K and 340 K. The residuals are plotted underneath, they are calculated as the difference between the measured and fitted S(Q, ω). The delta function is represented by the black dots, the two Lorentzians are dashed lines in blue and magenta, the background is dash-dot line in green, and the total fitted curve is represented by the red line.

Fig. 3.1 shows the spectra measured for the SCaCas sample hydrated with H$_2$O at three temperatures. The fits for the other samples can be found in the supplementary information, and the fitted parameters are summarised in Table 3.2.
 The FWHM of the Lorentzian function is inversely proportional to the relaxation times. The FWHMs of the dry SCaCas powder, shown in Table 3.2, are systematically smaller than those of the RCaCas at room temperature. While both Γ_{slow} and Γ_{fast} of SCaCas increase with temperature, they remain constant in RCaCas, implying that the dynamics of the protein groups in RCaCas are insensitive to temperature. The drying history that the powder has experienced is probably responsible for these differences.

Hydration increases significantly the quasi-elastic amplitudes. This is not surprising since the solvent increases the protein to be more flexible and mobile. Similar results were also obtained by for example Orecchini et al, who studied the (non)exchangeable hydrogen classes in β-lactoglobulin [18], and found that the quasi-elastic intensity of both the protein surface and the core groups increased with increasing hydration level.

On the other hand, hydration has little impact on the width of the Lorentzians. Unlike the dry powders, the FHWMs of all hydrated samples display a similar trend. Both Γ_{slow} and Γ_{fast} increase with temperature, and the corresponding relaxation times decrease from approximately 52 ps to 40 ps for the slow motion , and from 7 ps to 5.4 ps for the fast motion. The Γ_{slow} and Γ_{fast} reported here are in line with the values reported for other protein systems, such as the internal motion of *E.coli* [33] and lysozyme [8] for Γ_{slow}; Neocarzinostatin, a small all β protein [34], Ribonuclease A [35] and the hydrophobic side-chains of native α-lactalbumin [36] for Γ_{fast}.

Table 3.2: Fitted parameters of SCaCas and RCaCas powders dry, hydrated with either D_2O or H_2O at 293 K, 320 K and 340 K. Columns 3-6 give the area fraction of the delta function, the background (bkdg) and the two Lorentzian functions (L_{fast} and L_{slow}). The area fraction is calculated as the amplitude of one component divided by the sum of all the amplitudes ($A_0 + A_{slow} + A_{fast}$+background), the estimated error bar of the area fraction is within 1% in all cases; columns 7-8 are the corresponding FWHMs of the Lorentzian functions.

3

		Area (%)				FWHM	(μeV)
		delta	bkgd	L_{slow}	L_{fast}	Γ_{slow}	Γ_{fast}
	293 K	89.8	0.8	6.6	2.9	25±4	163±17
SCaCas/dry	320 K	89.2	0.8	7.2	2.8	39±3	239±26
	340 K	86.9	1.2	7.9	4.0	53±7	293±79
	293 K	89.2	1.2	7.5	2.1	32±2	247±24
RCaCas/dry	320 K	87.7	1.5	7.5	3.0	34±2	227±18
	340 K	86.4	1.7	7.9	4.0	36±2	226±15
	293 K	74.9	1.9	16.8	6.4	26±1	188±8
SCaCas/D_2O	320 K	68.1	2.9	19.2	9.8	33±1	214±8
	340 K	63.0	3.3	21.1	12.6	36±2	244±14
	293 K	73.5	1.9	17.8	6.7	25±1	201±77
RCaCas/D_2O	320 K	66.1	3.0	19.9	11.0	28±1	202±56
	340 K	60.0	3.9	21.4	14.7	30±1	221±67
	293 K	61.0	2.6	25.6	10.9	26±1	196±5
SCaCas/H_2O	320 K	52.1	4.0	26.2	17.7	31±1	219±4
	340 K	46.5	5.4	26.3	21.9	33±1	240±4
	293 K	65.5	2.4	22.4	9.6	25±1	182±6
RCaCas/H_2O	320 K	57.6	3.7	23.9	14.8	32±1	216±5
	340 K	52.8	4.4	24.3	18.5	33±2	235±9

Though the FWHMs of the Lorentzians follow quite similar trends for the different samples and solvents, this is not the case for their area fractions, which vary depending on the drying method and the solvent. When hydrated with D_2O, the L_{fast} and L_{slow} are slightly smaller for SCaCas than for RCaCas, which suggests that there are less mobile protons in SCaCas. On the other hand, when hydrated with H_2O, L_{fast} and L_{slow} are larger for SCaCas than for RCaCas. As far as the solvent isotope effect is concerned, H_2O hydrated samples have in general higher quasi-elastic amplitudes than the D_2O hydrated ones. This is most likely due to the H_2O molecules that are bound to the protein surface and have dynamics that are similar to the protein. In particular, the increase of area fractions is larger for SCaCas than for RCaCas when switching from D_2O to H_2O. These results indicate that the response of the protein dynamics to the solvent isotope effect is influenced by the drying history. A possible explanation is that the protein side-group activities are different due to either chemical reactions during processing, or to a different structural arrangement of the caseinate.
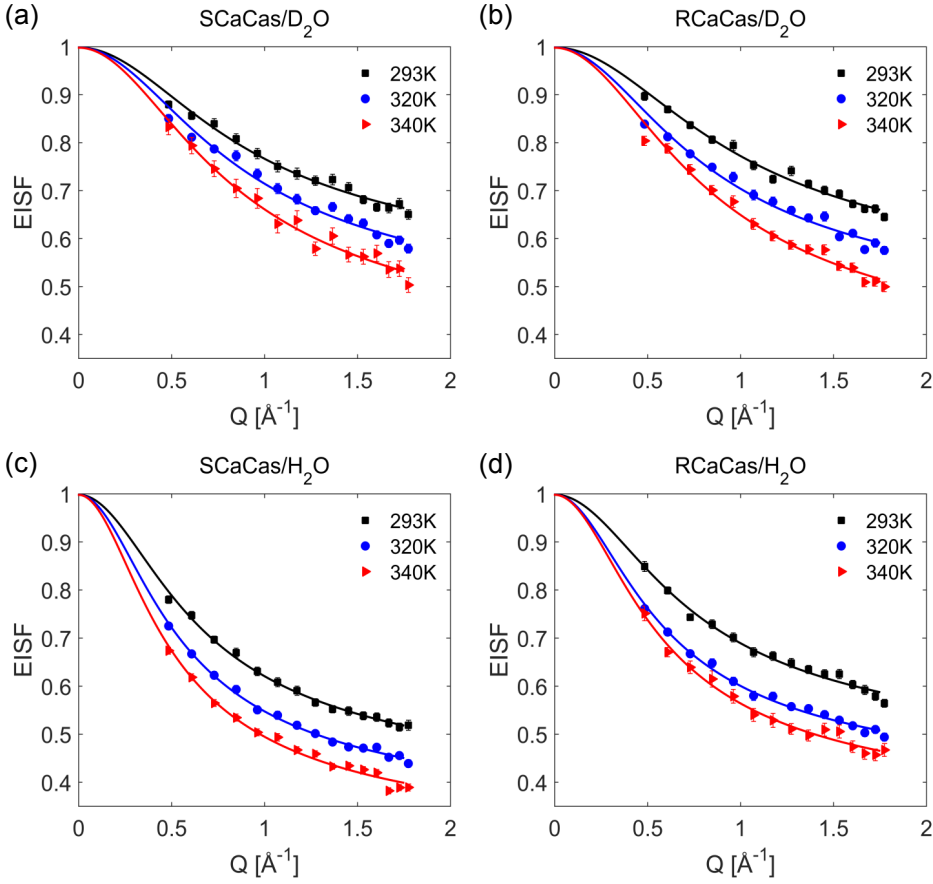
Figure 3.2: EISF fitted with the free diffusion in a sphere model, plotted as a function of Q at different temperatures. SCaCas and RCaCas powders are hydrated with D_2O (a-b) or H_2O (c-d). The error bars of samples measured at 293 K and 320 K are smaller than the symbol size.

3.3.2. ELASTIC INCOHERENT STRUCTURE FACTOR (EISF)

The elastic incoherent structure factor (EISF), which in essence is the area fraction of the delta function $EISF = A_0/(A_0 + A_{slow} + A_{fast})$, provides complementary information to the area fraction of the Lorentzians. We can extract quantitative information on the geometry of the atomic motion by fitting the Q-dependence of the EISF. For this purpose, we introduce the simple modified 'free diffusion in a sphere' model [37].

$$EISF = p + (1 - p)A$$

$$\text{With} \quad A = \int_0^\infty A_{sph} \cdot f(R, \sigma) dR$$

$$f(R, \sigma) = \frac{2}{\sqrt{2\pi\sigma^2}} \cdot e^{-\frac{R^2}{2\sigma^2}},$$

(3.2)

where p is the population of immobile protons and $A_{sph} = [\frac{3j_1(QR)}{QR}]^2$, with j_1 the first-order Bessel function of the first kind. The Gaussian distribution $f(R, \sigma)$ accounts for the heterogeneity of the samples [34] with σ the variance. The average diffusion radius of the sphere is $R_0 = \sigma\sqrt{\frac{2}{\pi}}$.

Fig. 3.2 shows the experimental results and the excellent fits to the data. The deduced parameters are given in Table 3.3. The population of the immobile protons p of all samples decreases as temperature increases. This trend is also consistent with the area fractions of the quasi-elastic amplitudes, which increase with increasing temperature. Interestingly, at 293 K, SCaCas hydrated with H_2O has significantly less immobile protons than the other samples. However, the difference between this sample and the rest reduces as temperature increases. This indicates that SCaCas hydrated with H_2O is the sample with the most mobile protons whereas high temperatures mitigate the solvent effect.

Table 3.3: Fitted values of p and R_0 of SCaCas and RCaCas hydrated with either D_2O or H_2O at 293 K, 320 K and 340 K.

		SCaCas/D_2O	RCaCas/D_2O	SCaCas/H_2O	RCaCas/H_2O
	293 K	0.49±0.04	0.46±0.04	0.36±0.02	0.43±0.03
p	320 K	0.40±0.05	0.41±0.04	0.31±0.01	0.37±0.02
	340 K	0.32±0.05	0.30±0.04	0.26±0.02	0.32±0.02
	293 K	1.8±0.2	1.7±0.2	2.7±0.1	2.3±0.2
R_0 (Å)	320 K	2.0±0.2	2.1±0.2	3.2±0.1	3.0±0.2
	340 K	2.1±0.2	2.1±0.2	3.6±0.3	3.1±0.2

The diffusion radius R_0 is about 1.9 Å for the D_2O hydrated samples, and 3.0 Å for the H_2O hydrated ones. Both radii are much larger than the reported value of 1 Å for the methyl-group rotation [38]. Thus, these radii probably implicate the hydrophilic side chains or the flexible regions of the protein that are participating in the motions. The radii of the D_2O hydrated samples are close to those of folded globular proteins such as lysozyme, myoglobin or GFP [8, 10, 39]. For the H_2O hydrated samples, the radii are similar to those of β-casein, tRNA and *E.coli* [12, 33, 40, 41].

The difference in the diffusion radii of H_2O and D_2O hydrated samples may be due to either the different incoherent cross sections of hydrogen and deuterium, or to the solvent effect. On the basis of our observations, we are inclined to attribute this effect to the latter. The reason is that the diffusion radius reflects the dynamics of the side chains rather than the dynamics of the H atoms. Given that the molecular mass of side chains is not affected substantially by deuteration, the difference in the diffusion radius must be attributed to the solvent effect. Furthermore, since proteins with open structures such as caseinate tend to have larger diffusion radii than proteins with well-defined folded structures, the fact that the radii of the D_2O hydrated samples are smaller than those of the H_2O hydrated ones indicates that a more hydrophobic environment constrains the diffusive motions of calcium caseinate.

The temperature dependence of mobile protons has been seen in many systems and has been attributed to protein denaturation or thermal unfolding [34, 40, 42]. Our preliminary differential scanning calorimetry data (supplementary information) show small bumps in the heat capacity of all the samples between 320 and 340K, which indicate structural changes. We attribute this phenomenon to the relaxation of hydrogen bond networks [43] and the swelling of protein aggregates [42], instead of to irreversible denaturation or thermal unfolding. The reasons are two-fold. One is that the diffusion radii increase with increasing temperature. This leads to larger diffusion volumes, which are likely to result from the swelling of caseinate aggregates and the breakage of hydrogen bonds at mild heating temperatures, such as below 340 K. On the other hand, when a protein with a well-defined structure undergoes an irreversible denaturation, its flexibility is constrained and its diffusion radius usually decreases [34, 40]. Consequently, the diffusion volume for the side-chains is reduced as well.

The other reason is related to the water content of the samples. Compared to dry powders, thermal unfolding is observed more often in solutions, since more solvents decrease the protein stability. On the one hand, the protein's freedom of movement is limited by the low water content [44]; on the other hand, more energy is needed to mobilize the first or second hydration layer, as these water molecules are tightly bound to the protein surface [45]. Given the low water content of our samples (0.4 g solvent/g dry powder), the temperature that would trigger irreversible denaturation is most likely higher than 340 K.

3.3.3. ELASTIC WINDOW SCAN

In order to follow the temperature dependence of the dynamics at the molecular scale, we performed elastic window scans up to temperatures above physiological conditions. From the measurements, we deduced both the elastic incoherent intensity ΔI_{el} and the mean-square atomic displacement (MSD) $\langle u^2 \rangle$. ΔI_{el} is calculated as the difference between the normalized elastic intensity of the hydrated and the dry samples: $\Delta I_{el} = \frac{I_{\text{hydrated}}(T)}{I_{\text{hydrated}}(20K)} - \frac{I_{\text{dry}}(T)}{I_{\text{dry}}(20K)}$. The MSD is obtained by fitting the elastic incoherent intensity using the Gaussian approximation: $\langle u^2 \rangle = -\frac{3}{Q^2} \ln[\frac{I_{el}(Q,T)}{I_{el}(Q,20K)}]$. ΔI_{el} is summed over all the Q's while the MSD is obtained from the Q-dependent I_{el}. Both parameters provide qualitative, complementary information of the dynamics of the samples.

The temperature dependence of ΔI_{el} is shown in Fig. 3.3(a). All samples display a sharp decrease of ΔI_{el} at around 250 K, which corresponds to the onset of protein anharmonic motions enabled by the presence of solvent [27, 43]. Below 250 K, the decrease of ΔI_{el} for the H_2O hydrated SCaCas is slightly more gradual than the others and starts at lower temperatures. Only RCaCas hydrated with H_2O shows an elastic intensity higher than the dry sample, which is consistent with the assumption that hydration increases the stiffness of the protein structure at low temperatures [10, 35]. Above 250 K, the slope of

$\langle u^2 \rangle$ vs. temperature shown in Fig. 3.3(b) provides an empirical indication of the protein flexibility and resilience, as suggested by Zaccai. et al [46, 47]. According to this work, the steeper the slope, the more flexible the protein structure, which implies that more conformational changes are possible. SCaCas hydrated with H_2O has a slightly steeper slope than the other samples, suggesting that it should be more prone to alignment under shear.
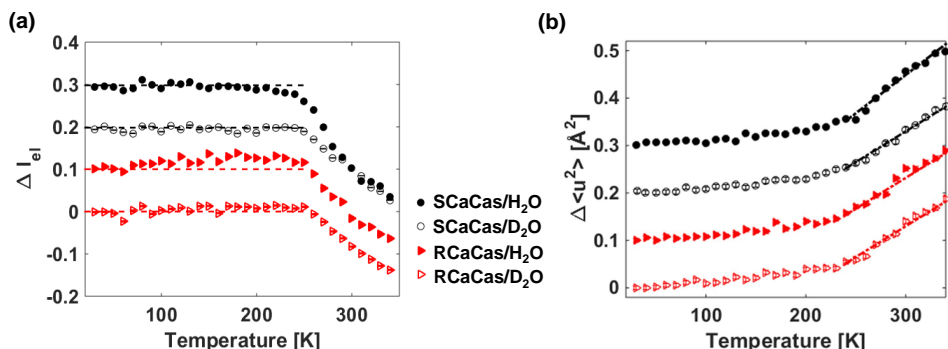

Figure 3.3: (a): Change of the elastic incoherent intensity ΔI_{el} as a function of temperature. (b): MSDs of the hydrated samples as a function of temperature. For clarity, the plots of RCaCas hydrated with H_2O (filled triangle), SCaCas hydrated with D_2O (hollow circle) and H_2O (filled circle) are shifted by 0.1, 0.2 and 0.3, respectively. The dashed lines are guides to the eye.

3.4. DISCUSSION

This study has been initiated by the experimental observation that the isotope effect of solvent alters the fibre formation in calcium caseinate. The QENS investigation presented above reveals systematic differences at the microscopic scale. To connect the macroscopic findings with the microscopic results, we will discuss below some important aspects.

1) Hydration scenario of the calcium caseinate powder.
It is generally agreed that the four sub-caseins in caseinate [Fig. 3.4(a)] [49] self-assemble into an open, micelle-like structure in solution [Fig. 3.4(b)] [50]. Different drying methods used to obtain the protein powder cause the micelle-like structure to collapse into compact aggregates [Fig. 3.4(c)]. This suggests that little space is available for diffusive motions, which is in line with the FWHMs of the Lorentzians that point to only re-orientational, localized motions. Moreover, though the micelle-like structure is regarded as 'open', it is unlikely that water molecules diffuse freely into the hydrophobic core during hydration of the powder [Fig. 3.4(d)]. Based on these structural considerations, we discuss two possible explanations for the quasi-elastic amplitudes. One is that the fast and slow Lorentzians correspond to the small and large protein side-groups respectively. However, if this would have been the case, one would expect the trend in the area fraction with temperature to be the same for different solvents. This is not in line
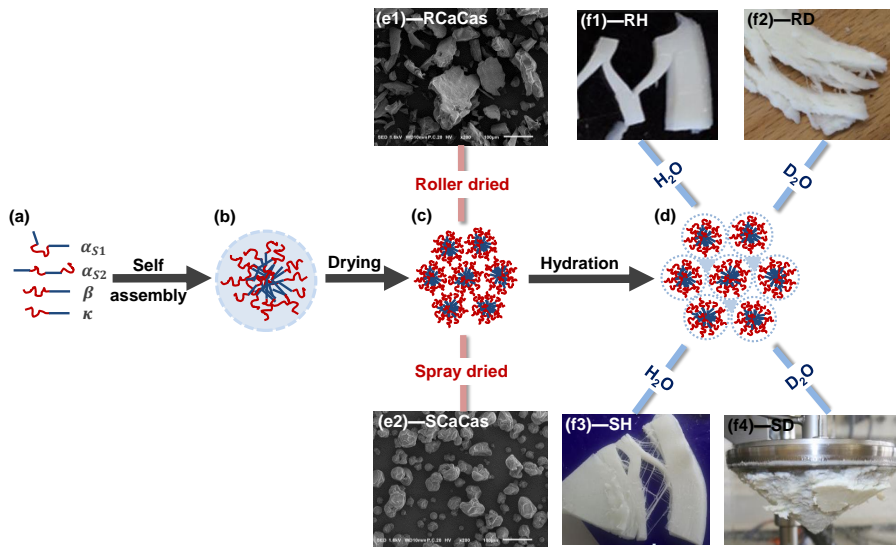
Figure 3.4: Schematic illustration of the status of the calcium caseiante aggregates from solution (a-b) to dried powders (c and e) and to re-hydration with different solvents (d and f). (a): the four sub-caseins are depicted according to the Horne. et al [48], where the straight lines represent the hydrophobic region and the twisting lines represent the hydrophilic region. (b): a simplified depiction of one micelle-like aggregate in solution before drying, based on the model from the de Kruif [28]. Note, Ca^{2+} ions distribute homogeneously inside the aggregates, but are not shown in the drawing since they are not the interest of this discussion. (c): after drying, the micelle-like aggregates collapse into bigger aggregates that form the powder particle. (d): after hydration, each individual aggregate is surrounded by a thin layer of solvent (blue dashed lines), with some free solvent dispersed in between (blue triangle). (e): Scanning electron microscopy images of dried RCaCas (e1) and SCaCas (e2) powders. (f1-2): pictures of RCaCas gels made with H_2O and D_2O; (f3-4): pictures of SCaCas gels made with H_2O and D_2O.

with the experimental results, as the L_{slow} of H_2O hydrated samples remains unchanged with increasing temperature while it increases for D_2O. The other possible explanation is that the fast Lorentzian represents the motions of protein groups that are exposed to the solvent (i.e. hydrophilic groups) and that the slow Lorentzian represents the groups that are not accessible to the solvent (i.e. hydrophobic groups). This explanation is in line with the experimental observations, as the area fraction of L_{slow} is much higher than that of L_{fast}, reflecting the fact that there are more hydrophobic sub-caseins ($\alpha_{s1,s2}$-, and β-casein) than hydrophilic sub-caseins (κ-casein). In the following, we will adopt this assumption and consider that the fast and slow Lorentzians represent the hydrophilic and hydrophobic side-groups of caseinate respectively.

2) Representativeness of the measured hydration level.
A hydration level of h=0.4(weight solvent/weight dry protein powder) is generally regarded as sufficient to have the protein surface completely covered by at least 1 layer of water molecules [27]. This first hydration layer is considered to be bound or non-freezable [51]. In the actual production of the fibrous material, a higher hydration level of h=2.3 is used. Thus, it might be questionable whether the protein dynamics at h=0.4 is representative of the dynamics at higher hydration levels. In this respect we note that one caseinate aggregate is larger than a globular protein and thus has a lower surface to volume ratio. Therefore, in that case, h=0.4 would lead to more than 1 layer of hydration water. This is also confirmed experimentally, as we observe Bragg peaks from crystalline D_2O at 20 K, using the additional diffraction detector from IRIS (supplementary information). Furthermore, the water activity of milk protein powder follows a sigmoidal increase with hydration content [52, 53]. Based on the moisture sorption isotherm, the water activity of the powder exceeds 0.9 when h=0.4, a state where water is freezable. We thus concluded that the observed dynamics at h=0.4 are representative for the behaviour at higher hydration level.

3) Effect of the drying history on the activity of the protein.
Fig. 3.4(e1, e2) shows a clear difference in the powder morphology of roller and spray dried calcium caseinate on the micrometer length scales. It is therefore likely that the arrangements of the sub-micelles and micelle-like aggregates are also different. This is indirectly reflected in the QENS results where the dynamics between the dry powders are different. At room temperature, SCaCas has longer relaxation times than RCaCas. The relaxation times of SCaCas shorten with increasing temperature, while they remain unchanged for RCaCas. We assume that the drying history explains these discrepancies. RCaCas went through a longer heating time and at higher temperatures during drying than SCaCas. Longer times give the protein more possibilities to re-order into a thermodynamically more favourable state. In addition, a more intensive heating process may modify the micelle arrangement and even damage certain side-groups. As a result, RCaCas has probably a different structure or less active side-groups than SCaCas, which explains why its FWHMs are less affected by temperature.

4) Solvent isotope effect on caseinate fibre formation.
The most distinct macroscopic difference lies in the appearance of the fibrous gels. The

use of H_2O results in intact and homogeneous gels in both RCaCas (RH) and SCaCas (SH) [Fig. 3.4(f1, f3)]; On the other hand, D_2O leads to a paste with inconsistent texture and expelled water [Fig. 3.4(f2, f4)]. Poor gelation behaviour can be due to a reduced water binding capacity and/or to a strong hydrophobic interaction. This is not surprising as it is indeed assumed that D_2O suppresses the dynamic motion between intra-protein hydrogen bonds [54] and promotes hydrophobic interaction [55]. Our QENS results also support this assumption as L_{slow} is smaller in D_2O hydrated samples, suggesting that less protons are mobile in the hydrophobic cores, since it requires a higher activation energy to break the hydrogen bonds in D_2O than H_2O. Furthermore, with increasing temperature, L_{slow} increases in the D_2O hydrated samples, whereas it remains constant in the H_2O hydrated ones. This difference may be due to the subtle changes of weak interactions (e.g. hydrophobic interaction, hydrogen bonding, Van der Waals interactions) [28] inside the hydrophobic cores. Higher temperatures indeed increase the hydrophobic interaction but also facilitate the breakage of hydrogen bonds which gives rise to more mobile protons. Therefore, the counterbalance in these weak interactions may be responsible for the different behaviour of L_{slow}.

As a final remark, the H_2O hydrated SCaCas behaves differently from the rest of the samples: it has the highest quasi-elastic amplitudes (section 3.3.1), the largest population of mobile protons, the largest diffusion radius (section 3.3.2), and the steepest slope of MSD above 250 K (section 3.3.3). These results imply that this sample combines a higher proton mobility with a higher diffusion amplitude, which are both beneficial to protein aggregates interactions. As a more flexible structure is important for the alignment of the aggregates upon deformation, our study provides a strong link between the dynamics probed by QENS and the macroscopic fibre formation in calcium caseinate.

3.5. CONCLUSION

Our QENS investigation sheds light on the solvent isotope effect of H_2O and D_2O on two industrially obtained protein powders: roller dried (RCaCas) and spray dried (SCaCas) calcium caseinate at physiological temperatures.

We analysed the data using a phenomenological model assuming two independent dynamical processes. A first result concerns the dry powder, the behaviour of which depends very much on the drying method. The relaxation times of the dry SCaCas are longer than of the dry RCaCas at room temperature, and they shorten with increasing temperature. The higher susceptibility of SCaCas to temperature may be due to the milder drying conditions.

The results of the hydrated powders show two re-orientational, picosecond motions: a fast one Γ_{fast} attributed to the external, hydrophilic protein groups and a slow one Γ_{slow} representing the internal, hydrophobic and solvent non-accessible regions.

The solvent isotope effect is found mostly in the quasi-elastic amplitudes and less in the relaxation times. The D_2O hydrated samples have less mobile protons at the hydropho-

bic cores, as D_2O promotes hydrophobic interaction. The EISF results are in agreement with these findings, because samples hydrated with D_2O have less mobile protons and smaller diffusion radii. Temperature mitigates the solvent isotope effect by altering the weak interactions inside the micelles. In addition, the analysis of the elastic window scan suggests that SCaCas hydrated with H_2O has a lower onset temperature of the dynamic transition and a more flexible conformation than the other samples. This sample also has the most anisotropic fibres.

To summarise, with QENS we were able to distinguish the dynamics between powders dried using different methods, and we could detect the solvent isotope effect of hydrated powders. We have thus established a correlation between the differences of the protein dynamics on the microscopic level and the resulting different bulk fibre structures.

3.6. SUPPLEMENTARY INFORMATION

FITTING THE QENS DATA

We started off by fitting the QENS data of both the H_2O and D_2O hydrated samples with 1 Lorentzian function. The residuals of the fits from figure 3.5 & 3.6 showed a clear trend, suggesting 1 Lorentzian is insufficient to describe the features in the data.

As a result, we re-fitted the spectra with 2 Lorentzian functions. It turned out that 2 Lorentzians were over-fitting the D_2O hydrated samples at 293 K and 320 K. This is probably because the slow motion has not yet entered the instrument resolution at these temperatures. Since our primary interest in this study is to compare the dynamics of proteins affected by solvent, we used a constant value of the Full Width Half Maximum (FWHM) Γ of the narrow Lorentzian in order to obtain the FWHM of the broad Lorentzian. These values are the same as the Γ_{narrow} of the H_2O hydrated samples. This approach is justified by the fact that the FWHMs of the H_2O hydrated samples are very similar to the D_2O ones at 340 K, which is shown in figure 3.7. This figure also showed that the FWHMs of both Lorentzians are Q-independent in all samples. Thus, we decided to sum all the detectors to get a more accurate value of Γ. The fit of the summed detectors are presented in figure 3.8, 3.9 & 3.10, the residuals no longer show any trend. Note, the dry powders are also fitted with 2 Lorentzians because their residuals showed a clear trend when fitting the summed detectors with 1 Lorentzian.

DIFFERENTIAL SCANNING CALORIMETRY

The heat flows of the hydrated powders were measured using a differential scanning calorimetry (DSC) Q2000 C24.11. After reaching a hydration level of 0.4 g solvent/g dry powder, around 12 mg of the sample is sealed in an aluminium hermetic cell for the measurement. The reference is an empty hermetic cell. The sample is first cooled to -85 °C, and then equilibrated for 2 minutes. Afterwards, the temperature ramps to 85 °C at a speed of 5 °C/min. At least three triplicates are performed for each sample.

The calculated heat capacities are shown in figure 3.11. It appears that the reproducibility is not very good, probably due to an uneven hydration of the protein powders. Since the sample volume is very small in a DSC measurement, it is likely that the hydration is different in the different samples. Nevertheless, it is clear that nearly all the samples show a sharp peak below 0 °C, suggesting melting of the ice. Moreover, the samples show small bumps between 50-70 °C, indicative of structural changes.

EVIDENCE OF FREE WATER

Figure 3.12 showed the diffraction pattern of the D_2O hydrated samples at 20 K. According to the user manual of the IRIS instrument at ISIS, three Bragg peaks that are characteristic to crystallined D_2O can be identified, thus suggesting the presence of frozen water. Since structural water or water that tightly bound to protein is regarded as non-freezable, these Bragg peaks can only be from water that are loosely bound or free.
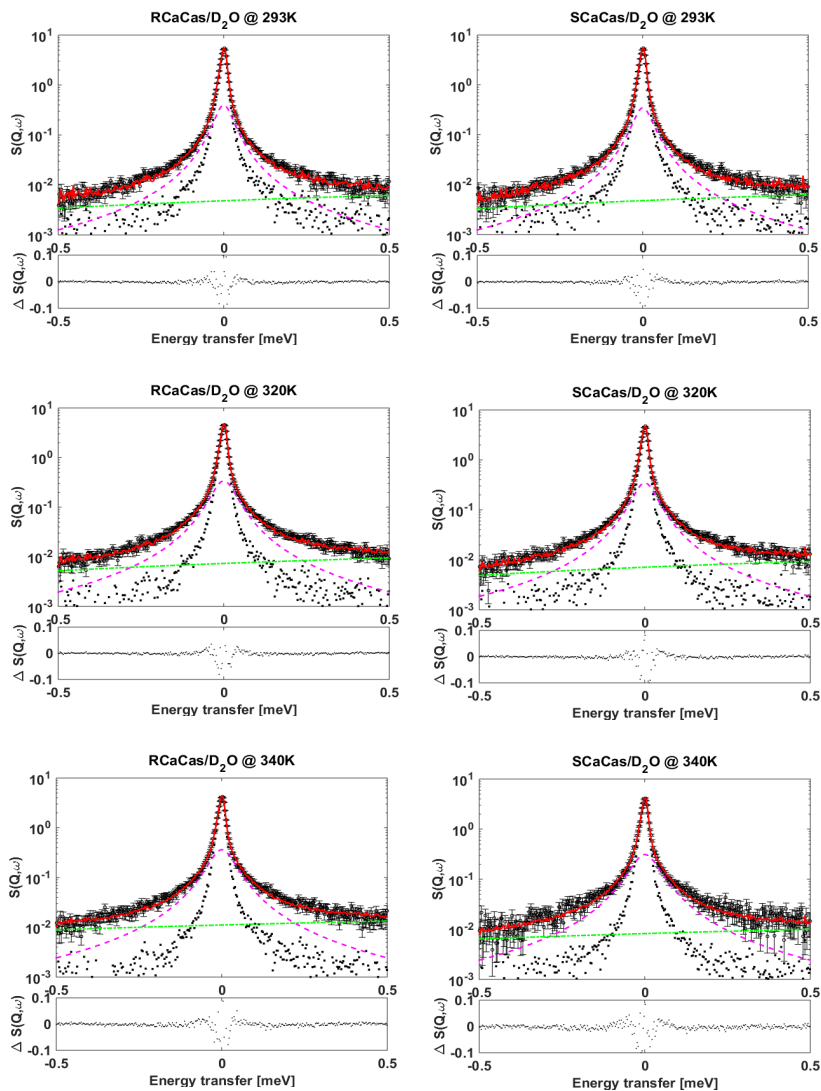
Figure 3.5: QENS spectra of D_2O hydrated powders fitted with 1 Lorentzian function at $Q = 1.45$ Å. Left column from top to bottom: Roller dried samples measured at 293 K, 320 K and 340 K; right column from top to bottom: Spray dried samples measured at 293 K, 320 K and 340 K. The delta function is presented by black dots, the Lorentzian function is dashed lines in magenta; the background is dot dashed lines in green. The sum of fits are lines in red. The residuals of the fits are underneath each spectrum.
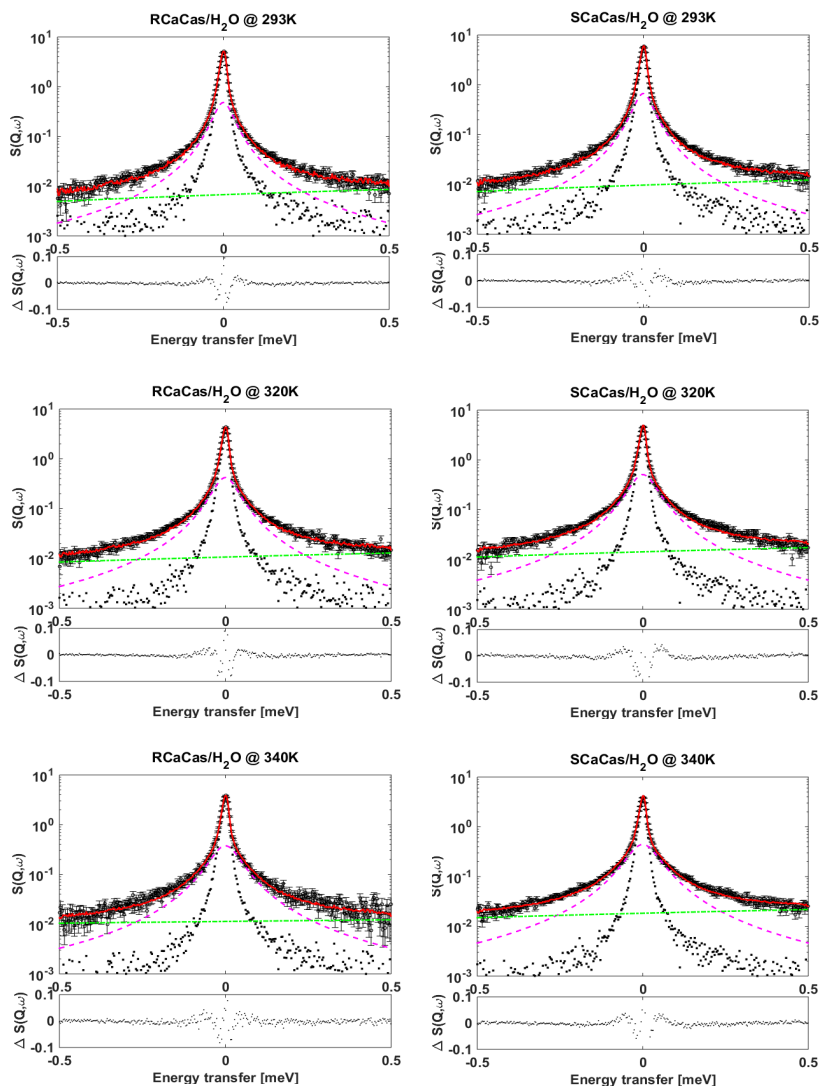
Figure 3.6: QENS spectra of H_2O hydrated powders fitted with 1 Lorentzian function at $Q = 1.45$ Å. Left column from top to bottom: Roller dried samples measured at 293 K, 320 K and 340 K; right column from top to bottom: Spray dried samples measured at 293 K, 320 K and 340 K. The delta function is presented by black dots, the Lorentzian function is dashed lines in magenta; the background is dot dashed lines in green. The sum of fits are lines in red. The residuals of the fits are underneath each spectrum.
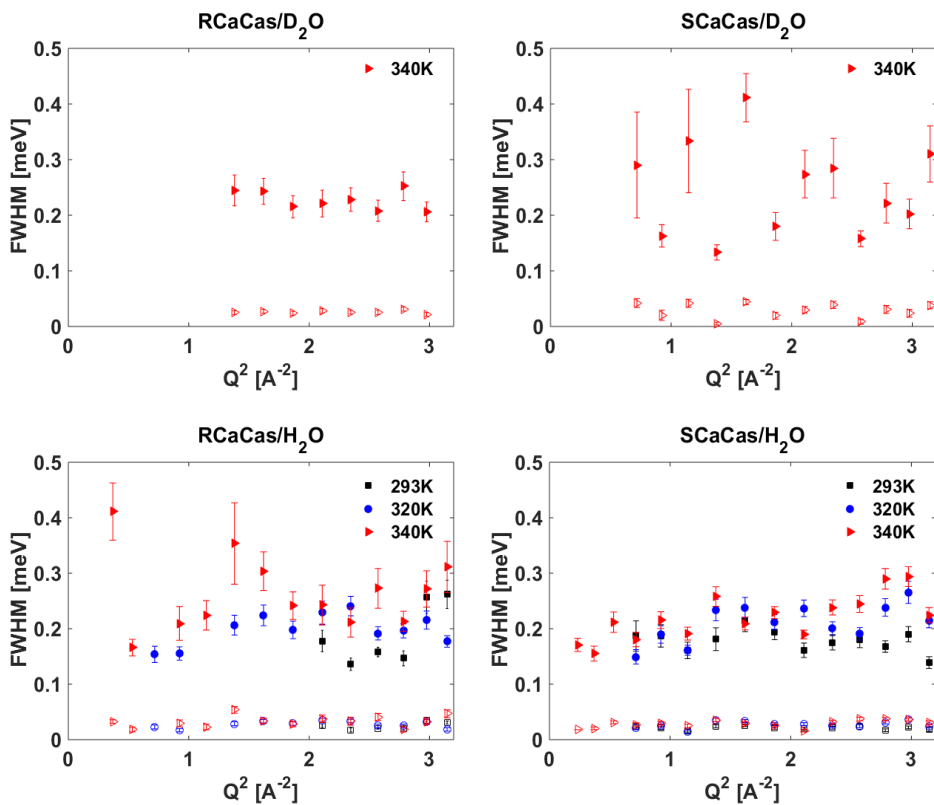
3

Figure 3.7: FWHMs of D_2O (top row) and H_2O (bottom row) hydrated samples as a function of Q^2. Two Lorentzian functions were used to fit the data measured at 293 K (square), 320 K (circle) and 340K (triangle). The FWHMs of the narrow Lorentzian is represented by hollow symbols, while the FWHMs of the broad Lorentzian is represented by filled symbols. Since at 293 K and 320 K, the two Lorentzians were over fitting the D_2O hydrated samples, only data at 340 K are shown.
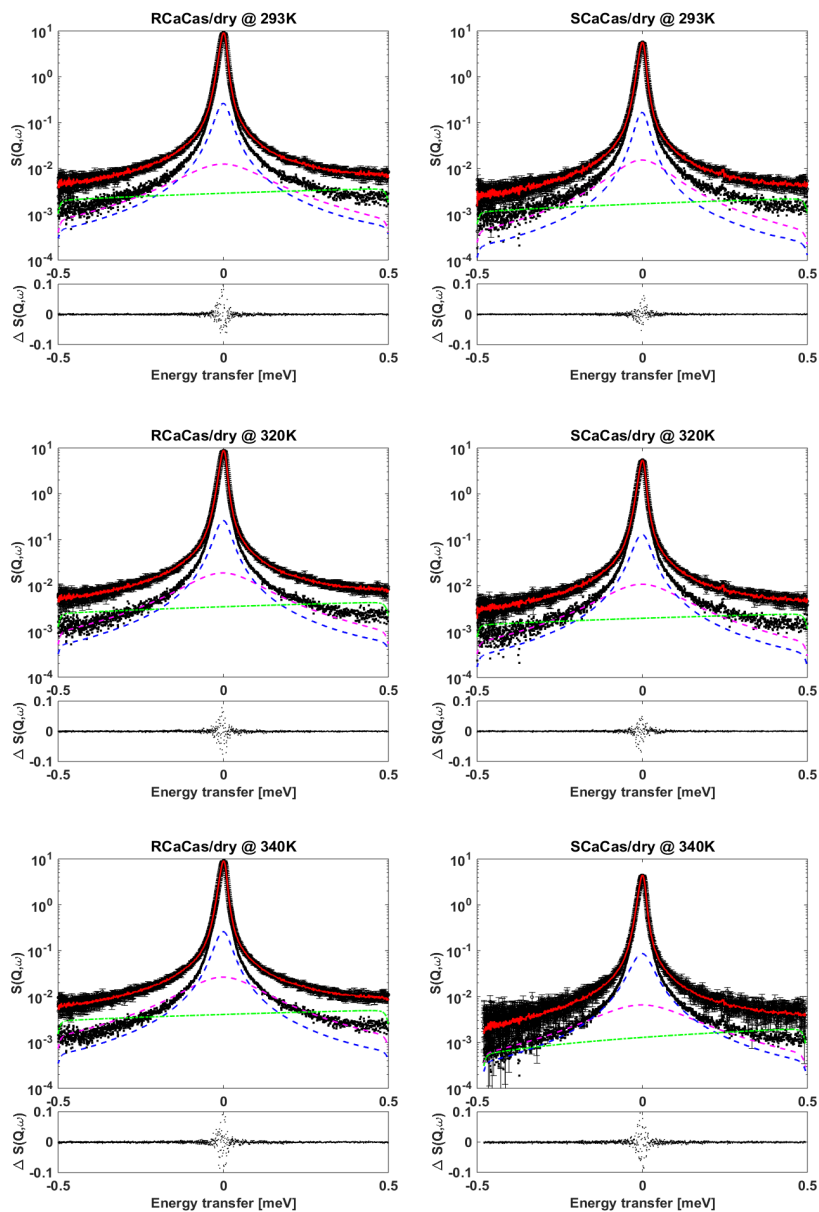
Figure 3.8: QENS spectra of dry powders fitted with 2 Lorentzian functions with summed detectors. Left column from top to bottom: Roller dried samples measured at 293 K, 320 K and 340 K; right column from top to bottom: Spray dried samples measured at 293 K, 320 K and 340 K. The delta function is presented by black dots, the broad Lorentzian function is dashed lines in magenta, the narrow Lorentzian function is dashed lines in blue; the background is dot dashed lines in green. The sum of fits are lines in red. The residuals of the fits are underneath each spectrum.
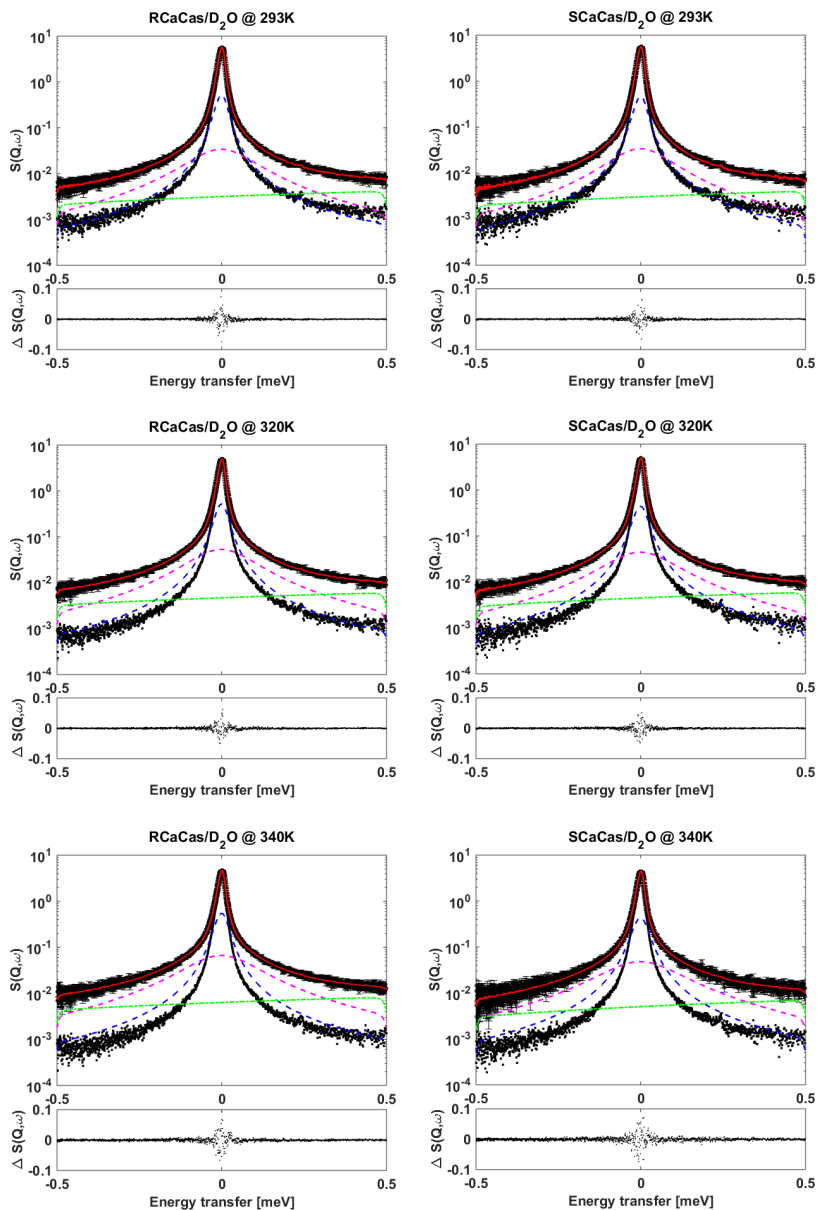
Figure 3.9: QENS spectra of D_2O hydrated powders fitted with 2 Lorentzian functions with summed detectors. Left column from top to bottom: Roller dried samples measured at 293 K, 320 K and 340 K; right column from top to bottom: Spray dried samples measured at 293 K, 320 K and 340 K. The delta function is presented by black dots, the broad Lorentzian function is dashed lines in magenta, the narrow Lorentzian function is dashed lines in blue; the background is dot dashed lines in green. The sum of fits are lines in red. The residuals of the fits are underneath each spectrum.
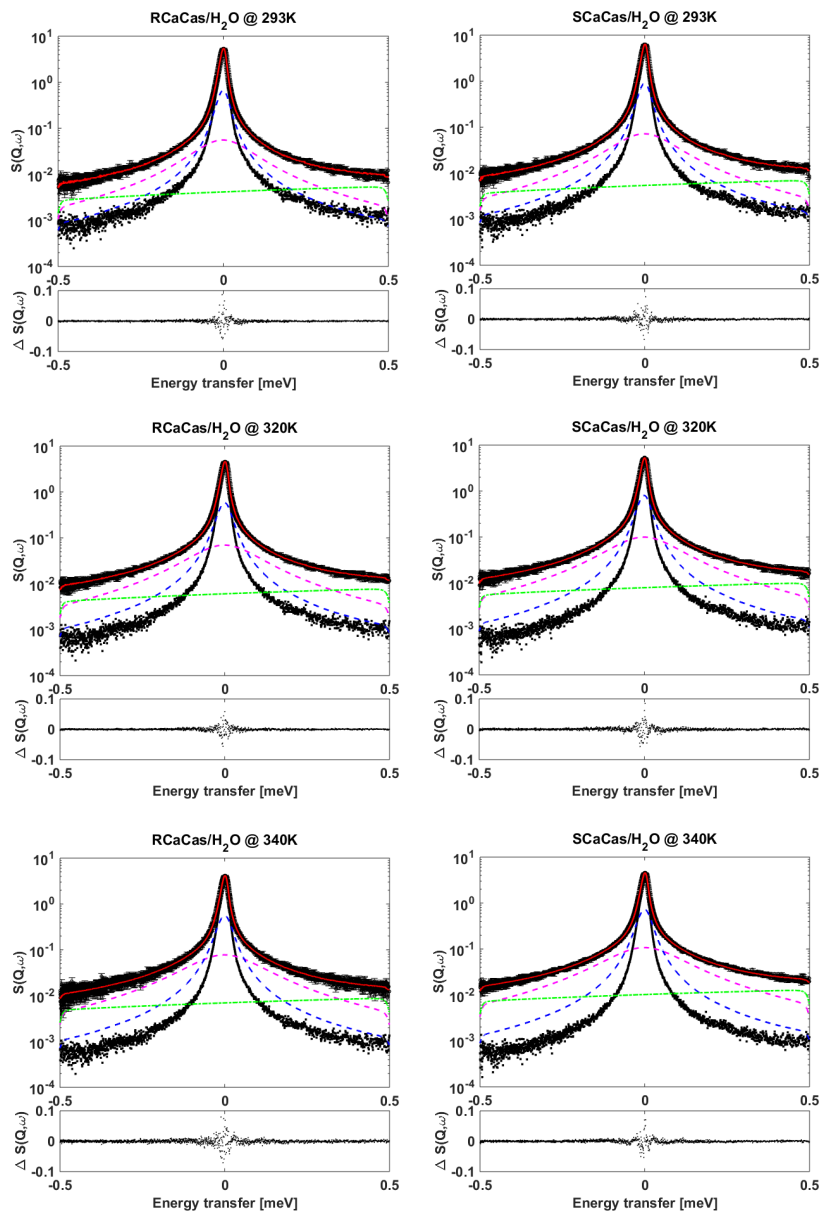
Figure 3.10: QENS spectra of H_2O hydrated powders fitted with 2 Lorentzian functions with summed detectors. Left column from top to bottom: Roller dried samples measured at 293 K, 320 K and 340 K; right column from top to bottom: Spray dried samples measured at 293 K, 320 K and 340 K. The delta function is presented by black dots, the broad Lorentzian function is dashed lines in magenta, the narrow Lorentzian function is dashed lines in blue; the background is dot dashed lines in green. The sum of fits are lines in red. The residuals of the fits are underneath each spectrum.
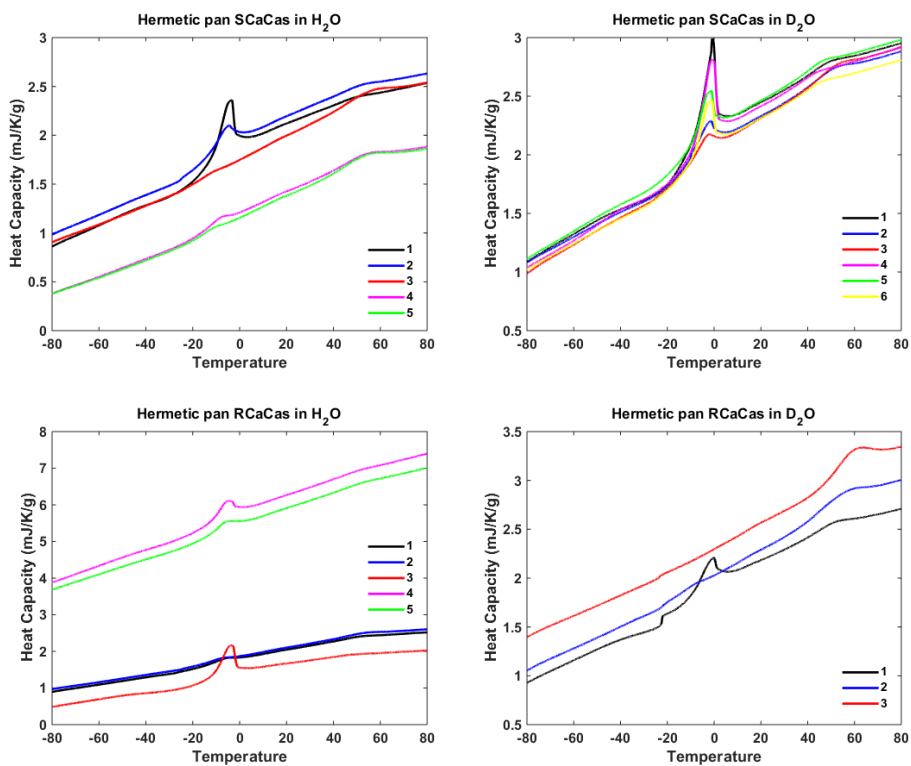
Figure 3.11: Heat capacities of the four samples as a function of increasing temperatures. The top row is spray dried calcium caseinate hydrated with H_2O (left) and D_2O (right), the bottom row is roller dried calcium caseinate.
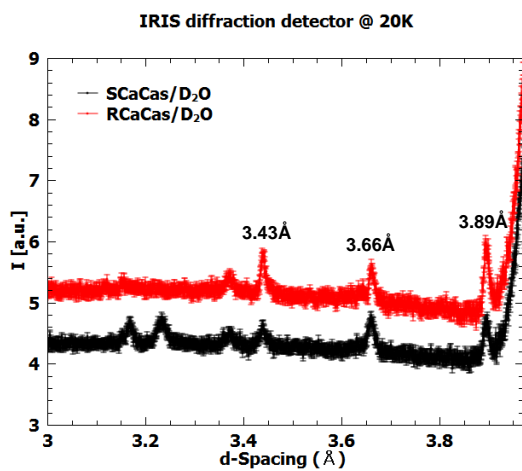
Figure 3.12: Diffraction peaks of D_2O hydrated samples measured at 20 K. Both RCaCas and SCaCas have peaks at 3.43 Å, 3.66 Å and 3.89 Å, which are characteristic to crystallined D_2O.

REFERENCES

[1] B. Tian, V. G. Sakai, C. Pappas, A. J. van der Goot, and W. G. Bouwman, *Fibre formation in calcium caseinate influenced by solvent isotope effect and drying method–a neutron spectroscopy study,* Chemical Engineering Science **207**, 1270 (2019).

[2] J. M. Manski, A. J. van der Goot, and R. M. Boom, *Advances in structure formation of anisotropic protein-rich foods through novel processing concepts,* Trends in Food Science & Technology **18**, 546 (2007).

[3] J. M. Manski, A. J. van der Goot, and R. M. Boom, *Formation of fibrous materials from dense calcium caseinate dispersions,* Biomacromolecules **8**, 1271 (2007).

[4] Z. Wang, B. Tian, R. Boom, and A. J. van der Goot, *Air bubbles in calcium caseinate fibrous material enhances anisotropy,* Food hydrocolloids **87**, 497 (2019).

[5] B. L. Dekkers, C. V. Nikiforidis, and A. J. van der Goot, *Shear-induced fibrous structure formation from a pectin/spi blend,* Innovative Food Science & Emerging Technologies **36**, 193 (2016).

[6] B. Tian, Z. Wang, A. J. van der Goot, and W. G. Bouwman, *Air bubbles in fibrous caseinate gels investigated by neutron refraction, x-ray tomography and refractive microscope,* Food Hydrocolloids **83**, 287 (2018).

[7] S. Magazù, F. Migliardo, and A. Benedetto, *Mean square displacements from elastic incoherent neutron scattering evaluated by spectrometers working with different energy resolution on dry and hydrated (H_2O and D_2O) lysozyme,* The Journal of Physical Chemistry B **114**, 9268 (2010).

[8] J. H. Roh, J. E. Curtis, S. Azzam, V. N. Novikov, I. Peral, Z. Chowdhuri, R. B. Gregory, and A. P. Sokolov, *Influence of hydration on the dynamics of lysozyme,* Biophysical journal **91**, 2573 (2006).

[9] W. Doster, S. Cusack, and W. Petry, *Dynamical transition of myoglobin revealed by inelastic neutron scattering,* Nature **337**, 754 (1989).

[10] J. D. Nickels, H. O'Neill, L. Hong, M. Tyagi, G. Ehlers, K. L. Weiss, Q. Zhang, Z. Yi, E. Mamontov, J. C. Smith, *et al.*, *Dynamics of protein and its hydration water: neutron scattering studies on fully deuterated GFP,* Biophysical journal **103**, 1566 (2012).

[11] G. Caliskan, R. M. Briber, D. Thirumalai, V. Garcia-Sakai, S. A. Woodson, and A. P. Sokolov, *Dynamic transition in tRNA is solvent induced,* Journal of the American Chemical Society **128**, 32 (2006).

[12] J. H. Roh, R. M. Briber, A. Damjanovic, D. Thirumalai, S. A. Woodson, and A. P. Sokolov, *Dynamics of tRNA at different levels of hydration,* Biophysical journal **96**, 2755 (2009).

[13] S. H. Chen, L. Liu, X. Chu, Y. Zhang, E. Fratini, P. Baglioni, A. Faraone, and E. Mamontov, *Experimental evidence of fragile-to-strong dynamic crossover in DNA hydration water,* The journal of chemical physics **125**, 171103 (2006).

[14] J. Fitter, R. E. Lechner, and N. A. Dencher, *Interactions of hydration water and biological membranes studied by neutron scattering,* The Journal of Physical Chemistry B **103**, 8036 (1999).

[15] J. Sjöström, F. Kargl, F. Fernandez-Alonso, and J. Swenson, *The dynamics of water in hydrated white bread investigated using quasielastic neutron scattering,* Journal of Physics: Condensed Matter **19**, 415119 (2007).

[16] H. Jansson, W. S. Howells, and J. Swenson, *Dynamics of fresh and freeze-dried strawberry and red onion by quasielastic neutron scattering,* The Journal of Physical Chemistry B **110**, 13786 (2006).

[17] C. S. Kealley, A. V. Sokolova, G. J. Kearley, E. Kemner, M. Russina, A. Faraone, W. A. Hamilton, and E. P. Gilbert, *Dynamical transition in a large globular protein: Macroscopic properties and glass transition,* Biochimica et Biophysica Acta (BBA)-Proteins and Proteomics **1804**, 34 (2010).

[18] A. Orecchini, A. Paciaroni, A. R. Bizzarri, and S. Cannistraro, *Dynamics of different hydrogen classes in β-lactoglobulin: a quasielastic neutron scattering investigation,* The Journal of Physical Chemistry B **106**, 7348 (2002).

[19] A. M. Stadler, E. Pellegrini, M. Johnson, J. Fitter, and G. Zaccai, *Dynamics-stability relationships in apo-and holomyoglobin: a combined neutron scattering and molecular dynamics simulations study,* Biophysical journal **102**, 351 (2012).

[20] F. Ameseder, A. Radulescu, M. Khaneft, W. Lohstroh, and A. M. Stadler, *Homogeneous and heterogeneous dynamics in native and denatured bovine serum albumin,* Physical Chemistry Chemical Physics **20**, 5128 (2018).

[21] C.-L. Hsu, W. Chen, Y.-M. Weng, and C.-Y. Tseng, *Chemical composition, physical properties, and antioxidant activities of yam flours as affected by different drying methods,* Food chemistry **83**, 85 (2003).

[22] I. Claussen, I. Strømmen, B. Egelandsdal, and K. Strætkvern, *Effects of drying methods on functionality of a native potato protein concentrate,* Drying technology **25**, 1091 (2007).

[23] P. Luck, B. Vardhanabhuti, Y. Yong, T. Laundon, D. Barbano, and E. Foegeding, *Comparison of functional properties of 34% and 80% whey protein and milk serum protein concentrates,* Journal of dairy science **96**, 5522 (2013).

[24] O. Caparino, J. Tang, C. Nindo, S. Sablani, J. Powers, and J. Fellman, *Effect of drying methods on the physical properties and microstructures of mango (philippine 'carabao'var.) powder,* Journal of Food Engineering **111**, 135 (2012).

[25] C. Ratti, *Hot air and freeze-drying of high-value foods: a review,* Journal of food engineering **49**, 311 (2001).

3

[26] D. Dehnad, S. M. Jafari, and M. Afrasiabi, *Influence of drying on functional properties of food biopolymers: From traditional to novel dehydration techniques,* Trends in food science & technology **57**, 116 (2016).

[27] F. Gabel, D. Bicout, U. Lehnert, M. Tehei, M. Weik, and G. Zaccai, *Protein dynamics studied by neutron scattering,* Quarterly reviews of biophysics **35**, 327 (2002).

[28] C. G. De Kruif, T. Huppertz, V. S. Urban, and A. V. Petukhov, *Casein micelles and their internal structure,* Advances in Colloid and Interface Science **171**, 36 (2012).

[29] B. Ingham, G. D. Erlangga, A. Smialowska, N. M. Kirby, C. Wang, L. Matia-Merino, R. G. Haverkamp, and A. J. Carr, *Solving the mystery of the internal structure of casein micelles,* Soft matter **11**, 2723 (2015).

[30] C. J. Carlile and M. A. Adams, *The design of the IRIS inelastic neutron spectrometer and improvements to its analysers,* Physica B: Condensed Matter **182**, 431 (1992).

[31] O. Arnold, J.-C. Bilheux, J. M. Borreguero, A. Buts, S. I. Campbell, L. Chapon, M. Doucet, N. Draper, R. F. Leal, M. A. Gigg, *et al.*, *Mantid—Data analysis and visualization package for neutron scattering and μ SR experiments,* Nuclear Instruments and Methods in Physics Research Section A: Accelerators, Spectrometers, Detectors and Associated Equipment **764**, 156 (2014).

[32] R. T. Azuah, L. R. Kneller, Y. Qiu, P. L. W. Tregenna-Piggott, C. M. Brown, J. R. D. Copley, and R. M. Dimeo, *DAVE: a comprehensive software suite for the reduction, visualization, and analysis of low energy neutron spectroscopic data,* Journal of Research of the National Institute of Standards and Technology **114**, 341 (2009).

[33] M. Jasnin, M. Moulin, M. Haertlein, G. Zaccai, and M. Tehei, *In vivo measurement of internal and global macromolecular motions in Escherichia coli,* Biophysical Journal **95**, 857 (2008).

[34] D. Russo, J. Pérez, J.-M. Zanotti, M. Desmadril, and D. Durand, *Dynamic transition associated with the thermal denaturation of a small beta protein,* Biophysical journal **83**, 2792 (2002).

[35] K. Wood, C. Caronna, P. Fouquet, W. Haussler, F. Natali, J. Ollivier, A. Orecchini, M. Plazanet, and G. Zaccai, *A benchmark for protein dynamics: Ribonuclease a measured by neutron scattering in a large wavevector-energy transfer range,* Chemical physics **345**, 305 (2008).

[36] Z. Bu, J. Cook, and D. J. E. Callaway, *Dynamic regimes and correlated structural dynamics in native and denatured α-lactalbumin,* Journal of molecular biology **312**, 865 (2001).

[37] F. Volino and A. J. Dianoux, *Neutron incoherent scattering law for diffusion in a potential of spherical symmetry: general formalism and application to diffusion inside a sphere,* Molecular Physics **41**, 271 (1980).

[38] B. Frick and L. J. Fetters, *Methyl group dynamics in glassy polyisoprene: a neutron backscattering investigation,* Macromolecules **27**, 974 (1994).

[39] J. Pérez, J.-M. Zanotti, and D. Durand, *Evolution of the internal dynamics of two globular proteins from dry powder to solution,* Biophysical journal **77**, 454 (1999).

[40] G. K. Dhindsa, M. Tyagi, and X.-q. Chu, *Temperature-dependent dynamics of dry and hydrated β-casein studied by quasielastic neutron scattering,* The Journal of Physical Chemistry B **118**, 10821 (2014).

[41] S. Perticaroli, J. D. Nickels, G. Ehlers, E. Mamontov, and A. P. Sokolov, *Dynamics and rigidity in an intrinsically disordered protein, β-casein,* The Journal of Physical Chemistry B **118**, 7317 (2014).

[42] G. Gibrat, F. L. Assairi, Y. Blouquit, C. T. Craescu, and M.-C. Bellissent-Funel, *Biophysical study of thermal denaturation of apo-calmodulin: dynamics of native and unfolded states,* Biophysical journal **95**, 5247 (2008).

[43] W. Doster, M. Settles, *et al., The dynamical transition in proteins: the role of hydrogen bonds,* NATO ASI SERIES A LIFE SCIENCES **305**, 177 (1999).

[44] C. Anandharamakrishnan, C. Rielly, and A. Stapley, *Effects of process variables on the denaturation of whey proteins during spray drying,* Drying Technology **25**, 799 (2007).

[45] A. Colombo, P. D. Ribotta, and A. E. LEOn, *Differential scanning calorimetry (dsc) studies on the thermal properties of peanut proteins,* Journal of agricultural and food chemistry **58**, 4434 (2010).

[46] G. Zaccai, *How soft is a protein? A protein dynamics force constant measured by neutron scattering,* Science **288**, 1604 (2000).

[47] G. Zaccai, *Neutron scattering perspectives for protein dynamics,* Journal of Non-Crystalline Solids **357**, 615 (2011).

[48] D. S. Horne, *Casein micelles as hard spheres: limitations of the model in acidified gel formation,* Colloids and Surfaces A: Physicochemical and Engineering Aspects **213**, 255 (2003).

[49] D. S. Horne, *Casein structure, self-assembly and gelation,* Current Opinion in Colloid & Interface Science **7**, 456 (2002).

[50] C. Holt, *Structure and stability of bovine casein micelles,* Advances in protein chemistry **43**, 63 (1992).

[51] J. Kinsella, *Relationships between structure and functional properties of food proteins,* Food proteins **1**, 51 (1982).

[52] M. K. Haque and Y. H. Roos, *Water sorption and plasticization behavior of spray-dried lactose/protein mixtures,* Journal of food science **69**, E384 (2004).

[53] E. Ostrowska-Ligeza, E. Jakubczyk, A. Górska, M. Wirkowska, and J. Bryś, *The use of moisture sorption isotherms and glass transition temperature to assess the stability of powdered baby formulas,* Journal of Thermal Analysis and Calorimetry **118**, 911 (2014).

[54] S.-Y. Sheu, E. Schlag, H. Selzle, and D.-Y. Yang, *Molecular dynamics of hydrogen bonds in protein- d2o: the solvent isotope effect,* The journal of physical chemistry A **112**, 797 (2008).

[55] Y. Efimova, S. Haemers, B. Wierczinski, W. Norde, and A. Van Well, *Stability of globular proteins in h2o and d2o,* Biopolymers **85**, 264 (2007).

3

4

THE SCATTERING FROM ORIENTED OBJECTS ANALYSED BY THE ANISOTROPIC GUINIER-POROD MODEL

Anisotropy is introduced to the Guinier-Porod model to describe the 2D scattering from oriented objects. This empirical model is first applied to approximate the scattering from oriented cylinders. It is then used to describe the anisotropic scattering from fibres in a protein gel. The orientation distribution and sizes of fibres can be obtained through simultaneously fitting two perpendicular sector intensities. Fitted results are in good agreement with microscopy images from previous works. With a slight modification, the model can also approximate the scattering from oriented ellipsoids. Lastly, a generalised form of the anisotropic Guinier-Porod model is proposed.

4.1. INTRODUCTION

Many samples display anisotropy in their two-dimensional (2D) small-angle scattering (SAS) patterns. Anisotropy can be introduced through compression, particle alignment under shear flow or orientation in a magnetic field [1–3]. The resulting anisotropic SAS pattern will contain few features when samples are composed of less well defined objects such as protein, or when they are less well oriented.

There are in general three approaches to extract information from 2D SAS data. One is to fit the data with a shape-dependent model. A size distribution is often included to smooth sharp interference peaks from a certain form factor. For example, 2D scattering patterns from a fibrin network under shear deformation were fitted with the form factor of an oriented cylinder [2]. To describe the hierarchical structure of branched wormlike micelle/chains [4], a hybrid model was introduced where the form factor of a cylinder described the local symmetry, and a unified power law [5] was used to account for the large scale structure. Moreover, the anisotropic structure of calcium-induced alginate gels was studied by the superposition of rod-like fibrils and Gaussian coils [6]. A drawback of this approach is that fitted sizes will have broad distributions due to inclusions of polydispersity, which renders it difficult to distinguish between samples prepared under similar conditions with subtle differences.

The second approach is to fit the sector intensity using a model without a specific geometry (referred to as a shape-independent model). The Ornstein-Zernike function was used to study the correlation length of uniaxially deformed polymer networks in the Tetra-PEG gel [7] and clay nanocomposite gels [8]; a sum of squared-Lorentz function and the scattering from randomly oriented thin rods were applied to study stretched slide-ring gels [9]; the radius of gyration of polystyrene fibres parallel and perpendicular to the rotation direction was extracted using an empirical model describing the scattering from polydispersed polymer chains [10]; and the Debye function was applied to study the radius of gyration of the Shish nuclei under extension flow [11]. With this approach, the interpretation of the physical meaning of fitted parameters will rely on an a priori assumption obtained from other techniques.

A third and simpler approach is to parametrise only changes in the peak position and the slope in the scattering pattern, without performing a global fit. This was used in the analysis of sector intensities from the 2D scattering pattern of a viscoelastic polymer-clay solution at different shear rates [12], as well as the crystallisation behaviour of poly(lactic-acid) polymers during annealing [13]. Such an approach displays the trend of samples with varying conditions but contains little information on an overall interpretation of the system.

To address above-mentioned situations, we introduce a new empirical anisotropic Guinier-Porod model to analyse the scattering from oriented objects. The model is derived from the Guinier-Porod model by Hammouda [14]. It is first used to approximate the sector intensity of oriented cylinders, and then applied to study sizes and degree of alignment of fibres in a protein gel made of calcium caseinate. After demonstrating that the model

can also approximate the sector intensity of oriented ellipsoids, we propose a generalised form of the anisotropic Guinier-Porod model.

4.2. Approximating the sector intensity of oriented cylinders

Detector plane: xy
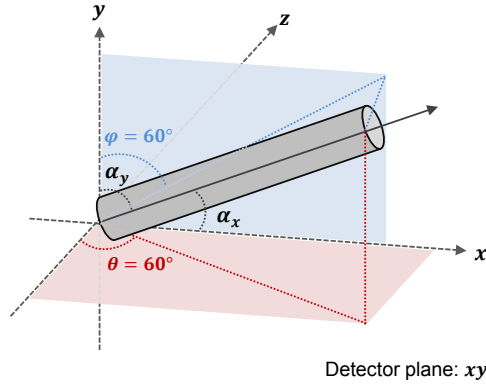
Figure 4.1: A schematic representation of the orientation of a cylinder in the Cartesian coordinate. From Eq. 4.6, one can calculate that when $\varphi = 60°$ and $\theta = 60°$, $\alpha_x = 39°$ and $\alpha_y = 63°$.

The original scattered intensity of oriented cylinders is given by [15, 16]:

$$I(\mathbf{Q}) = \phi(1 - \phi) \cdot V \cdot (\Delta\rho)^2 \cdot P_{\text{cylinder}}(\mathbf{Q}) \tag{4.1}$$

Where V and ϕ are the volume and volume fraction of a cylinder respectively, $\Delta\rho$ is the difference in scattering length density between the cylinder and the surrounding matrix. $P_{\text{cylinder}}(\mathbf{Q})$ is the form factor of an oriented cylinder given by:

$$P_{\text{cylinder}}(\mathbf{Q}) = P_{\text{cylinder}}(Q, \alpha) = \left[\frac{\sin(Q \cdot \cos\alpha \cdot \frac{L}{2})}{Q \cdot \cos\alpha \cdot \frac{L}{2}} \right]^2 \times \left[\frac{2J_1(Q \cdot \sin\alpha \cdot \frac{D}{2})}{Q \cdot \sin\alpha \cdot \frac{D}{2}} \right]^2 \tag{4.2}$$

Where L and D are the length and diameter of the cylinder respectively, α is the angle between the axis of the cylinder and the scattering vector $\mathbf{Q}$.
The anisotropic Guinier-Porod model (P_{aGP}) approximates the form factor of an oriented cylinder with the following equations:

$$P_{\text{cylinder}}(Q, \alpha) \approx P_{\text{aGP, cyl}}(Q, \alpha) = F_l(Q, \alpha) \cdot F_r(Q, \alpha) \tag{4.3}$$

Where

$$
F_l(Q, \alpha) = \begin{cases} e^{\frac{-(Q \cdot \cos\alpha \cdot L)^2}{12}} & Q \leq \frac{\sqrt{12}}{L \cdot \cos\alpha} \\[4mm] \left(\dfrac{\sqrt{12/e}}{Q \cdot \cos\alpha \cdot L} \right)^2 & Q \geq \frac{\sqrt{12}}{L \cdot \cos\alpha} \end{cases}
\tag{4.4}
$$

$$
F_r(Q, \alpha) = \begin{cases} e^{\frac{-(Q \cdot \sin\alpha \cdot D)^2}{12}} & Q \leq \frac{\sqrt{18}}{D \cdot \sin\alpha} \\[4mm] \left(\dfrac{\sqrt{18/e}}{Q \cdot \sin\alpha \cdot D} \right)^3 & Q \geq \frac{\sqrt{18}}{D \cdot \sin\alpha} \end{cases}
\tag{4.5}
$$

$F_l(Q, \alpha)$ approximates the Guinier and Porod regions of the scattering curve due to the length of the cylinder, while $F_r(Q, \alpha)$ approximates the Guinier and Porod regions of the scattering curve due to the cross section of the cylinder. A closer look reveals that $F_l(Q, \alpha)$ describes the scattering feature of $\left[\dfrac{\sin(Q \cdot \cos\alpha \cdot \frac{L}{2})}{Q \cdot \cos\alpha \cdot \frac{L}{2}} \right]^2$ and $F_r(Q, \alpha)$ describes the feature of $\left[\dfrac{2J_1(Q \cdot \sin\alpha \cdot \frac{D}{2})}{Q \cdot \sin\alpha \cdot \frac{D}{2}} \right]^2$ in Eq. 4.2. Inserting Eq. 4.3, 4.4 and 4.5 into Eq. 4.1 completes the model.
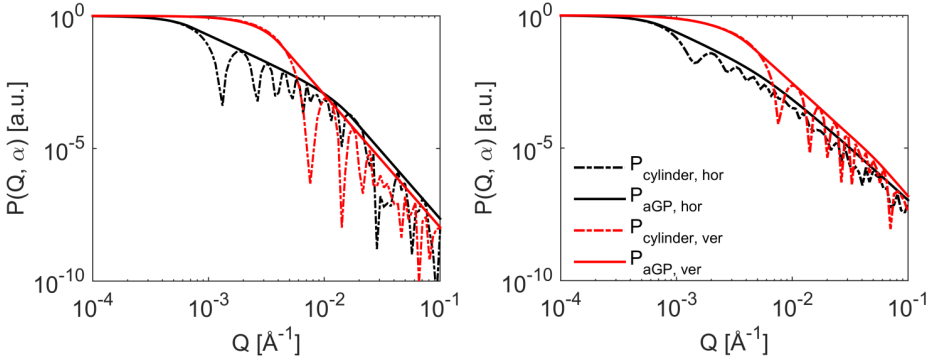

Figure 4.2: Comparison between the form factor of an oriented cylinder (dot dashed lines) and the corresponding anisotropic Guinier-Porod model (solid lines) at $\alpha_x = 14°$ (denoted as 'hor') and $\alpha_y = 80°$ (denoted as 'ver'). The diameter of the cylinder is 100 nm, and the length is 500 nm. Left: axes of cylinders are perfectly parallel to one another; Right: an orientation distribution of the axis with a standard deviation of 30° is included.

Before calculating the sector intensity, the reference orientation of the cylinder with respect to the detector [15] will be described. As is shown in Fig. 4.1, the angle between the incident beam (z-axis) and the projection of the cylinder axis onto the xz-plane is

defined as θ, while the angle between the y-axis and the projection of the cylinder axis onto the detector plane is defined as φ. The angles between the cylinder axis and the x-axis (α_x) as well as the y-axis (α_y) can be calculated given θ and φ:

$$\alpha_x = \arctan\sqrt{(\cot\theta)^2 + (\cot\varphi)^2}$$
$$\alpha_y = \arctan\left(\frac{\tan\varphi}{\sin\theta}\right)$$

(4.6)

Knowing α_x and α_y, the form factor in two perpendicular directions can be calculated as $P_{\text{aGP, cyl, hor}} = F_l(Q, \alpha_x) \cdot F_r(Q, \alpha_x)$ and $P_{\text{aGP, cyl, ver}} = F_l(Q, \alpha_y) \cdot F_r(Q, \alpha_y)$. The form factor of an oriented cylinder and the corresponding anisotropic Guinier-Porod model are presented in Fig. 4.2. It shows that the anisotropic Guinier-Porod model can capture very well the scattering feature of oriented cylinders at a given direction.

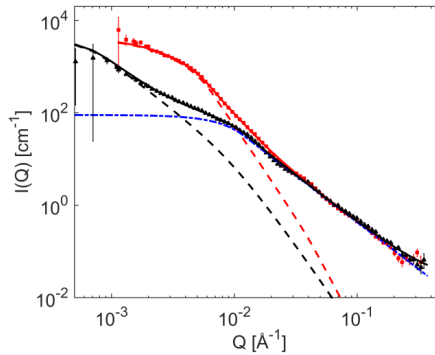## 4.3. APPLYING THE MODEL TO ORIENTED FIBRES IN A PROTEIN GEL

Figure 4.3: The horizontal (black triangles) and vertical (red squares) sector intensity of the fibrous calcium caseinate gel modelled by the sum of (solid lines) the anisotropic and isotropic Guinier-Porod model. Anisotropic contributions from cylinder-like fibres are presented by the red dashed line in the vertical direction and by the black dashed line in the horizontal direction. The isotropic scattering from spheres is presented by the blue dot dashed line.

Pronounced fibres are formed in a calcium caseinate gel after mild shearing and heating [17]. Microscopy images from previous works [17, 18] have shown that these fibres are composed of sphere-like particles aligned along the shear flow direction. As a result, a combined Guinier-Porod model, which is a sum of the anisotropic Guinier-Porod model describing the scattering from cylinder-like fibres at low Q and the isotropic Guinier-Porod model describing the scattering from sphere-like particles at high Q, is used to model the sector intensity. The scattering from spheres can be described by the original
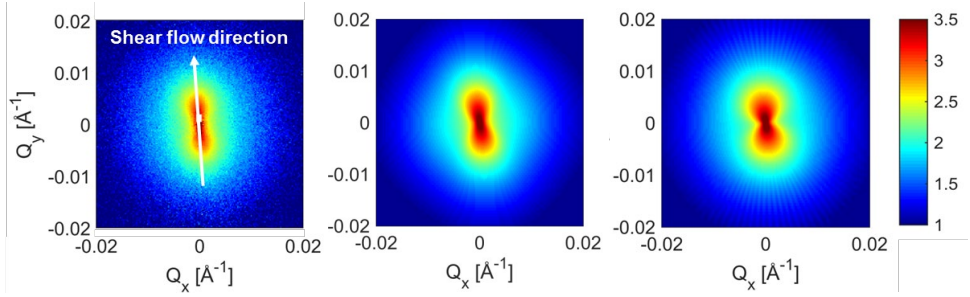
Figure 4.4: Measured and calculated 2D scattering patterns of the fibrous calcium caseinate gel. The intensity uses a logarithmic scale. Left: measured 2D pattern of the sample; Middle: calculated scattering pattern with a fibre diameter of 64 nm, a length of 437 nm, and a standard deviation of 20° on the orientation distribution; Right: calculated scattering pattern with a fibre diameter of 59 nm, a length of 824 nm, and a standard deviation of 30° on the orientation distribution. The sizes are obtained by simultaneously fitting two perpendicular sector intensities.

Guinier-Porod model:

$$
I_{\text{sphere}}(Q) =
\begin{cases}
G \cdot e^{\frac{-(Q \cdot R_g)^2}{3}} & Q \leq Q_1 \\[2ex]
\dfrac{D_s}{Q^d} & Q \geq Q_1
\end{cases}
\tag{4.7}
$$

The pre-factor G is written as $G = \phi_s(1-\phi_s) \cdot V_s \cdot (\Delta\rho_s)^2$, where V_s and ϕ_s are the volume and volume fraction of the sphere respectively, $\Delta\rho_s$ is the scattering length density contrast between the sphere and the surrounding matrix. R_g is the radius of gyration of the sphere, d is the Porod exponent that can have values between 0 and 4, depending on the roughness of the surface. $Q_1 = \dfrac{1}{R_g}\sqrt{\dfrac{3d}{2}}$ and $D_s = G \cdot e^{\frac{-(Q_1 \cdot R_g)^2}{3}} \cdot Q_1^d$.

The combined Guinier-Porod model shown in Fig. 4.3 fits very well to sector intensities of the sample, thus demonstrating its applicability to real systems. The fitted diameter of the fibre is 64±1 nm, the length is 437±79 nm, and the R_g of the sphere is 14.8±0.1 nm. These numbers are in accordance with reported values obtained from microscopy images [17].

Because fibres are not perfectly parallel, a Gaussian distribution with a standard deviation of 20° is applied to α_x and α_y during the fitting of sector intensities. It is observed that fitted sizes of the cylinder are dependent on the standard deviation of the orientation distribution: the larger the standard deviation, the higher the aspect ratio of the cylinder, while the quality of the fit remains similar. Yet, this does not mean the reliability of fitted parameters is low, since the standard deviation can be obtained through other means.

One straightforward way is to compare calculated 2D scattering patterns with the mea-
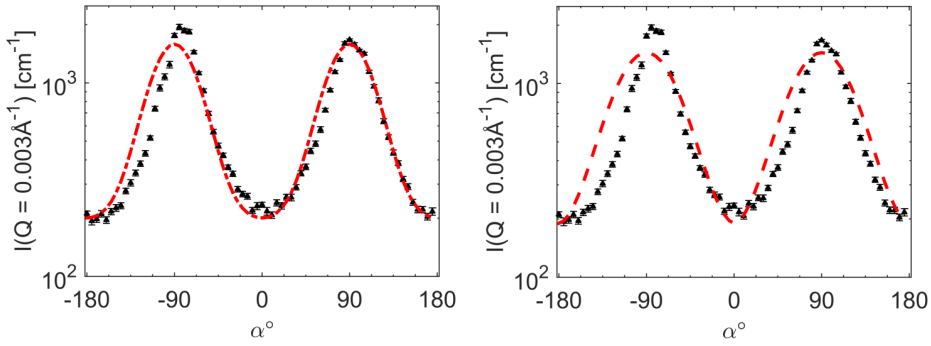
Figure 4.5: The annular intensity at Q = 0.003 Å, measured from the fibrous calcium caseinate gel (black triangles), and calculated from the anisotropic Guinier-Porod model. Left: a standard deviation of 20° on the orientation distribution is included (dot dashed line); Right: a standard deviation of 30° on the orientation distribution is included (dashed line).

sured one, as shown in Fig. 4.4. When the standard deviation of the orientation distribution is too large (30°), the scattering pattern will be overly smeared in the direction parallel to the shear flow (Fig. 4.4, right). Another way that requires less computation is to compare the distribution of the annular intensity at a given Q. Fig. 4.5 shows that the calculated annular intensity deviates more significantly from the measured one when the standard deviation of the orientation distribution is too large (30°). By these two means, we can confirm that an orientation distribution with a standard deviation of 20° is a fair estimation on the extent of alignment of fibres.

4.4. DISCUSSION

It is common that the surface of an object is rough. In that case, the Porod exponent will deviate from the Porod exponent of the same object with a smooth surface. The anisotropic Guinier-Porod model can adapt to that by treating the Porod exponent as an additional fitting parameter. For cylinders, Eq. 4.4 and 4.5 can consequently be rewritten into the following forms:

$$
F_l(Q, \alpha) =
\begin{cases}
e^{-\frac{d_l}{2}\left(\frac{Q}{Q_l(\alpha)}\right)^2} & Q \leq Q_l(\alpha) \\[2em]
\left(\frac{Q_l(\alpha)}{Q \cdot \sqrt{e}}\right)^{d_l} & Q \geq Q_l(\alpha)
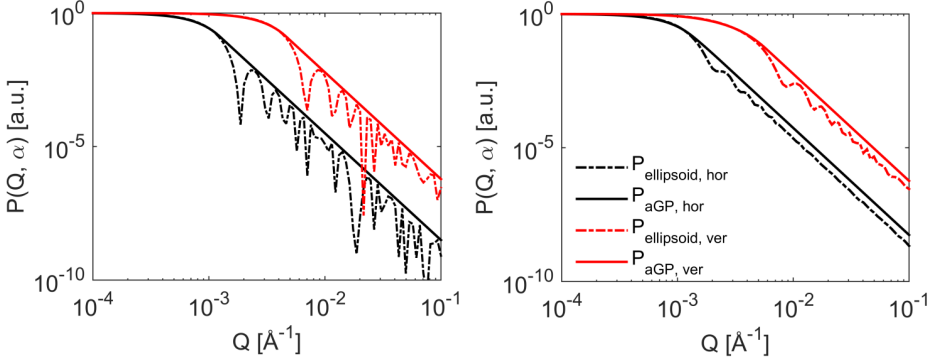\end{cases}
\tag{4.8}
$$

Figure 4.6: Comparison between the form factor of an oriented ellipsoid (dot dashed lines) and the corresponding anisotropic Guinier-Porod model (solid lines) at $\alpha_x = 14°$ (denoted as 'hor') and $\alpha_y = 80°$ (denoted as 'ver'). The equatorial radius of the ellipsoid is 50 nm, and the polar radius is 250 nm. Left: the polar axes of ellipsoids are perfectly parallel to one another; Right: an orientation distribution of the axis with a standard deviation of $30°$ is included.

$$F_r(Q, \alpha) = \begin{cases} e^{-\frac{d_r}{2}\left(\frac{Q}{Q_r(\alpha)}\right)^2} & Q \leq Q_r(\alpha) \\[2em] \left(\dfrac{Q_r(\alpha)}{Q \cdot \sqrt{e}}\right)^{d_r} & Q \geq Q_r(\alpha) \end{cases} \tag{4.9}$$

where $Q_l(\alpha) = \dfrac{\sqrt{6d_l}}{L \cdot \cos\alpha}$ and $Q_r(\alpha) = \dfrac{\sqrt{6d_r}}{D \cdot \sin\alpha}$, L and D are the length and diameter of the cylinder respectively, d_l and d_r are Porod exponents.

The anisotropic Guinier-Porod model can approximate not only the form factor of a cylinder, but also that of other oriented object, such as an ellipsoid shown as follows:

$$P_{\text{ellipsoid}}(Q, \alpha) \approx P_{\text{aGP, ellip}}(Q, \alpha) = F_e(Q, \alpha)^2 \tag{4.10}$$

with

$$F_e(Q, \alpha) = \begin{cases} e^{-\frac{d_e}{2}\left(\frac{Q}{Q_e(\alpha)}\right)^2} & Q \leq Q_e(\alpha) \\[2em] \left(\dfrac{Q_e(\alpha)}{Q \cdot \sqrt{e}}\right)^{d_e} & Q \geq Q_e(\alpha) \end{cases} \tag{4.11}$$

where $Q_e(\alpha) = 3/R_e(\alpha)$, $R_e(\alpha) = \sqrt{(r_e \cdot \sin\alpha)^2 + (r_p \cdot \cos\alpha)^2}$. r_e is the equatorial radius and r_p is the polar radius. The Porod exponent d_e is equal to 2 for a smooth surface.

The horizontal and vertical sector intensity of oriented ellipsoids and their corresponding anisotropic Guinier-Porod model are presented in Fig. 4.6. It is interesting to note
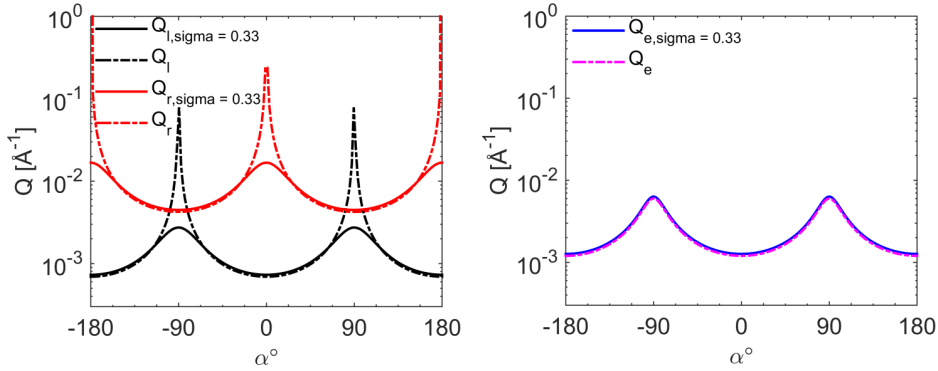
Figure 4.7: Transition points Q_l, Q_r and Q_e as a function of the angle α. Left: the Q_l and Q_r from a cylinder without (dot dashed lines) or with (solid lines), a standard deviation of 30° on the orientation distribution. Right: the Q_e from an ellipsoid without (dot dashed line) or with (solid line) a standard deviation of 30° on the orientation distribution. The diameter of the cylinder is 100 nm and the length is 500 nm; the equatorial radius of the ellipsoid is 50 nm and the polar radius is 250 nm.

that unlike the case of cylinders shown in Fig. 4.2, orientation distribution of the polar axis of the ellipsoid has little impact on the shape of the scattering curve, as well as on the intensity difference between two perpendicular sectors. This is related to the trend of transition points (i.e. Q_l, Q_r and Q_e) influenced by the orientation distribution, as depicted in Fig. 4.7. In the case of cylinders, the sector intensity in a certain direction α is the product of Eq. 4.8 and 4.9, which means both Q_l and Q_r play a role in the shape of the scattering curve. When orientation distribution is included, features in the convoluted Q_l and Q_r (Fig. 4.7 left) become less sharp. As a result, the two transition points are less discernible, and the resulting scattering curve becomes smoother. While for ellipsoids, the transition point is determined only by the 'surface to centre distance', R_e, which barely changes even when the orientation distribution of the polar axis is very broad (Fig. 4.7 right), thus, its sector intensity is less influenced by the orientation distribution.

Even though the difference in sector intensities between oriented cylinders and ellipsoids is significant, their radially averaged intensities are very similar, as shown in Fig. 4.8. The width of the form factor of the ellipsoid is broader than that of the cylinder, because the radius of gyration of the cylinder ($R_{g,\text{cylinder}} = D^2/8 + L^2/12$) is larger than that of the ellipsoid ($R_{g,\text{ellipsoid}} = 2r_e^2/5 + r_p^2/5$), given the two objects have the same outer dimensions.

Comparing Eq. 4.8, 4.9 and 4.11 suggests that a generalised anisotropic Guinier-Porod
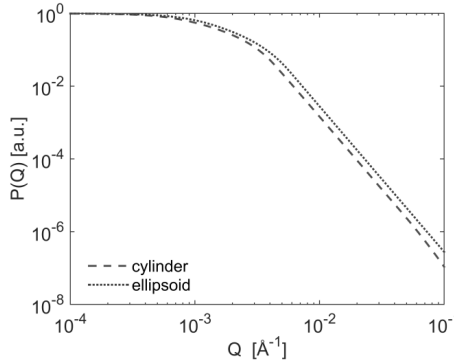
Figure 4.8: Comparison of radially averaged intensities between the cylinder (dashed line) and the ellipsoid (dotted line). The diameter of the cylinder is 100 nm and the length is 500 nm; the equatorial radius of the ellipsoid is 50 nm and the polar radius is 250 nm.

model has the following form:

$$
F_{\text{aGP}}(Q, \alpha) =
\begin{cases}
e^{-\frac{d}{2}\left(\frac{Q}{Q_0(\alpha)}\right)^2} & Q \leq Q_0(\alpha) \\[2ex]
\left(\dfrac{Q_0(\alpha)}{Q \cdot \sqrt{e}}\right)^d & Q \geq Q_0(\alpha),
\end{cases}
\tag{4.12}
$$

in which the choice of a function to describe $Q_0(\alpha)$ is important. This generalised form will offer the flexibility to describe the sector intensity of a variety of objects. Reversely, knowing the geometry of the object can help to fix fitting parameters such as the Porod exponent, which reduces numbers of fitting parameters and adds more certainty to fitted sizes. For example, the generalised anisotropic Guinier-Porod model in the case of ellipsoids is more suitable to describe oil droplets under shear or compression, while the cylindrical geometry will be more suitable when it comes to the characterisation of tubes or cylindrical micelles.

4.5. CONCLUSION

The empirical anisotropic Guinier-Porod model can be particularly useful in analysing the sector intensity of oriented objects. A detailed example is given using the model to fit two perpendicular sector intensities of oriented fibres in a calcium caseinate gel. By comparing calculated 2D patterns and annular intensities to measured ones, information on the standard deviation of the orientation distribution of fibres can be obtained as well. The anisotropic Guinier-Porod model is further extended to approximate the scattering from oriented ellipsoids. A generalised form of the anisotropic Guinier-Porod model is proposed which offers more flexibility to the description of a variety of objects. Compared to conventional shape-dependent models, the anisotropic Guinier-Porod model does not require a high polydispersity index to smear out sharp interfer-

ence peaks from the form factor. Compared to shape-independent models, the interpretation of the physical meaning of parameters does not require a priori information.

ACKNOWLEDGMENT

4

REFERENCES

[1] B. J. Maranzano and N. J. Wagner, *Flow-small angle neutron scattering measurements of colloidal dispersion microstructure evolution through the shear thickening transition,* The Journal of chemical physics **117**, 10291 (2002).

[2] K. M. Weigandt, L. Porcar, and D. C. Pozzo, *In situ neutron scattering study of structural transitions in fibrin networks under shear deformation,* Soft Matter **7**, 9992 (2011).

[3] F. Gazeau, E. Dubois, J.-C. Bacri, F. Boué, A. Cebers, and R. Perzynski, *Anisotropy of the structure factor of magnetic fluids under a field probed by small-angle neutron scattering,* Physical Review E **65**, 031403 (2002).

[4] K. Vogtt, G. Beaucage, M. Weaver, and H. Jiang, *Scattering function for branched wormlike chains,* Langmuir **31**, 8228 (2015).

[5] G. Beaucage, *Approximations leading to a unified exponential/power-law approach to small-angle scattering,* Journal of Applied Crystallography **28**, 717 (1995).

[6] Y. Maki, K. Ito, N. Hosoya, C. Yoneyama, K. Furusawa, T. Yamamoto, T. Dobashi, Y. Sugimoto, and K. Wakabayashi, *Anisotropic structure of calcium-induced alginate gels by optical and small-angle x-ray scattering measurements,* Biomacromolecules **12**, 2145 (2011).

[7] T. Matsunaga, H. Asai, Y. Akagi, T. Sakai, U.-i. Chung, and M. Shibayama, *Sans studies on tetra-peg gel under uniaxial deformation,* Macromolecules **44**, 1203 (2011).

[8] S. Miyazaki, T. Karino, H. Endo, K. Haraguchi, and M. Shibayama, *Clay concentration dependence of microstructure in deformed poly (n-isopropylacrylamide)- clay nanocomposite gels,* Macromolecules **39**, 8112 (2006).

[9] T. Karino, Y. Okumura, C. Zhao, T. Kataoka, K. Ito, and M. Shibayama, *Sans studies on deformation mechanism of slide-ring gel,* Macromolecules **38**, 6161 (2005).

[10] S. D. Mohan, G. R. Mitchell, and F. J. Davis, *Chain extension in electrospun polystyrene fibres: a sans study,* Soft Matter **7**, 4397 (2011).

[11] H. Yang, D. Liu, J. Ju, J. Li, Z. Wang, G. Yan, Y. Ji, W. Zhang, G. Sun, and L. Li, *Chain deformation on the formation of shish nuclei under extension flow: an in situ sans and saxs study,* Macromolecules **49**, 9080 (2016).

[12] G. Schmidt, A. I. Nakatani, P. D. Butler, and C. C. Han, *Small-angle neutron scattering from viscoelastic polymer- clay solutions,* Macromolecules **35**, 4725 (2002).

[13] A. Mahendrasingam, D. Blundell, M. Parton, A. Wright, J. Rasburn, T. Narayanan, and W. Fuller, *Time resolved study of oriented crystallisation of poly (lactic acid) during rapid tensile deformation,* Polymer **46**, 6009 (2005).

[14] B. Hammouda, *A new guinier–porod model,* Journal of Applied Crystallography **43**, 716 (2010).

[15] G. Fournet, *Étude théorique et expérimentale de la diffusion des rayons x par les ensembles denses de particules,* Bulletin de Minéralogie **74**, 37 (1951).

[16] A. Guinier, G. Fournet, and C. Walker, *Small-angle scattering of X-rays* (John Wiley & Sons, New-York, 1955).

[17] J. M. Manski, A. J. van der Goot, and R. M. Boom, *Formation of fibrous materials from dense calcium caseinate dispersions,* Biomacromolecules **8**, 1271 (2007).

[18] Z. Wang, B. Tian, R. Boom, and A. J. van der Goot, *Air bubbles in calcium caseinate fibrous material enhances anisotropy,* Food hydrocolloids **87**, 497 (2019).

[19] M. Doucet, J. Cho, G. Alina, J. Bakker, W. Bouwman, P. Butler, and e. a. Washington, A, *Sasview version 4.2.0,* http://doi.org/10.5281/zenodo.1412041 (2017).

4

5

SMALL ANGLE NEUTRON SCATTERING QUANTIFIES THE HIERARCHICAL STRUCTURE IN FIBROUS CALCIUM CASEINATE

Pronounced fibres are formed through simple shearing of a dense calcium caseinate dispersion. Both mechanical tests and scanning electron microscopy images demonstrate that the material is anisotropic. It is hypothesized that calcium caseinate aggregates, under shear, align into micro-fibres and bundle further into a hierarchical structure. Yet no direct evidence at the sub-micron length scale can support the assumption. Small angle neutron scattering (SANS) experiments were conducted on calcium caseinate samples prepared at different conditions. Analysis of the SANS data revealed that the micro-fibres have a diameter of ~100 nm and a length of ~300 nm. The addition of enzyme and air contributed to longer and thinner micro-fibres. Furthermore, the extent of fibre alignment at the micro-scale and the macroscopic anisotropy index followed the same trends with varying processing conditions. It is concluded that the material does indeed possess a hierarchical structure and the micro-fibres are responsible for the anisotropy on the macro-scale.

5.1. INTRODUCTION

A dietary transition towards more plant-based products can provide a long term solution to mitigate the impact of humans on the environment [1]. However, this transition is severely hampered by the fact that the majority of consumers prefer animal-derived products to plant-based alternatives. Recent consumer research has shown that plant-based alternatives that effectively replicate meat structure could potentially stimulate the transition away from the consumption of meat [2–4], thus emphasizing the importance of fibrous structures in meat analogues.

Over the years, a variety of meat analogues have been developed using different ingredients and through different technologies [5–11]. One prominent candidate is calcium caseinate [12]. It is obtained by re-dissolving the acid casein curd in a $Ca(OH)_2$ solution [13], then subjected to drying. The chemical composition and structure of calcium caseinate is similar to that of casein micelles, except that the four sub-caseins, α_{s1}-, α_{s2}-, β- and κ-casein, are connected by the Ca^{2+} ions, instead of the colloidal calcium phosphate (CCP) nanoclusters, since they are soluble at pH ~4.6 while casein micelles are not [14]. Comparable to the micellar structure in casein micelles, it is assumed that a caseinate aggregate is composed of sub-aggregates. Under simple shear and mild heat, a 30%w/w calcium caseinate dispersion can be transformed into pronounced fibrous structure. Scanning electron microscopy (SEM) images have shown that caseinate aggregates, with a typical diameter of a few hundreds of nanometres, are aligned into fibres which are parallel to the shear flow direction [15]. Given these fibres are also visible to the eye, it is hypothesized that the fibrous calcium caseinate has a hierarchical structure which prevails from mili- down into the nanometre length scale.

Based on this hypothesis, research has been conducted to study the anisotropy of fibrous calcium caseinate [16, 17]. The current understanding is that air bubbles are present in the protein dispersion during pre-mixing and that they enhance the anisotropy of the final material [18]. The addition of a crosslinking enzyme, transglutaminase, also appears to improve the anisotropy, as does maltodextrin [19]. In the above studies, the occurrence and quantification of anisotropy have always been examined by mechanical tests. The anisotropy index is calculated as the ratio between the true stress (or fracture strain) of the material being fractured parallel or perpendicular to the shear flow direction. As informative as the mechanical test can be, it is a bulk measurement that reflects the property of the material on the macroscopic scale; thus, a direct method that can prove and quantify the anisotropy and structure of the fibres at the microscopic scale is desirable.

The small angle neutron scattering (SANS) technique is proposed to serve this role in the study the structure of the fibres. It has been successfully applied to study the anisotropy and structure of many materials at the microscopic scale, such as the shear-induced orientation of polymer clay platelets [20], the chain conformation of model inter-penetrated elastomer networks [21], the orientation of collagen in human dentine [22], the hierarchical structure of bacterial cellulose [23] and the structural transitions in fibrin networks under shear deformation [24]. The application of SANS on food materials has also

grown in recent years [25, 26]. It has contributed to a better understanding of the hierarchical structure of plant cell walls [27] and to the characterisation of starch structure [28]. Similar to these studies, we expect a connection between the dimensions and anisotropy of the fibres obtained from SANS and the bulk mechanical properties.

In this work, SANS experiments were carried out on calcium caseinate samples following production at different shearing rates and times, both with or without the inclusion of enzyme and air. An analysis of the annular intensity was performed to quantify the extent of fibre alignment at the micro-scale; a anisotropic Guinier-Porod model was applied to fit two perpendicular sector intensities so as to extract the structural information of the micro-fibres. The SANS results were then compared to those obtained from mechanical tests.

5.2. Experimental section

5.2.1. Preparation of the fibrous materials

Materials

Spray-dried calcium caseinate powder was kindly provided by DMV International (Veghel, the Netherlands). According to the manufacturer's specification, it contains 91.5%w/w protein, ~5.2%w/w moisture and 3.9%w/w ash, among which 1.5%w/w is calcium. In practice, the measured dry matter is 94.8%w/w.

The activity of the microbial Ca^{2+}-independent transglutaminase derived from the Streptoverticillium moberansae (1%w/w transglutaminase, 99%w/w maltodextrin; Ajinomoto Co. Inc., Tokyo, Japan) is 114 units·g^{-1}, determined by the hydroxamate method [29]. A 20%w/w (in demineralized water) enzyme solution is stirred at room temperature for 1 h.

Preparation of the protein dispersions

Samples without enzyme or air were prepared from de-aerated protein dispersions before being loaded into a shear cell device [30]. A protein dispersion is obtained through manually mixing 30 g of calcium caseinate powder with 70 g of demineralized water using a spatula. The dispersion was then heated at 80 °C for 5 min and centrifuged at 2500×g for 2 min to remove most of the air. It was left at room temperature for 55 min before being transferred to the shear cell device. Samples with enzyme and air were prepared by manually mixing 30 g of protein powder with 62.5 g of water and 7.5 g of enzyme solution for 1 min.

Structure formation in the shear cell device

Well-defined shear flow was applied to the protein dispersion using a custom built shearing device (Wageningen University, the Netherlands). It consists of a rotating cone (the bottom cone, angle = 105°) and a stationary cone (the top cone, angle =100°). More details are described in earlier publications [30, 31]. Both cones were thermostatted with a circulating water bath.

The protein dispersions were transferred to the pre-heated (50 °C) shear cell device after mixing. The dispersions without enzyme or air were then subjected to shear at various rates (40, 50, 75, 100, 125 and 150 rpm) for 5 min. The dispersions with enzyme and air were subjected to either various shear rates (10, 25, 75, or 150 rpm) for 5 min, or to various shear times (1, 2.5, 15 or 30 min) at 50 rpm. After processing, the materials were cooled for 10 min at 4 °C. Tensile tests were performed within 1 h after removal of the material from the shear cell device. Parts of the materials were stored at -20 °C prior to the SANS measurements.

The material sheared for 30 min showed phase separation [16]. The area that was close to the tip of the shear cell was a uniform, yellowish gel, whereas the area close to the edge remained fibrous. Only the fibrous part was measured by the tensile test while both the fibrous and gel parts were measured by SANS. The resultant sector intensities of the fibrous part were fitted with a anisotropic Guinier-Porod model, while the isotropic scattering from the gel part was compared to a sample without shear.

5.2.2. Tensile strength analysis

To study the mechanical property of the fibrous material, a texture analyser (Instron Testing System, table model 5564) was used with a load cell of 100 N. A dog bone shaped mould was used to cut the material. A detailed preparation procedure can be found elsewhere [19]. The sample was 15.2 mm long and 3.18 mm wide, its thickness varied from 4 to 6 mm. The material was cut both parallel and perpendicular to the shear flow direction (based on the shear-vorticity plane). Tensile tests were conducted at a constant deformation speed of 3 mm/s. Grips with abrasive paper were used to prevent slippage during the test. At least three specimens per direction were measured. The results were depicted as force-displacement curves. The true stress (σ, kPa) and the Hencky strain (ε, -) were calculated as $\sigma = F(t)/A(t)$ and $\varepsilon = ln(L(t)/L_0)$, where $F(t)$ is the force, $A(t)$ is the cross sectional area, $L(t)$ is the length of the sample at time t, and L_0 is the initial length of the tensile bar (15.2 mm).

The Young's modulus ($E = \sigma/\varepsilon$, kPa) was calculated by applying a linear fit to the initial displacement. A Hencky strain interval between 0.03-0.27 was taken. The macroscopic anisotropy index was calculated as $E_\parallel/E_\perp$, where $E_\parallel$ is the Young's modulus of the sample fractured in the direction parallel to the shear flow, and $E_\perp$ is perpendicular to the shear flow.

5.2.3. Small angle neutron scattering (SANS)

SANS experiments of materials processed through the shear cell device were performed at the OPAL reactor, Australian Nuclear Science and Technology Organisation (ANSTO). Fig. 5.1 illustrates how a sample was cut from the material and mounted for the neutron measurement. Samples without enzyme or air were measured on the pinhole QUOKKA instrument [32, 33]. Four configurations were used to cover a Q range of 0.0006 to 0.64 Å^{-1}, where Q is the magnitude of the scattering vector defined as $Q = (4\pi/\lambda)\sin\theta$, λ is the wavelength in Å and 2θ is the scattering angle. The four configurations were: (i) source-
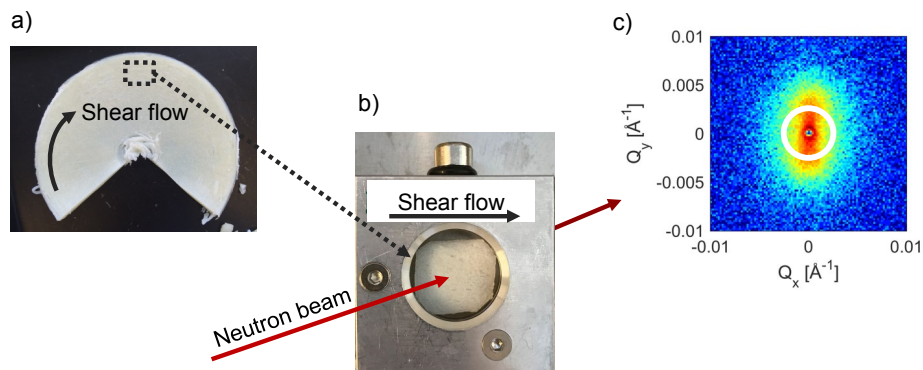
Figure 5.1: An illustration of the sample preparation for the SANS measurements. a) a rectangular sample ($L \times H \times W \approx 1 \times 0.7 \times 0.2$ cm) was cut from a fibrous gel slab, with its length being parallel to the shear flow direction. b) this sample was placed in a sample holder and presented to the neutron in transmission geometry. c) a typical 2D scattering pattern obtained using the focusing configuration on the QUOKKA instrument.

5

to-sample distance (SSD) = 20.2 m with focusing optics using MgF_2 lenses; (ii) SSD = 20.2 m, sample-to-detector distance (SDD) = 20.1 m; (iii) SSD = 8.0 m, SDD = 8.0 m and (iv) SSD = 12 m, SDD = 1.3 m, with 10% wavelength resolution and λ = 8.1 Å for (i) and λ = 5.0 Å for (ii)-(iv). Source and sample apertures of 50 mm and 12.5 mm were used respectively. Sample temperature was controlled by a Huber thermostatted bath and held at 25 °C throughout the measurements. All data were corrected for blocked beam measurements, normalized, radially averaged and placed on an absolute scale, following attenuated direct beam measurements, using a package of macros in the Igor Pro software (Wavemetrics, Lake Oswego, OR, U.S.A.) modified to accept HDF5 data files from QUOKKA. Fig. 5.2 gives an example on how sector cut intensities, obtained at different SDD, were combined into 1D sector intensities. To correct for the incoherent scattering from the solvent, 70% of the scattering intensity of the H_2O was subtracted from each sample.

Samples with enzyme and air were measured on the BILBY instrument [34]. A wavelength range of 2-20 Å yielded a Q range of 0.001 to 0.35 Å^{-1}, which is similar to QUOKKA. The BILBY data were reduced using the Mantid framework [35]. A different background subtraction approach was taken to correct for the incoherent scattering. The slope of the scattering curve at high Q was fitted with the sum of a constant and a power law, the percentage of the H_2O subtracted from the sample was determined by the value of the fitted constant.

One reference sample–the protein dispersion without shear–was measured on the LAR-MOR instrument at ISIS, UK. The time-of-flight instrument utilised wavelength of 0.9 to 13 Å, which gave a Q range of 0.003-0.4 Å^{-1}. To account for the incoherent background,

70% of the scattering intensity of the H_2O was subtracted. Data reduction was performed using the Mantid framework [35].

The vertical sector intensity was obtained by averaging over $\pm 10°$ along the direction where the intensity is the highest. The horizontal sector intensity was obtained by averaging the intensity over $\pm 10°$ in the direction perpendicular to the highest intensity. The vertical and horizontal sector intensities were fitted simultaneously using an anisotropic Guinier-Porod model (Eq. 5.2 and 5.3). This was achieved by embedding the model as a plugin function into the simultaneous fit functionality of SASView 4.2.0 [36].
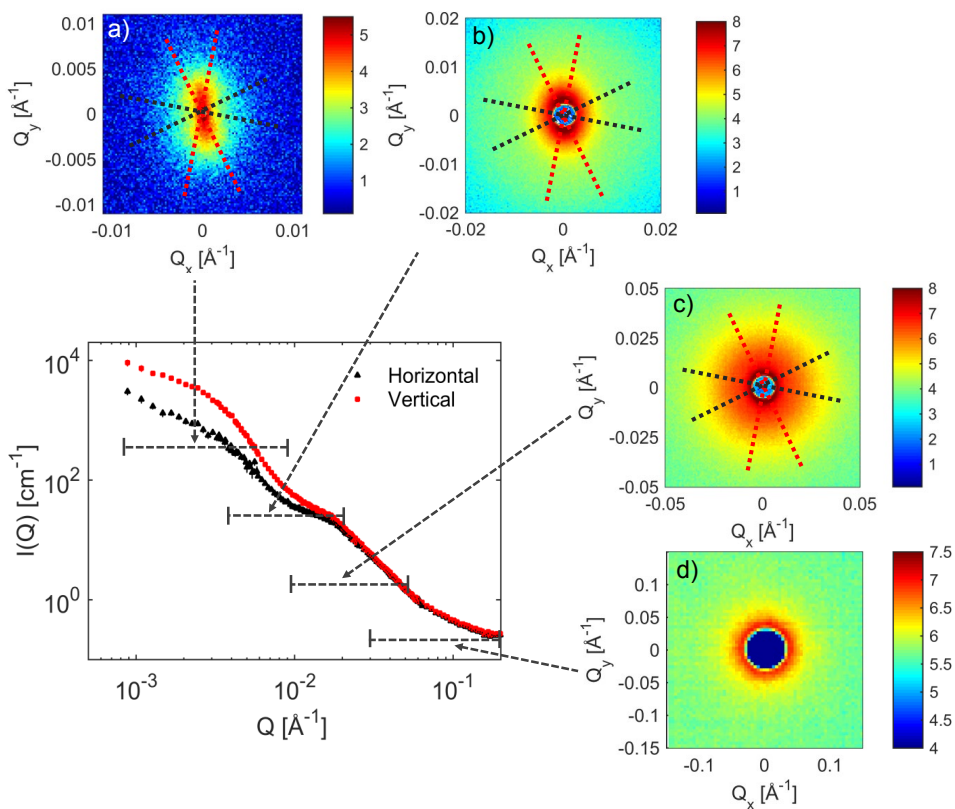
Figure 5.2: A complete set of the reduced and normalized sector intensities of a sample (without enzyme or air, sheared at 75 rpm for 5 min) measured on the QUOKKA instrument. Data were obtained by combining four instrument configurations that each covers a Q range (indicated by dashed lines). Figs. a)-d) are 2D scattering patterns from the corresponding lens with detector at 20 m, conventional 20 m, 8 m and 1.3 m detector positions. The 2D patterns are presented as measured.

5.3. RESULTS AND DISCUSSION

5.3.1. SIZE AND STRUCTURE OF THE CALCIUM CASEINATE GEL

SIZE AND STRUCTURE OF THE CASEINATE PARTICLE IN THE UNSHEARED PROTEIN DISPERSION

The two perpendicular sector intensities for the unsheared protein dispersion shown in Fig. 5.3a overlap, confirming that the material is isotropic. The scattering intensity continues to increase in the limit of low Q of the instrument, suggesting the presence of larger aggregates or clusters in the gel. Large aggregates are indeed observed in the SEM image presented in Fig. 5.4a.
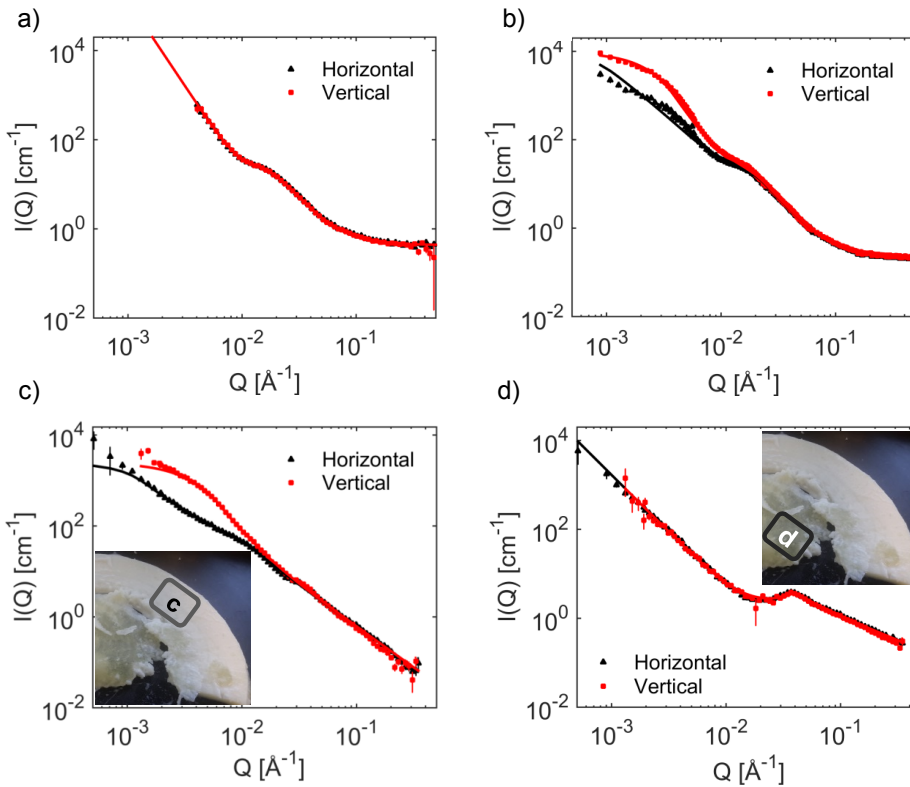

Figure 5.3: Examples of typical sector scattering from different samples. a) an unsheared protein dispersion; b) a fibrous sample sheared at 75 rpm for 5 min, without enzyme or air; c) the fibrous part (inset) of a sample sheared at 50 rpm for 30 min, with addition of enzyme and air; d) the gel part (inset) of the same sample as c). Lines in a) and d) represent fits using a broad peak model, lines in b) and c) are fits of the sector intensities using a combined Guinier-Porod model.

An empirical 'broad peak' model [36] is applied to fit the isotropic scattering data. The choice of the 'broad peak' model over the more commonly used 'correlation length' model [37] is because that it can also describe the feature of a sharper peak (e.g. the gel

part of the phase separated sample in Fig. 5.3d), so that fitted parameters from different samples are consistent and comparable. The 'broad peak' model is given by

$$I(Q) = \frac{A}{Q^d} + \frac{C}{1 + (|Q - Q_0|\xi)^m} + \text{Background}, \tag{5.1}$$

where A and d is the Porod scale factor and the exponent respectively; C and m is the Lorentzian scale factor and the exponent respectively; ξ is the Lorentzian screening length, which can be interpreted as the gel mesh size in case of a gel network [38]. The peak position Q_0 is related to the d-spacing as $d = 2\pi/Q_0$, which corresponds to the average center-to-center distance between neighbouring particles [39].

Table 5.1: Fitted parameters of the isotropic protein gel using the model from Eq. 5.1.

	A	d	C	m	Q_0 [Å^{-1}]	ξ [nm]
1[a]	$(4.0 \pm 2.4) \times 10^{-7}$	3.8 ± 0.1	19.3 ± 0.8	2.0 ± 0.1	0.013 ± 0.001	9.8 ± 0.3
2[b]	$(3.4 \pm 0.3) \times 10^{-5}$	2.6 ± 0.1	3.7 ± 0.1	1.0 ± 0.1	0.040 ± 0.001	3.7 ± 0.1

[a]: protein dispersion without shear (Fig. 5.3a)
[b]: sheared for 30 min (gel part in Fig. 5.3d)

Fitted parameters of the sample without shear (Fig. 5.3a) are presented in the first row in Table 5.1. The mesh size of the gel is around 10 nm. In the case of caseinate, this may be interpreted as the size of a sub-aggregate, since it is close to the average value of the sub-structure in casein micelles [40–42]. This size is also similar to the radius of gyration (R_g) of the sphere-like particles in the fibrous samples without enzyme or air shown in Table 5.2, suggesting that the sub-aggregates are the elementary building block in caseinate. The d-spacing between the neighbouring sub-aggregate is approximately 48 nm, which is in agreement with the distance between two adjacent particles in Fig. 5.4a, at a closer look.

The 'broad peak' model is also applied to fit the gel part of the phase separated sample shown in Fig. 5.3d, the resultant fitted parameters are presented in the second row in Table 5.1. The gel mesh size is reduced to less than one half of that compared to the protein dispersion without shear, as is the d-spacing. This may be explained as the caseinate sub-aggregates becoming compacted over time. Expelled water is observed on the surface of the gel after 30 min of shearing, which supports this explanation. Because the compacted particles are denser than the fibres, the material phase separates into a dense isotropic gel that is close to the tip of the cone and a fibrous gel close to the edge.

SIZE AND STRUCTURE OF THE FIBRES IN ANISOTROPIC PROTEIN DISPERSIONS
The SEM image in Fig. 5.4b reveals that the sheared sample contains cylinder-like microfibres which are composed of sphere-like aggregates. Thus, it is reasonable to attribute the measured scattering intensity to the summation of the scattering from both cylinders and spheres, as depicted in Fig. 5.4c.
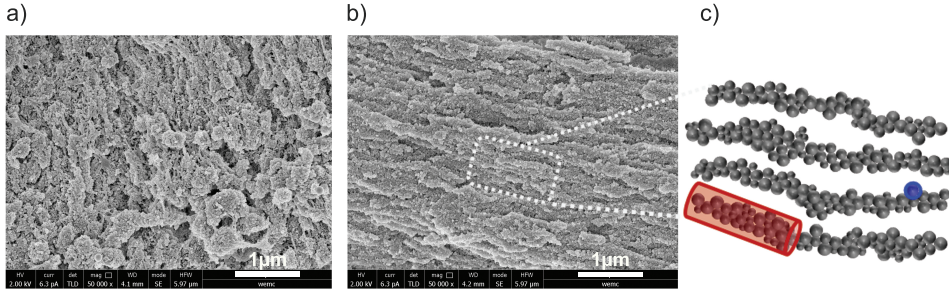
Figure 5.4: An illustration of the fibres based on SEM images. a) a SEM image of the protein dispersion without shear. Sub-aggregates with a diameter of ~10 nm form larger sphere-like aggregates with a size of a few hundreds of nanometres. b) Reproduction of a SEM image of a sheared sample (without enzyme or air, sheared at 50 rpm for 5 min) fractured parallel to the shear flow direction [18]. Copyright 2019, Elsvier. c) A schematic illustration of the micro-fibres: the system can be simplified into cylinders composed of sphere-like calcium caseinate aggregates.

The anisotropic scattering from the cylinders can be approximated by an anisotropic Guinier-Porod model, while the isotropic scattering from the spheres can be approximated by the original Guinier-Porod model [43]. The total scattering intensity is calculated as

$$I(Q, \alpha) = I_{\text{fibre}}(Q, \alpha) + I_{\text{sphere}}(Q) + \text{Background}$$
$$I_{\text{fibre}}(Q, \alpha) = \phi(1 - \phi) \cdot (\Delta\rho)^2 \cdot V \cdot F_l(Q, \alpha) \cdot F_r(Q, \alpha) \tag{5.2}$$
$$I_{\text{sphere}}(Q) = \phi_s(1 - \phi_s) \cdot (\Delta\rho_s)^2 \cdot V_s \cdot F_s(Q)$$

where

$$F_l(Q, \alpha) = \begin{cases} e^{\frac{-(Q \cdot \cos\alpha \cdot L)^2}{12}} & Q \leq \frac{\sqrt{12}}{L \cdot \cos\alpha} \\ (\frac{\sqrt{12/e}}{Q \cdot \cos\alpha \cdot L})^2 & Q \geq \frac{\sqrt{12}}{L \cdot \cos\alpha} \end{cases}$$

$$F_r(Q, \alpha) = \begin{cases} e^{\frac{-(Q \cdot \sin\alpha \cdot D)^2}{12}} & Q \leq \frac{\sqrt{18}}{D \cdot \sin\alpha} \\ (\frac{\sqrt{18/e}}{Q \cdot \sin\alpha \cdot D})^3 & Q \geq \frac{\sqrt{18}}{D \cdot \sin\alpha} \end{cases} \tag{5.3}$$

$$F_s(Q) = \begin{cases} e^{\frac{-(Q \cdot Rg)^2}{3}} & Q \leq Q_1 \\ \frac{D_s}{Q^d} & Q \geq Q_1 \end{cases}$$

In Eq. 5.2, ϕ is the volume fraction of the micro-fibres, $\Delta\rho$ is the difference in scattering length density (SLD) between the fibres and the surrounding matrix. The product of $\phi(1 - \phi) \cdot (\Delta\rho)^2$ is fitted as one parameter and denoted as 'P_f'. The volume of the micro-fibre is calculated as $V = \pi D^2 L/4$, where L is the length of the fibre and D is the diameter.

Similarly, ϕ_s is the volume fraction of the spheres, $\Delta\rho_s$ is the SLD contrast between the spheres and the surrounding matrix. The product of $\phi_s(1-\phi_s)\cdot(\Delta\rho_s)^2$ is denoted as 'P_s'. The volume of the sphere is $V_s = 4\pi R_g^3/3$, where R_g is the radius of gyration. In Eq. 5.3, d is the Porod exponent which describes the roughness of the surface; $Q_1 = \dfrac{1}{R_g}\sqrt{\dfrac{3d}{2}}$ and

$$D_s = e^{\frac{-(Q_1\cdot R_g)^2}{3}}\cdot Q_1^d.$$

The angle α specifies the scattering intensity in a certain direction. α_x and α_y are the angles between the cylinder axis and the x-axis or y-axis on the detector plane, respectively. During measurements the fibres are placed parallel to the x-axis, thus the horizontal intensity is obtained at $\alpha_x = 0°$ and the vertical intensity is obtained at $\alpha_y = 90°$. Since the fibres are not perfectly parallel to each other, a Gaussian distribution with a standard deviation of $20°$ is included for both α_x and α_y.

The two perpendicular sector intensities are fitted simultaneously using Eq. 5.2 and 5.3. Fig. 5.3b displays the sector intensities and the corresponding fits of a sample without enzyme or air, and Fig. 5.3c shows the data and fits of a sample with the addition of enzyme and air. The slight inconsistency between the fits and the data at low Q from the BILBY data may have risen from the multiple scattering from the sample. Dimensions of the micro-fibres at different shearing conditions are shown in Fig. 5.5; the rest of the fitted parameters are summarised in Table 5.2.
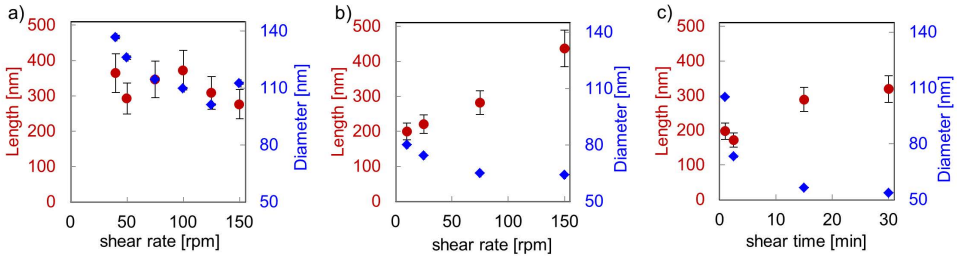

Figure 5.5: Fitted length (red circles) and diameter (blue diamonds) of the micro-fibres as a function of shear rate or time. (a) samples without enzyme or air, sheared at 40, 50, 75, 100, 125 and 150 rpm for 5 min. (b) samples with enzyme and air, sheared at 10, 25, 75 and 150 rpm for 5 min. (c) samples with enzyme and air, sheared at 50 rpm for 1, 2.5, 15 and 30 min. The error bar of the diameter is smaller than the size of the symbol.

As shear rate increases, the diameter of the fibre in samples without enzyme or air (Fig. 5.5a) first decreases from 137 ± 1 to 101 ± 1 nm and then increases to 113 ± 1 when the shear rate is higher than 125 rpm. The length of the fibre is ~320 nm and remains nearly constant. The highest aspect ratio ($=L/D$) is obtained in the sample sheared at 100 rpm. Samples with the addition of enzyme and air contain slightly longer and much thinner micro-fibres. Fig. 5.5b shows that the length increases from ~200 to ~450 nm while the diameter decreases from ~80 to ~65 nm with increasing shear rate. A longer shear time has a similar but more severe impact on the diameter. It is reduced to one half

after being sheared for more than 15 min, as shown in Fig. 5.5c. The increase in the length of the micro-fibre can be attributed to the crosslinking by tranglutaminase. Yet, what contributes more to the higher aspect ratio of the micro-fibres in Fig. 5.5b and c is the drastic reduction in the diameter. This is probably due to the incorporation of air. Elongated air bubbles compact the material, especially in the direction perpendicular to the shear flow, thus leading to the decrease in the diameter.

Table 5.2: A summary of the fitted parameters of the sector intensities using the model from Eq. 5.2 and 5.3.

no enzyme or air	R_g [nm]	P_f [10^{-12} Å^{-4}]	P_s [10^{-12} Å^{-4}]	d	bkgd [cm^{-1}]
40 rpm	8.3 ± 0.1	0.17 ± 0.01	0.40 ± 0.01	2.74 ± 0.01	0.31 ± 0.01
50 rpm	8.6 ± 0.1	0.16 ± 0.01	0.39 ± 0.01	2.72 ± 0.01	0.31 ± 0.01
75 rpm	8.2 ± 0.1	0.16 ± 0.01	0.39 ± 0.01	2.72 ± 0.01	0.22 ± 0.01
100 rpm	8.5 ± 0.1	0.18 ± 0.01	0.41 ± 0.01	2.70 ± 0.01	0.50 ± 0.01
125 rpm	8.4 ± 0.1	0.17 ± 0.01	0.38 ± 0.01	2.65 ± 0.01	0.23 ± 0.01
150 rpm	8.5 ± 0.1	0.16 ± 0.01	0.39 ± 0.01	2.69 ± 0.01	0.30 ± 0.01
with enzyme & air	R_g [nm]	P_f [10^{-12} Å^{-4}]	P_s [10^{-12} Å^{-4}]	d	bkgd [cm^{-1}]
10 rpm	15.2 ± 0.1	0.17 ± 0.01	0.28 ± 0.01	2.03 ± 0.01	0.39 ± 0.01
25 rpm	13.3 ± 0.1	0.15 ± 0.01	0.27 ± 0.01	1.96 ± 0.01	0.21 ± 0.01
75 rpm	13.1 ± 0.1	0.16 ± 0.01	0.26 ± 0.01	1.81 ± 0.01	0.01 ± 0.01
100 rpm	14.8 ± 0.1	0.17 ± 0.01	0.26 ± 0.01	2.03 ± 0.01	0.02 ± 0.01
with enzyme & air	R_g [nm]	P_f [10^{-12} Å^{-4}]	P_s [10^{-12} Å^{-4}]	d	bkgd [cm^{-1}]
1 min	11.6 ± 0.1	0.15 ± 0.01	0.29 ± 0.01	2.04 ± 0.01	0.24 ± 0.01
2.5 min	5.4 ± 0.1	0.09 ± 0.01	0.33 ± 0.01	1.79 ± 0.01	0.03 ± 0.01
15 min	11.9 ± 0.1	0.14 ± 0.01	0.21 ± 0.01	1.73 ± 0.01	0.12 ± 0.01
30 min (fibre-part)	7.6 ± 0.1	0.21 ± 0.01	0.27 ± 0.01	1.41 ± 0.01	0.06 ± 0.01

As mentioned before, the sphere-like aggregates in the micro-fibres are composed of elementary sub-aggregates. The R_g of these sub-aggregates is equal to ~8.5 nm in samples without enzyme or air (first column in Table 5.2). This size remains constant with increasing shear rate, indicating that shear merely aligns the larger aggregates and has no influence on the sub-structure of the caseinate. This has also been observed by Jaspe et al., [44] in a modelling study, which concludes that an extremely high shear rate (~10^7 s^{-1}) is required before shear takes effect in the shape or structure of the protein particle. On the other hand, the R_g in samples with enzyme and air nearly doubled. This implies that the enzyme not only extends the length of the fibre but also crosslinks the sub-aggregates which consequently contributes to stronger fibres.

The fitted P_f and P_s in Table 5.2 remain nearly constant within each sample set, indi-

cating that processing conditions have little to no influence on the SLD contrast and the volume fraction. Even so, it remains challenging to identify the exact cause of the SLD contrast, due to the complexity of the system. For instance, both the SLD contrast between the fibres and the air and the contrast between the fibres and the solvent contribute to the P_f. It is thus concluded that even though values of P_f and P_s are in agreement with the composition of the protein, the results remain phenomenological.

5.3.2. EXTENT OF FIBRE ALIGNMENT

The annular intensity obtained from the 2D pattern provides information on the extent of fibre alignment and the orientation of the fibres with respect to the shear flow direction. Fig. 5.3b and c shows that the intensity begins to diverge at $Q < 0.01 \text{ Å}^{-1}$. As a result, the annular intensity at $Q = 0.003 \text{ Å}^{-1}$ is plotted and fitted with the Legendre polynomial [24, 45]

$$I(Q = 0.003 \text{ Å}^{-1}, \psi) = \sum_{n=0}^{\infty} a_n \cdot P_{2n}(\cos\psi^*) \tag{5.4}$$

where a_n is the pre-factor of the polynomial, $\psi^* = \psi - (\psi_0 + \dfrac{\pi}{2})$, ψ_0 is the angle between the average direction of the fibres and the shear flow. It is also the direction at which the scattering intensity is the highest. Fig. 5.6 gives an example of the goodness of the fit.
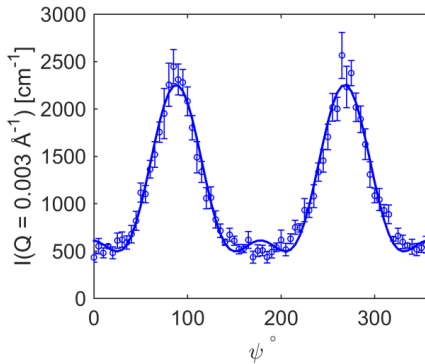

Figure 5.6: An example of the annular intensity fitted with the Legendre polynomial. A small bump at ∼180° is likely to be caused by the higher order Legendre polynomial.

The extent of alignment of the micro-fibres is related to the Hermans' orientation or nematic order parameter [46], and is calculated as $\dfrac{a_1}{5a_0}$. When $\dfrac{a_1}{5a_0} = 1$, the system has a perfect parallel orientation; when $\dfrac{a_1}{5a_0} = 0$, the system is totally randomly oriented, and $\dfrac{a_1}{5a_0} = -0.5$ when the system has a perfect perpendicular orientation [24, 45]. Given all the samples were mounted with the shear flow direction being parallel to the x-axis on the detector plane, $\dfrac{a_1}{5a_0}$ should have values between 0 and 1.
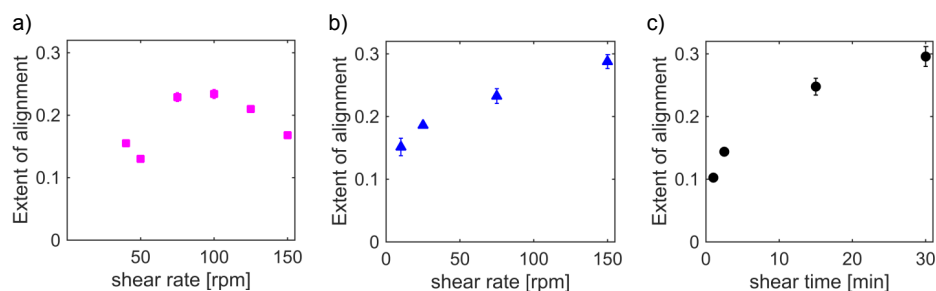
Figure 5.7: The extent of alignment of the microfibre as a function of shear rate or time. (a) samples without enzyme or air, sheared at 40, 50, 75, 100, 125 and 150 rpm for 5 min. (b) samples with enzyme and air, sheared at 10, 25, 75 and 150 rpm for 5 min. (c) samples with enzyme and air, sheared at 50 rpm for 1, 2.5, 15 and 30 min.

Fig. 5.7 summarises the extent of alignment from different samples. For samples without enzyme or air, the extent of alignment first increases with shear rate and then decreases. The most anisotropic fibre is produced between 75 and 100 rpm. The higher shear rate accompanied by the larger shear stress could break up the alignment of the micro-fibres [47], thus leading to the decrease in the extent of alignment. As for samples with enzyme and air, a continuous increase in the extent of alignment is observed when increasing either shear rate or time. Such a trend is also observed in the aspect ratio of the micro-fibres. Compared to samples without enzyme or air, the extent of alignment in samples with enzyme and air is greater at higher shear rate, and the micro-fibres have already shown alignment at shear rates lower than 40 rpm.

To summarise, through analysing the SANS data, we have gained insights into the sizes, structure and extent of alignment of the micro-fibres in calcium caseinate gels. Enzyme and air enhanced the orientation of the micro-fibres and facilitated systematic manipulation (e.g. varying shear rate or time) of the dimensions of the micro-fibres.

5.3.3. MECHANICAL PROPERTIES

Several parameters can describe the macroscopic anisotropy, such as the true stress, Hencky strain or Young's modulus. The true stress and Hencky strain are determined by the fracture point where a drastic decrease of the stress is observed in the stress-strain curve. These measurements can distinguish well the trend in the macroscopic anisotropy but are not comparable to the microscopic anisotropy derived from SANS. The reason is that the material is fractured irreversibly, while no deformation is applied to the sample during the SANS measurement.

Perhaps a more appropriate indication of the macroscopic anisotropy is the Young's modulus. It describes the stiffness of the material and is calculated using the near-zero linear region of the stress-strain curve. This method ensures the deformation is elastic,

reversible and kept to a minimum. It should also be noted that the anisotropy index obtained in this way is expected to be smaller than the reported anisotropy indices calculated from the true stress or Hencky strain [47], due to the fact that a smaller stress-strain region is employed.
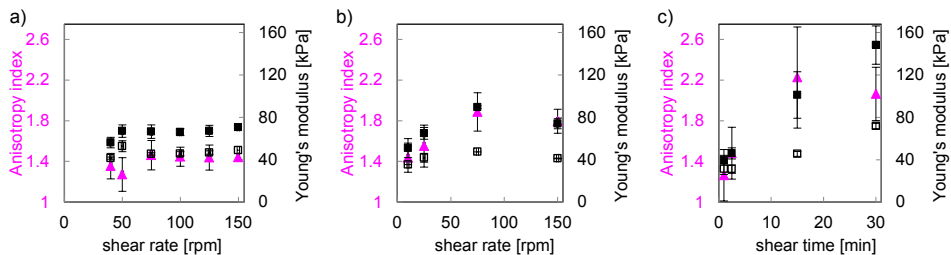

Figure 5.8: The anisotropy index (filled triangles) as a function of shear rate or time, the secondary axis is the Young's modulus of samples fractured along (filled squares) or perpendicular (hollow squares) to the shear flow direction. (a) samples without enzyme or air, sheared at 40, 50, 75, 100, 125 and 150 rpm for 5 min. (b) samples with enzyme and air, sheared at 10, 25, 75 and 150 rpm for 5 min. (c) samples with enzyme and air, sheared at 50 rpm for 1, 2.5, 15 and 30 min.

The macroscopic anisotropy index together with the Young's moduli of samples fractured in the direction parallel or perpendicular to the shear flow are presented in Fig. 5.8. For samples without enzyme or air, $E_\parallel$ and $E_\perp$ remain nearly constant with increasing shear rate, as is the resultant macroscopic anisotropy index. Samples with the addition of enzyme and air exhibit a more distinctive trend. As the shear rate increases, both $E_\parallel$ and $E_\perp$ increases in Fig. 5.8b. They reach the largest value at 75 rpm and start to decrease from 75 to 150 rpm, suggesting higher shear rate breaks the fibres. Increasing shear time leads to a continuous increase of Young's moduli. The resultant anisotropy index shown in Fig. 5.8c almost doubled between samples sheared for 1 and 15 min. Higher anisotropy indices in Fig. 5.8b and c thus confirm that air bubbles and enzymatic crosslinking are beneficial to the anisotropy at the macroscopic scale[17, 19].

It is interesting to note that $E_\perp$ is hardly affected by the shear rate, time or the addition of enzyme and air. It is $E_\parallel$ that is responsible for the increase of the anisotropy index. This seems to suggest that the calcium caseinate aggregates are crosslinked along a preferred direction guided by the shear flow. Such an effect is limited to shear times less than 15 min, since longer shear times could lead to phase separation.

5.3.4. DISCUSSION

A major interest of this work is to study the correlation between the extent of alignment in the fibres at the micro-scale and the mechanical property at the macro-scale. For this purpose, we employed SANS to extract information about the extent of alignment of the micro-fibres from the sub-micron level. For the macroscopic anisotropy, we conducted tensile tests and used the quotient of Young's moduli in two perpendicular directions as

an indication.

A comparison between Fig. 5.7 and Fig. 5.8 shows that the extent of alignment of the micro-fibres and the macroscopic anisotropy index follow the same trend with varying processing conditions. Moreover, the aspect ratio ($=L/D$) of the micro-fibres in Fig. 5.5 also follows the same trend. The results show that the material possesses a consistent trend in anisotropy at different length scales. These findings imply further that the dimensions of the micro-fibres are responsible for the mechanical property at the macro-scale.

Lastly, calcium caseinate is the only meat analogue candidate, to our knowledge, which displays anisotropy in Young's modulus. Chicken meat also displays anisotropy in Young's modulus [48], and it has a fibrous structure at the sub-micron length scale [49]. In this sense, anisotropy in Young's modulus could be a simple indication of protein alignment at the micro-scale. The only pitfall is that the trend calculated from the Young's moduli can be quite weak, even though the sample displays a clear anisotropy at the microscopic scale, such as the sample set without enzyme or air. This is likely to be caused by the inhomogeneity in the bulk structure, which renders greater uncertainties in the determination of the Young's modulus. Associated errors becomes even larger due to error propagation during calculations of the anisotropy index. It is also worth of mentioning that even though the inhomogeneity poses a challenge to the characterisation of the structure, it does not mean the structure is unsuitable from a food perspective. Indeed, food materials in nature are inherently inhomogeneous, and consumers can in fact prefer and appreciate such an inhomogeneity.

5.4. CONCLUSION

To understand the hierarchical structure of the fibres in calcium caseinate, we have conducted SANS measurements quantifying the sizes, structure and extent of alignment of the micro-fibres, and performed tensile tests to study the macroscopic anisotropy of materials processed at different conditions.

Prior to shearing, the protein dispersion is an isotropic gel network loosely formed by sphere-like aggregates. They are composed of sub-aggregates with a mesh size of ~10 nm. Upon shearing, the sphere-like aggregates are aligned and form cylinder-like micro-fibres with a diameter of ~100 nm and a length of ~300 nm. The addition of maltodextrin enriched-enzyme and air extends the length of the fibre and decreases its diameter. Transglutaminase probably crosslinks the sub-aggregates and contributes to stronger fibres.

The aspect ratio and the extent of alignment of the micro-fibres follow the same trend with increasing shear rate and time, which means the dimensions of the micro-fibres determine the anisotropy on the sub-micron scale. This microscopic anisotropy is probably also responsible for the anisotropy at the macro-scale, since a similar but weaker trend is observed in the quotient of Young's moduli. The consistency in anisotropy at different length scales thus reveals the relationship between structure and functionality,

which can assist in the more rational design of innovative food materials.

In summary, SANS combined with mechanical tests bridge the gap between the macro- and microscopic anisotropy in fibrous calcium caseinate gels. This work has also laid the foundation for characterising dense protein systems that can be explored as candidate materials for future meat analogues.

ACKNOWLEDGMENT

5

REFERENCES

[1] J. De Boer and H. Aiking, *On the merits of plant-based proteins for global food security: Marrying macro and micro perspectives,* Ecological Economics **70**, 1259 (2011).

[2] J. E. Elzerman, A. C. Hoek, M. A. Van Boekel, and P. A. Luning, *Consumer acceptance and appropriateness of meat substitutes in a meal context,* Food Quality and Preference **22**, 233 (2011).

[3] J. E. Elzerman, M. A. van Boekel, and P. A. Luning, *Exploring meat substitutes: consumer experiences and contextual factors,* British Food Journal **115**, 700 (2013).

[4] A. C. Hoek, P. A. Luning, P. Weijzen, W. Engels, F. J. Kok, and C. de Graaf, *Replacement of meat by meat substitutes. a survey on person-and product-related factors in consumer acceptance,* Appetite **56**, 662 (2011).

[5] Y. Owusu-Ansah and S. McCurdy, *Pea proteins: a review of chemistry, technology of production, and utilization,* Food Reviews International **7**, 103 (1991).

[6] A. Apichartsrangkoon, *Dynamic viscoelastic properties of heated gluten/soy protein gels,* Journal of food science **67**, 653 (2002).

[7] S. Peighambardoust, A. Van der Goot, R. Hamer, and R. Boom, *A new method to study simple shear processing of wheat gluten-starch mixtures,* Cereal chemistry **81**, 714 (2004).

[8] M. Asgar, A. Fazilah, N. Huda, R. Bhat, and A. Karim, *Nonmeat protein alternatives as meat extenders and meat analogs,* Comprehensive reviews in food science and food safety **9**, 513 (2010).

[9] M. Nieuwland, P. Geerdink, P. Brier, P. Van Den Eijnden, J. T. Henket, M. L. Langelaan, N. Stroeks, H. C. van Deventer, and A. H. Martin, *Food-grade electrospinning of proteins,* Innovative Food Science & Emerging Technologies **20**, 269 (2013).

[10] T. Finnigan, L. Needham, and C. Abbott, *Mycoprotein: a healthy new protein with a low environmental impact,* in *Sustainable protein sources* (Elsevier, 2017) pp. 305–325.

[11] B. L. Dekkers, R. Hamoen, R. M. Boom, and A. J. van der Goot, *Understanding fiber formation in a concentrated soy protein isolate-pectin blend,* Journal of Food Engineering **222**, 84 (2018).

[12] J. M. Manski, L. E. van Riemsdijk, A. J. van der Goot, and R. M. Boom, *Importance of intrinsic properties of dense caseinate dispersions for structure formation,* Biomacromolecules **8**, 3540 (2007).

[13] J. W. Fuquay, P. L. McSweeney, and P. F. Fox, *Encyclopedia of dairy sciences* (Academic Press, 2011).

[14] B. Caballero, P. Finglas, and F. Toldrá, *Encyclopedia of food and health* (Academic Press, 2015).

5

[15] J. M. Manski, A. J. van der Goot, and R. M. Boom, *Formation of fibrous materials from dense calcium caseinate dispersions,* Biomacromolecules **8**, 1271 (2007).

[16] K. J. Grabowska, A. J. van der Goot, and R. M. Boom, *Salt-modulated structure formation in a dense calcium caseinate system,* Food hydrocolloids **29**, 42 (2012).

[17] B. Tian, Z. Wang, A. J. van der Goot, and W. G. Bouwman, *Air bubbles in fibrous caseinate gels investigated by neutron refraction, x-ray tomography and refractive microscope,* Food Hydrocolloids **83**, 287 (2018).

[18] Z. Wang, B. Tian, R. Boom, and A. J. van der Goot, *Air bubbles in calcium caseinate fibrous material enhances anisotropy,* Food hydrocolloids **87**, 497 (2019).

[19] Z. Wang, B. L. Dekkers, R. Boom, and A. J. van der Goot, *Maltodextrin promotes calcium caseinate fibre formation through air inclusion,* Food Hydrocolloids **95**, 143 (2019).

[20] G. Schmidt, A. I. Nakatani, P. D. Butler, and C. C. Han, *Small-angle neutron scattering from viscoelastic polymer- clay solutions,* Macromolecules **35**, 4725 (2002).

[21] E. Ducrot, H. Montes, and C. Creton, *Structure of tough multiple network elastomers by small angle neutron scattering,* Macromolecules **48**, 7945 (2015).

[22] J. Kinney, J. Pople, G. Marshall, and S. Marshall, *Collagen orientation and crystallite size in human dentin: a small angle x-ray scattering study,* Calcified Tissue International **69**, 31 (2001).

[23] M. Martínez-Sanz, D. Mikkelsen, B. M. Flanagan, M. J. Gidley, and E. P. Gilbert, *Multi-scale characterisation of deuterated cellulose composite hydrogels reveals evidence for different interaction mechanisms with arabinoxylan, mixed-linkage glucan and xyloglucan,* Polymer **124**, 1 (2017).

[24] K. M. Weigandt, L. Porcar, and D. C. Pozzo, *In situ neutron scattering study of structural transitions in fibrin networks under shear deformation,* Soft Matter **7**, 9992 (2011).

[25] A. Lopez-Rubio and E. P. Gilbert, *Neutron scattering: a natural tool for food science and technology research,* Trends in Food Science & Technology **20**, 576 (2009).

[26] E. P. Gilbert, *Small angle x-ray and neutron scattering in food colloids,* Current Opinion in Colloid & Interface Science **42**, 55 (2019).

[27] M. Martínez-Sanz, M. J. Gidley, and E. P. Gilbert, *Application of x-ray and neutron small angle scattering techniques to study the hierarchical structure of plant cell walls: a review,* Carbohydrate polymers **125**, 120 (2015).

[28] J. Blazek and E. P. Gilbert, *Application of small-angle x-ray and neutron scattering techniques to the characterisation of starch structure: A review,* Carbohydrate Polymers **85**, 281 (2011).

[29] K. Yokoyama, T. Ohtsuka, C. Kuraishi, K. Ono, Y. Kita, T. Arakawa, and D. Ejima, *Gelation of food protein induced by recombinant microbial transglutaminase,* Journal of food Science **68**, 48 (2003).

[30] E. van der Zalm, J. Berghout, A. van der Goot, and R. Boom, *Starch–gluten separation by shearing: Influence of the device geometry,* Chemical engineering science **73**, 421 (2012).

[31] A. Van der Goot, S. Peighambardoust, C. Akkermans, and J. van Oosten-Manski, *Creating novel structures in food materials: The role of well-defined shear flow,* Food Biophysics **3**, 120 (2008).

[32] E. P. Gilbert, J. C. Schulz, and T. J. Noakes, *'quokka'—the small-angle neutron scattering instrument at opal,* Physica B: Condensed Matter **385**, 1180 (2006).

[33] K. Wood, J. P. Mata, C. J. Garvey, C.-M. Wu, W. A. Hamilton, P. Abbeywick, D. Bartlett, F. Bartsch, P. Baxter, and N. Booth, *Quokka, the pinhole small-angle neutron scattering instrument at the opal research reactor, australia: design, performance, operation and scientific highlights,* Journal of Applied Crystallography **51**, 294 (2018).

[34] A. Sokolova, A. E. Whitten, L. de Campo, J. Christoforidis, A. Eltobaji, J. Barnes, F. Darmann, and A. Berry, *Performance and characteristics of the bilby time-of-flight small-angle neutron scattering instrument,* Journal of Applied Crystallography **52** (2019).

[35] O. Arnold, J.-C. Bilheux, J. M. Borreguero, A. Buts, S. I. Campbell, L. Chapon, M. Doucet, N. Draper, R. F. Leal, M. A. Gigg, *et al.*, *Mantid—Data analysis and visualization package for neutron scattering and μ SR experiments,* Nuclear Instruments and Methods in Physics Research Section A: Accelerators, Spectrometers, Detectors and Associated Equipment **764**, 156 (2014).

[36] M. Doucet, J. Cho, G. Alina, J. Bakker, W. Bouwman, P. Butler, and e. a. Washington, A, *Sasview version 4.2.0,* http://doi.org/10.5281/zenodo.1412041 (2017).

[37] B. Hammouda, D. L. Ho, and S. Kline, *Insight into clustering in poly (ethylene oxide) solutions,* Macromolecules **37**, 6932 (2004).

[38] E. M. Saffer, M. A. Lackey, D. M. Griffin, S. Kishore, G. N. Tew, and S. R. Bhatia, *Sans study of highly resilient poly (ethylene glycol) hydrogels,* Soft Matter **10**, 1905 (2014).

[39] J. E. Curtis, A. McAuley, H. Nanda, and S. Krueger, *Protein structure and interactions in the solid state studied by small-angle neutron scattering,* Faraday discussions **158**, 285 (2012).

[40] P. H. Stothart and D. J. Cebula, *Small-angle neutron scattering study of bovine casein micelles and sub-micelles,* Journal of molecular biology **160**, 391 (1982).

[41] D. G. Dalgleish, P. A. Spagnuolo, and H. D. Goff, *A possible structure of the casein micelle based on high-resolution field-emission scanning electron microscopy,* International Dairy Journal **14**, 1025 (2004).

5

[42] B. Ingham, A. Smialowska, G. D. Erlangga, L. Matia-Merino, N. Kirby, C. Wang, R. G. Haverkamp, and A. Carr, *Revisiting the interpretation of casein micelle saxs data,* Soft Matter **12**, 6937 (2016).

[43] B. Hammouda, *A new guinier–porod model,* Journal of Applied Crystallography **43**, 716 (2010).

[44] J. Jaspe and S. J. Hagen, *Do protein molecules unfold in a simple shear flow?* Biophysical journal **91**, 3415 (2006).

[45] C. Burger, B. S. Hsiao, and B. Chu, *Preferred orientation in polymer fiber scattering,* Journal of Macromolecular Science®, Part C: Polymer Reviews **50**, 91 (2010).

[46] J. Hermans, P. Hermans, D. Vermaas, and A. Weidinger, *Quantitative evaluation of orientation in cellulose fibres from the x-ray fibre diagram,* Recueil des Travaux Chimiques des Pays-Bas **65**, 427 (1946).

[47] Z. Wang, B. Tian, R. Boom, and A. J. van der Goot, *Understanding the role of air and protein phase on mechanical anisotropy of calcium caseinate fibers,* Food Research International (2019).

[48] F. K. Schreuders, B. L. Dekkers, I. Bodnár, P. Erni, R. M. Boom, and A. J. van der Goot, *Comparing structuring potential of pea and soy protein with gluten for meat analogue preparation,* Journal of Food Engineering (2019).

[49] E. Tornberg, *Effects of heat on meat proteins–implications on structure and quality of meat products,* Meat science **70**, 493 (2005).

5

6

GENERAL DISCUSSION: APPLICATION OF NEUTRON TECHNIQUES TO THE STUDYING OF FOOD MATERIALS

From a technical point of view, the goal of this work is to introduce neutron techniques to the study of food materials, and to evaluate if they offer fresh insights into the understanding of such complex systems. A protein, calcium caseinate, is selected as the research material, as it has many fascinating properties that are worth of studying. For example, at a lower concentration, the wettability and dispersity of protein powders depend not only on the solvent but also on the drying history, such as the type of ions, the ionic strength in the solution before drying, the heating temperature and time during drying, and the type of drying methods. At a higher concentration, the pre-mixed caseinate gel can be transformed into different structures, such as a homogeneous gel, a layered gel, or a fibrous gel, depending on processing parameters. Given the diversity of research directions, different neutron techniques have been applied to calcium caseinate in different states. The main, and perhaps more easily retrievable findings are presented and analysed in details in chapters 2-5. Results that remain challenging are discussed in this chapter in forms of case studies, along with a general discussion on the implications of this work.

6.1. CASE 1: APPLICATION OF SESANS TO STUDY THE SIZE OF THE AGGREGATES IN CALCIUM CASEINATE SUSPENSIONS

The first case uses the spin-echo small angle neutron scattering (SESANS) instrument to characterise the size of the aggregates in calcium caseinate suspensions. Suspensions made from two types of calcium caseinate: the spray-dried (SCaCas) and roller-dried

(RCaCas) are measured to compare their size differences as a result of different drying methods. The concentration is 6%w/w. The depolarisation of the signal $P(z)/P_0$ is fitted by a sphere model, which writes as:

$$\frac{P(z)}{P_0} = e^{G(z)-G_0} \tag{6.1}$$

where

$$G(z) = \textbf{\textit{Real}}\left[G_0\sqrt{1-\frac{z^2}{4R^2}}\left(1+\frac{z^2}{8R^2}\right) + \frac{z^2}{2R^2}\left(1-\frac{z^2}{16R^2}\right)\ln\left(\frac{z/R}{2+\sqrt{4-\frac{z^2}{R^2}}}\right)\right] \tag{6.2}$$

$$G_0 = \frac{3}{2}\phi(1-\phi)(\Delta\rho)^2\lambda^2 tR$$

In the above equations, z is the spin-echo length, R is the radius of the aggregates, $t = 1$ cm, it is the thickness of the sample and $\lambda = 2.03$ Å, it is the wavelength of the neutron used in the measurement. The advancement of this study compares to that conducted by Tromp et al. [1] is the introduction of the parameter c, which describes the volume fraction of solvent absorbed by the protein aggregates. The reason for introducing c is that in a suspension, a number of protein aggregates are not (and probably will never be) fully dissolved, but rather swelled. The swelled aggregates and the fully dissolved particles thus render the suspension inhomogeneous. The properties of these swelled aggregates will also be different: the effective volume fraction ϕ is equal to $\phi_p(1 + c)$, where ϕ_p is the original weight fraction; the scattering length density (SLD) contrast $\Delta\rho$ equals $(\rho_{D_2O} - \rho_{protein})/(1 + c)$, where ρ_{D_2O} is the SLD of D_2O and $\rho_{protein}$ is the SLD of protein, estimated to be 2×10^{-6} Å^{-2}. From the definition of ϕ and $\Delta\rho$ it can be seen that the swelling of the protein aggregates leads to an increase in the effective volume fraction and a decrease in the SLD contrast.

Three types of size distribution are included in equations 6.1 and 6.2 when fitting the measured depolarisation. The first one describes the system in the simplest way with the least number of parameters, and assumes that the aggregates are monodisperse. However, as mentioned earlier, the suspension is inhomogeneous, so it seems unlikely that the aggregates are monodisperse. Thus, this leads to the second scenario: the radius of the aggregates R follows a log-normal distribution. In this case, $R = e^{-\frac{\ln(R-R_0)^2}{2\sigma^2}}/(R\sigma\sqrt{2\pi})$, where R_0 is the average radius, σ is the standard deviation. Given the aggregates can absorb quite some solvent and take up a larger volume, the swelled aggregates will probably interact with each other. As a result, a structure factor $S(Q)$, the Percus Yevick model describing the interaction between hard spheres, is introduced to the third scenario. It should be mentioned that the interaction between aggregates is more likely to be 'soft' than 'hard', since no oscillation pattern is observed in the depolarisation curve. Even so, the hard sphere structure factor is chosen because theories that describe the soft interaction are less known and less well-established, and it is very difficult to include polydispersity in both the form and structure factor.

The measured data and three fits are presented in Fig. 6.1, the fitted results are sum-
marised in Table 6.1. Comparing the depolarisation curves between the SCaCas and
RCaCas, it appears that the SCaCas has a more well defined turning point than the RCa-
Cas, suggesting the aggregates size is more monodisperse in the SCaCas than RCaCas.
Furthermore, the initial slope of the depolarisation is steeper in the SCaCas than RCa-
Cas, implying that the RCaCas absorbs more solvent than the SCaCas. The explanation
is that the slope equals to $\lambda^2 t (\Delta\rho)^2 \phi (1-\phi)$, which is proportional to $\dfrac{\phi_p - \phi_p^2 (1+c)}{1+c}$.
This function decreases monotonically with c, so that the steeper the slope, the smaller
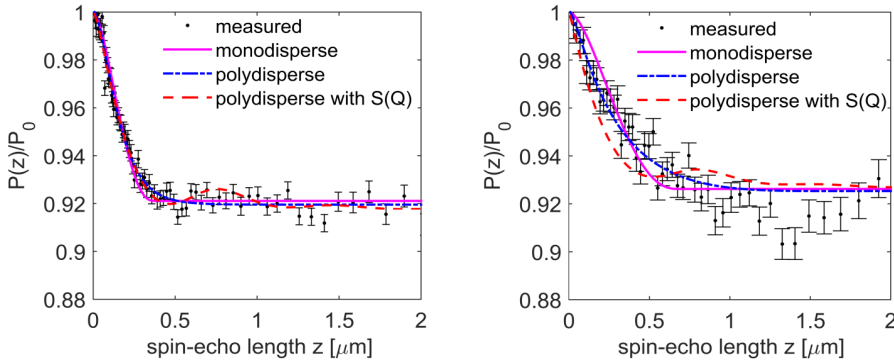the c. From Table 6.1 it can be seen that this is indeed the case.

Figure 6.1: Depolarisation of the 6%w/w spray-dried (SCaCas, left) and roller-dried (RCaCas, right) calcium
caseinate suspensions fitted with a sphere model which is monodisperse, polydisperse or polydisperse with
the Percus Yevick structure factor.

Table 6.1: Fitted parameters of R_0, c and σ assuming the aggregates are monodisperse, polydisperse or poly-
disperse with the Percus Yevick structure factor. The quality of the fits χ^2 is shown in the last column.

		R_0	c	σ	χ^2
	monodisperse	187.6±8.3	7.2±0.2	N/A	2.0
6% SCaCas	polydisperse	160.1±15.6	6.8±0.3	0.5±0.1	1.5
	polydisperse with $S(Q)$	320.1±20.4	4.7±0.2	1.1±0.2	1.7
	monodisperse	335.3±60.2	9.9±0.6	N/A	2.6
6% RCaCas	polydisperse	182.7±206.5	8.2±4.8	0.85±1.9	1.8
	polydisperse with $S(Q)$	499.7±180.8	4.8±1.1	4.5±15.1	3.5

Comparing the quality of the fits, χ^2, it seems that the polydisperse model describes both
samples the best. However, the fitted values of the 6%w/w RCaCas have too broad of a
confidence interval, which render the results less reliable. The same situation applies to
the polydisperse model with the Percus Yevick structure factor as well. The reasons are
three-fold. The first reason is the inhomogeneity of the sample. The second is because
the fitted parameters are highly correlated. The slope, turning point as well as saturation

level of the depolarisation are determined together by R_0, c and σ, according to Anders-son et al. [2]. The third reason is that the Percus Yevick model is unsuitable to describe the system, because the interaction between the aggregates is soft.
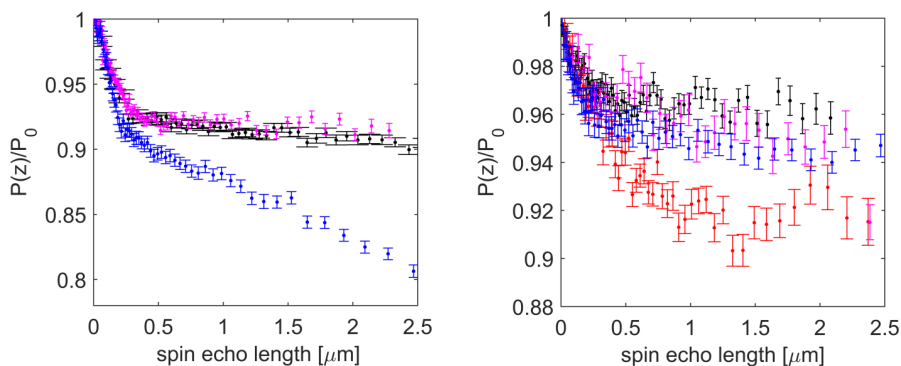

Figure 6.2: Depolarisation of the 6%w/w SCaCas (left) suspension measured in triplicate, and that of RCaCas (right) measured for four times.

Apart from the available models not being able to describe the actual state of the suspension, it also is challenging to reproduce the measured depolarisation. Two examples are given in Fig. 6.2. In the left figure, the depolarisation of one sample keeps decreasing while the others reach a plateau at ~0.4 μm, suggesting that this sample has gelled during the measurement. In the right figure, one sample reaches the plateau at a larger spin-echo length than the others, indicating that this sample contains more large, swelled aggregates. The inconsistency of the replicates comes from the fact that the caseinate powders used to make the suspension are also different. The powders are collected from multiple cows, which produce casein micelles with a different size and polydispersity [3]. Therefore, even though the samples are carefully prepared at the same condition, it is difficult to retrieve consistent results.

In summary, this case study shows that 1) while the size and amount of absorbed solvent in the protein aggregates can be well fitted, an objective description of the system depends on the choice of the right model, and this is not always readily available; 2) even though SESANS is very sensitive to the state of sample (e.g. when the system gels), it remains challenging to prepare reproducible suspensions due to the inconsistency of calcium caseinate powders. Despite the difficulty with the sample, SESANS remains a unique instrument, given that it measures the particle size at a larger length scale and covers a broad size range. It can also measure the sample without dilution, which is advantageous compared to other techniques such as dynamic light scattering (DLS), of which the measurement results can easily be disturbed by the presence of just a few large particles.

6.2. CASE 2: IN SITU STUDY OF THE STRUCTURE OF CALCIUM CASEINATE UNDER SHEAR

The fibres in calcium caseinate are formed under simple shear in an in-house developed shear device, which has aroused a lot of interest in the process happening inside the 'black box'. A versatile shear cell was built that can perform in situ measurements using either an X-ray or a neutron source [4]. To measure the structural change of calcium caseinate under simple shear, a cone plate geometry is employed so that the scattering from the velocity-vorticity plane can be probed [5].

A first attempt to measure a 30%w/w gel failed, because the motor couldn't provide sufficient torque to shear such a viscous sample. It is estimated that at least 2 N·m is needed to shear the sample, excluding 0.2 N·m of torque from the friction between seals. The concentration was consequently lowered to 15%w/w in the second attempt, along with vacuuming one inlet of the shear cell before filling in the suspension, to ensure that no air bubbles are present in the cell.
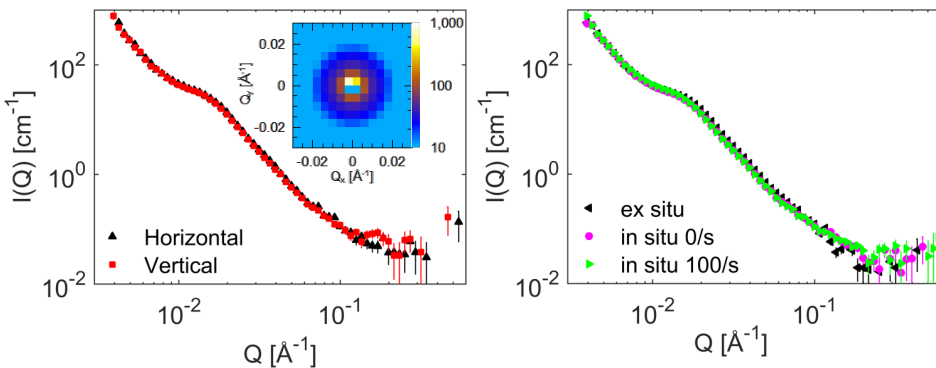

Figure 6.3: SANS data of 15%w/w SCaCas dissolved in H_2O. Left: two perpendicular sector intensities of the sample, the inset is the 2D pattern of the sample. Right: comparison of the same sample measured ex situ, in situ sheared at $0 \, s^{-1}$ and in situ sheared at $100 \, s^{-1}$.

The in situ SANS measurements were performed at the LARMOR instrument at ISIS, UK. A 15%w/w SCaCas suspension was measured at room temperature. The shear rate first increased from 0, 1, 10 to 100/s and then decreased backwards. Fig. 6.3 shows that the scattering patterns overlap between the sheared and un-sheared samples, suggesting that shear does not affect the structure of calcium caseinate. While it can be understood that shear barely influences the internal structure of protein [6], it remains curious that shear does not induce any alignment. This may be explained by the fact that a concentration of 15%w/w is too low to induce alignment, or that alignment happens at a lower Q which is out of the range of the instrument. Comparing the results to the sector intensities of a fibrous gel presented in Fig. 5.3b, it appears that the sector intensities begin to diverge within in the Q range of the LARMOR instrument, so the remaining explanation

is that the concentration is too low. Yet, it could also be interpreted as that it is easier to induce alignment at a higher Q in denser samples.

It is interesting to note that the scattering pattern of the 15%w/w SCaCas suspension is very similar to that of a 30%w/w gel presented in Fig. 5.3a, indicating that the structures of concentrated samples are reproducible. This is in contrast to the SESANS results of the 6%w/w suspension, where the reproducibility is poor.

In summary, it is currently not possible to conduct in situ measurements on the dense calcium caseinate gels, because the device could not provide sufficient torque to shear the material. Yet, given that the information obtained from in situ measurements is straightforward and may provide direct proof of the mechanism of fibre formation, it is worth investing in the design of another shear cell in the long term.

6.3. CASE 3: STRUCTURE AND ANISOTROPY OF THE FIBROUS CALCIUM CASEINATE GELS STUDIED BY USANS

Ultra-small angle neutron scattering (USANS) or SESANS are usually used in combination with SANS when the size of a structure prevails to the micrometre length scale. In this work, the scattering from fibrous calcium caseinate gels were measured by the KOOKABURRA instrument at the ANSTO OPAL reactor [7]. The principle of this instrument is based on the Bonse-Hart method [8], so that a high angular resolution can be achieved in a compact design. The resolution function of USANS is defined by a slit, which is different from SANS which is defined by a pinhole. When the scattering from a sample is isotropic, standard procedures are available to concatenate the slit-smeared USANS data with the pinhole-smeared SANS data, so that the whole scattering curve can be fitted on the absolute scale. Difficulty arises when the SANS pattern is anisotropic, because then the USANS data measured in one direction will be different from that in another direction. As a result, the standard desmearing algorithm can no longer concatenate two datasets. A recent study by Gu et al. [9, 10] proposed a method that can concatenate USANS data with azimuthal asymmetry with that from the SANS data. However, this method applies only to fractal systems, where the anisotropic sector scattering follows a simple power law. Thus, only a qualitative description of the USANS data can be provided so far.

USANS data of a fibrous sample without enzyme or air, and a sample with enzyme and air are presented in Fig. 6.4. The two samples have similar scattering patterns at high Q where the scattering intensity is higher in the vertical direction. This is in agreement with what has been observed in Fig. 5.3b and c. Thus, it can be concluded that the scattering entity in this region is a fibre. The scattering intensities keep increasing at lower Q, suggesting the presence of larger structures. It is probably the fibre bundles instead of the fibres which contribute to the scattering, given that the fibrous calcium caseinate has a hierarchical structure. At $Q \leq 0.001$ Å, the scattering curves become different between two samples. The vertical intensity in the sample without enzyme or air becomes lower than that in the horizontal direction; while it is first lower and then higher than that in
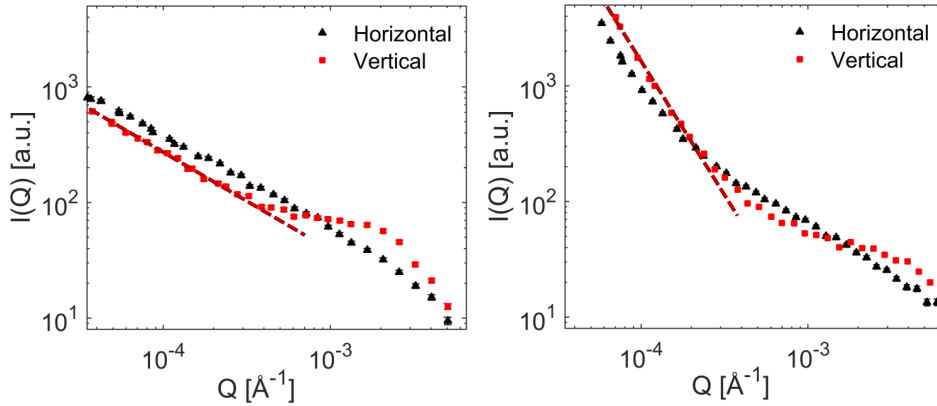
Figure 6.4: USANS data of fibrous calcium caseinate gels measured horizontally and vertically. Left: a sample without enzyme or air, sheared at 125 rpm for 5 min; Right: a sample with enzyme and air, sheared at 150 rpm for 5 min. The dashed lines are guide for the eye.

the horizontal direction for the sample with enzyme and air. Besides, the slope is steeper in the sample with enzyme and air. This is because not only fibre bundles but also air bubbles contribute to the signal, as is substantiated by the SESANS results in chapter 2, air bubbles refract the neutron beam at a larger length scale.

As food for thought, we propose a method that may help to extract quantitative information from these data. Instead of desmearing the data, we can forward calculate the scattering intensity based on a prior knowledge obtained using other techniques from this work, and then 'smear' the data to compare it with the measured USANS data. In detail, the scattering from the fibre bundles can be calculated using the anisotropic Guinier-Porod model, the sizes can be estimated from the SEM. The refraction from the air bubbles measured by USANS is a function of the distribution of the scattering angle [11] and the average number of air bubbles along the incoming beam. Smearing can be achieved by convoluting the scattering intensity with the resolution function, which is the product of the instrument resolution in the scan direction and the direction perpendicular to the scan. In this way, the smeared scattering intensity of the fibre bundles can be used to fit the measured USANS data from samples without enzyme or air, and the smeared intensity of the summed intensity from the fibre bundles and the air bubbles can be used to fit the USANS data from samples with enzyme and air.

In summary, it is obvious that the USANS data contain more valuable information than what currently can be extracted. Thus, it is worth concatenating the data with SANS. This can be achieved either by the above-mentioned method, or by developing a theory that can desmear the anisotropic sector intensity.

6.4. OUTLOOK

A summary of the neutron techniques employed in this work, based on the concentration and different states of the calcium caseinate, is presented in Fig. 6.5. At lower concentration, the system is a semi-transparent suspension. SESANS and DLS can characterise the particle/aggregates size, while SANS can provide information of the internal structure of the caseinate aggregates. As the concentration increases to 15%w/w, the suspension becomes viscous and opaque. In situ SANS measurements are conducted in an attempt to study the behaviour of the aggregates under shear. At 30%w/w, the visco-elastic calcium caseinate gel is transformed into a fibrous structure with air dispersed in it. The fibrous part can be studied by SANS together with SEM, USANS and mechanical test; while the air bubbles can be characterised by neutron refraction in combination with refractive microscopy and XRT. As concentration increases to 71%w/w, the dynamics of the hydrated caseinate powder can be probed by QENS.
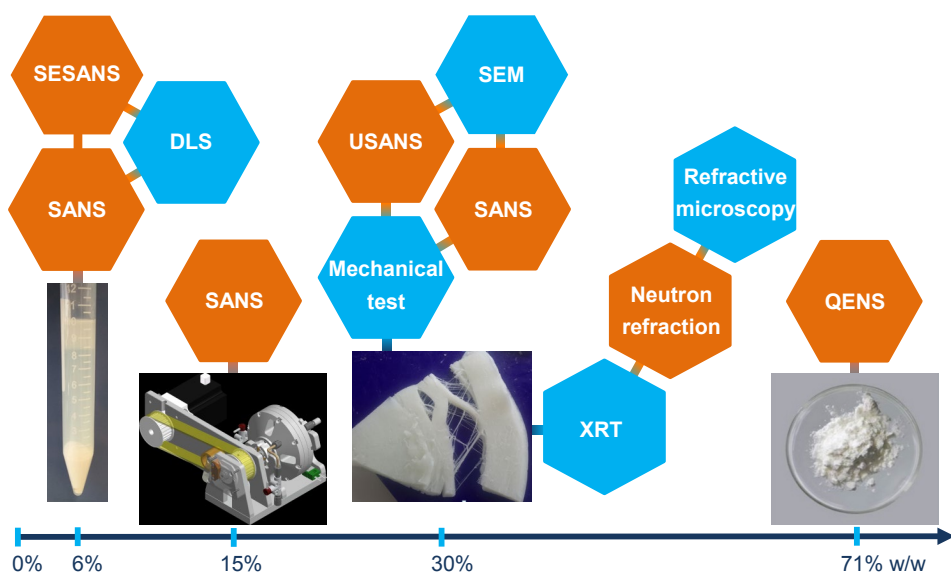

Figure 6.5: Techniques used in this work. Neutron techniques are orange hexagons while complementary techniques are blue hexagons. Techniques used in the same study are connected by strips.

This work mainly explored the application of scattering techniques on one meat analogue candidate, while there are many other neutron techniques that can be applied to study food materials. Fig. 6.6 provides an overview of the time and length scales covered by neutron and other complementary techniques, as well as their applications. Not many food-related applications can be found in the overview, which indicates on the one hand that the combination of food and neutron is still novel, and on the other hand that there is plenty of knowledge on other systems that can be transferred to the study of food materials. An outlook will be given for the continuation of this work and for other
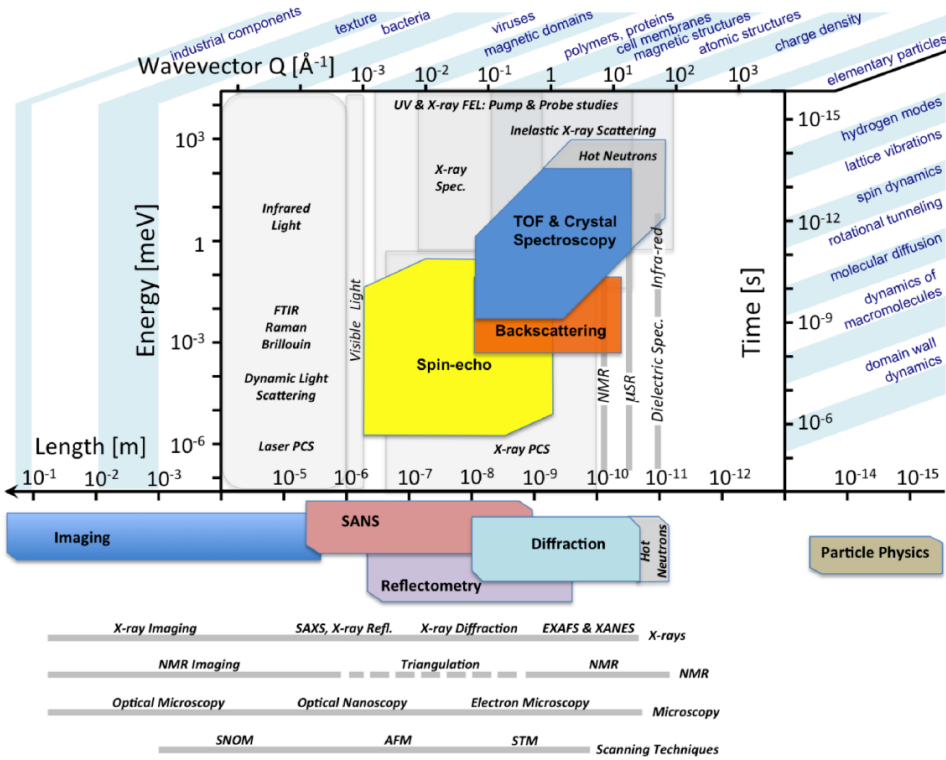
possible research directions.

Figure 6.6: An overview of the length and time scales that can be probed by neutron techniques in comparison with other techniques. Reprinted with permission from [12].

As shown in the second case study, it is not yet possible to perform in situ SANS measurements on dense calcium caseinate gels. To our knowledge, most of the rheo-cells used by neutron facilities have a Couette geometry [5], which are not suitable to measure sample displaying visco-elastic behaviour, because the sample cannot be evenly dispersed in the cell. Therefore, a rheo-cell that can provide high torque with plate-plate geometry will be more fitted to study visco-elastic materials. Information obtained from such a design is unique and may answer to fundamental questions such as the (dis)aggregation of aggregates in jammed states and their structural evolution.

Deuteration as a mean to increase contrast is regarded as a unique advantage of neutron scattering techniques in comparison to X-ray scattering. Even though it affects the structuring potential of calcium caseinate in this work, its influence on other components is allegedly less pronounced. Since carbohydrates, protein and lipids have similar chemical compositions and densities, it can sometimes be difficult to separate their effects and contributions. Deuterating one component can therefore increase the SLD

contrast so that different components in a complex matrix can be differentiated by neutrons. For instance, pectin and other polysaccharides act as a dispersed phase in soy protein based meat analogues. Adding deuterated pectin or polysaccharides to the matrix will enable the characterisation of the average size, shape and volume fraction of the dispersed phase. Another example is related to the inclusion of fat in meat analogues, as it can improve the mouth feel of the end product. The size and polydispersity of the oil droplets may be studied by SESANS when they are in deuterated forms. These quantitative results should be complementary to that obtained from confocal laser scanning microscopy (CLSM) with one phase being dyed.

Another research direction concerns exploring the dynamics of food materials using neutron techniques. Similar to QENS, the neutron spin-echo (NSE) technique can probe the dynamics of water and macromolecules at the nanosecond timescale. For instance, it can be interesting to study the dynamics of water in bound and free states as well as the type of diffusion. The results will be comparable to that obtained from nuclear magnetic resonance (NMR). The advantage of NSE over NMR is that not only a range of time scales but also a range of length scales can be measured at the same time.

6

REFERENCES

[1] R. H. Tromp and W. G. Bouwman, *A novel application of neutron scattering on dairy products,* Food Hydrocolloids **21**, 154 (2007).

[2] R. Andersson, L. F. Van Heijkamp, I. M. De Schepper, and W. G. Bouwman, *Analysis of spin-echo small-angle neutron scattering measurements,* Journal of Applied Crystallography **41**, 868 (2008).

[3] C. De Kruif and T. Huppertz, *Casein micelles: size distribution in milks from individual cows,* Journal of agricultural and food chemistry **60**, 4649 (2012).

[4] E. Velichko, B. Tian, T. Nikolaeva, J. Koning, J. van Duynhoven, and W. G. Bouwman, *A versatile shear cell for investigation of structure of food materials under shear,* Colloids and Surfaces A: Physicochemical and Engineering Aspects **566**, 21 (2019).

[5] A. P. Eberle and L. Porcar, *Flow-sans and rheo-sans applied to soft matter,* Current opinion in colloid & interface science **17**, 33 (2012).

[6] J. Jaspe and S. J. Hagen, *Do protein molecules unfold in a simple shear flow?* Biophysical journal **91**, 3415 (2006).

[7] C. Rehm, A. Brûlé, A. K. Freund, and S. J. Kennedy, *Kookaburra: the ultra-small-angle neutron scattering instrument at opal,* Journal of Applied Crystallography **46**, 1699 (2013).

[8] U. Bonse and M. Hart, *Tailless x-ray single-crystal reflection curves obtained by multiple reflection,* Applied Physics Letters **7**, 238 (1965).

[9] X. Gu and D. Mildner, *Ultra-small-angle neutron scattering with azimuthal asymmetry,* Journal of applied crystallography **49**, 934 (2016).

[10] X. Gu and D. F. Mildner, *Determination of porosity in anisotropic fractal systems by neutron scattering,* Journal of Applied Crystallography **51**, 175 (2018).

[11] V.-O. de Haan, J. Plomp, and A. A. van Well, *Real-space form factor of spherical particles in kinematic and dynamic scattering,* Journal of Applied Crystallography **40**, 756 (2007).

[12] C. Carlile, K. Andersen, and et al., *European spallation source technical design report,* `DOI:10.13140/RG.2.1.2040.6483/1` (2013).

6

SUMMARY

In the past decades, neutron scattering techniques have been applied to many soft matter systems and have yielded fruitful results that contribute to a better understanding of their properties. Yet, the techniques were rarely used for studying food materials, probably because they are less well known and less accessible to food scientists. This work fills a small part of the research gap by applying several neutron scattering techniques to the characterisation of a food-relevant protein sample: calcium caseinate. Calcium caseinate can be transformed into pronounced fibres to form the basis for a next generation meat analogue. Given the prospect of the material, the emphasis in this work is on quantifying the size, structure and dynamics of the air bubbles and fibres present in calcium caseinate gels. The main findings are summarised into four chapters.

Fibres have always been the centre of attention when characterising the structure of calcium caseinate gels, it is not until recently that the importance of air bubbles arose. These air bubbles are naturally induced during pre-mixing of a protein dispersion. Later on, depending on processing conditions, they are entrapped in the final product with a volume fraction that ranges from ~5% to ~25%. Furthermore, the shape of the air bubbles varies from spherical to prolate spheroid: the more elongated the air bubbles, the higher the mechanical anisotropy of the fibres, which suggests a relation between the elongation of the air bubbles and the anisotropy of the final product. Before a correlation is established, reliable methods that can quantify the sizes and shape of the air bubbles are in need. The neutron refraction technique, carried out by the Spin-Echo Small Angle Neutron Scattering (SESANS) instrument, is introduced for this purpose, and the main findings are summarised in chapter 2. Depolarisation due to the refraction from the air bubbles is fitted with a model, in which the shape of an air bubble is described as a cylinder with spherical end caps, based on the impression from refractive microscopy images. The average width and degree of deformation of the air bubbles can be extracted from the model. Comparing the results to that obtained from X-ray Tomography (XRT) has shown that the neutron refraction technique provides an overall description of the system: the average width and deformation degree correspond to the largest area and volume fraction of the air bubbles. It is thus concluded that the neutron refraction technique is complementary to XRT and refractive microscope.

A side effect of D_2O was discovered when it was used to increase the scattering length density contrast in chapter 2. When H_2O was replaced with D_2O during sample preparations, spray-dried calcium caseinate powders could no longer be transformed into fibres, while roller-dried powders started to form less distinctive fibres. Moreover, the deformation degree of the air bubbles is dependent on the H_2O to D_2O ratio. These observations clearly suggest the influence of D_2O on the dynamics of calcium caseinate powders, which consequently initiated the study presented in chapter 3, where the ef-

fects of isotope solvents and drying methods on fibre formation are studied by Quasi-Elastic Neutron Scattering (QENS). The IRIS instrument used in this study probes the localized motion of protein's side-groups at the picoseconds timescale. The scattering function is analysed phenomenologically. The influence of drying methods is distinguished by the trend of relaxation time with increasing temperatures. The dry spray-dried calcium caseinate powder displays a higher temperature susceptibility than the roller-dried one, suggesting shorter and milder drying processes help to preserve the activity of the protein's side-groups. By attributing the fast motion to the external, hydrophilic side-groups, and the slow motion to the solvent non-accessible, hydrophobic regions, the area fraction of the Lorentzians reveal that less mobile protons and smaller diffusion radii are available in D_2O hydrated samples, thus confirming the hydrophobic effect of D_2O. Lastly, it is found that the H_2O hydrated spray-dried calcium caseinate has a lower onset temperature of the dynamic transition, a more flexible structural conformation, and the most mobile protons. These QENS results in combination with the macroscopic observation that the H_2O hydrated spray-dried calcium caseinate also produces the most anisotropic fibres, point to a correlation between the protein dynamics on the microscopic scale and the resulting bulk structures.

Neutron scattering techniques are further applied to the characterisation of fibres in calcium caseinate gels. The fibres orient along the shear flow direction and are visible to the eye upon tearing. The degree of anisotropy is characterised by mechanical tests and varies with processing conditions. It is hypothesized that the fibres are composed of bundles of micro-fibres at the sub-micron length scale and the anisotropy of the micro-fibres is responsible for the macroscopic anisotropy. Yet, besides scanning electron microscopy (SEM) images, few methods are available to provide quantitative information on the fibres at the micro-scale. The Small Angle Neutron Scattering (SANS) technique comes in useful and yields research results presented in chapter 4 and 5. In order to analyse the elliptic scattering patterns of the fibres, an anisotropic Guinier-Porod model is constructed which forms the theme of chapter 4. This empirical model has no interference peaks, which renders it particularly useful for analysing less well defined objects without including a polydispersity index in sizes. The model is able to approximate the scattering from not only oriented cylinders, but also oriented ellipsoids, and it can distinguish well the scattering curves between the two shapes. Afterwards, a generalised form of the model is proposed, which offers the flexibility to describe the scattering from a variety of oriented objects, as long as the function which determines the transition point from the Guinier to the Porod regime is chosen carefully.

The anisotropic Guinier-Porod model provides a thorough description of the structure of the fibres which lays the foundation for chapter 5. Analysis of the sector intensity reveals that the micro-fibres are made of caseinate aggregates which are composed of smaller sphere-like particles. The resulting micro-fibres have a diameter of ~100 nm and a length of ~300 nm; the sphere-like particles have a gel mesh size of ~10 nm and can be crosslinked by the enzyme transglutaminase, which leads to stronger fibres. The addition of enzyme and air, as well as increasing shear rate and time (to a certain degree) contribute to longer and thinner fibres, which implies that the anisotropy of the

micro-fibres can be manipulated in a systematic way. By fitting the annular intensity with the Legendre polynomial, the extent of alignment of the micro-fibres is obtained. It follows the same trend as the micro-fibres' aspect ratio with varying processing parameters. Moreover, the trend of the extent of alignment is also in agreement with that obtained from the bulk mechanical tests. The consistency in trends leads to the conclusion that the fibres in calcium caseinate has a hierarchical structure, and the micro-fibres are indeed responsible for the anisotropy at the macro-scale.

In summary, through employing different neutron scattering techniques, we are able to study the sizes, structure and extent of alignment of both the air bubbles and the fibres in calcium caseinate gels; as well as the dynamics of calcium caseinate powders influenced by drying methods and isotope solvents. These studies bring a fresh view to the understanding of this meat analogue candidate, and showcase the added value of neutron scattering techniques in the study and re-design of food materials.

SAMENVATTING

In de afgelopen decennia zijn neutronenverstrooiingstechnieken toegepast op vele zachte materiesystemen en hebben vruchtbare resultaten opgeleverd die tot een beter begrip van hun eigenschappen bijdragen. Toch werden de technieken zelden gebruikt voor het bestuderen van voedselmaterialen, waarschijnlijk omdat ze minder bekend zijn en minder toegankelijk voor voedselwetenschappers. Dit werk vult een klein deel van de onderzoekskloof door verschillende neutronenverstrooiingstechnieken toe te passen bij de karakterisering van een eiwitmonster: calciumcaseïnaat. Calciumcaseïnaat kan worden omgezet in overduidelijke vezels die de basis vormen voor een volgende generatie vleesanaloog. Gezien het vooruitzicht van het materiaal ligt de nadruk in dit werk op het kwantificeren van de afmetingen, structuur en dynamiek van de luchtbellen en vezels in calciumcaseïnaatgels. De belangrijkste bevindingen zijn samengevat in vier hoofdstukken.

Vezels hebben altijd in het middelpunt van de aandacht gestaan bij het karakteriseren van de structuur van calciumcaseïnaatgels, pas sinds kort krijgt luchtbellen ook aandacht. Deze luchtbellen worden van nature geïnduceerd tijdens het voormengen van een eiwitdispersie. Later, afhankelijk van de verwerkingsomstandigheden, worden ze in het eindproduct gevangen met een volumefractie die varieert van ~5% tot ~25%. Bovendien varieert de vorm van de luchtbellen van bolvormig tot langgerekt bolvormig: hoe langgerekter de luchtbellen, hoe hoger de mechanische anisotropie van de vezels, wat een verband suggereert tussen de langgerektheid van de luchtbellen en de anisotropie van het eindproduct. Voordat een correlatie wordt vastgesteld, zijn betrouwbare methoden nodig die de grootte en vorm van de luchtbellen kunnen kwantificeren. De neutronen refractie techniek, uitgevoerd door het Spin-Echo Small Angle Neutron Scattering (SESANS) instrument, wordt voor dit doel geïntroduceerd en de belangrijkste bevindingen worden samengevat in hoofdstuk 2. Depolarisatie vanwege de breking aan de luchtbellen wordt gefit met een model, waarin de vorm van een luchtbel wordt beschreven als een cilinder met bolvormige eindkappen, gebaseerd op de indruk van brekingsmicroscopiebeelden. De gemiddelde dikte en vervormingsgraad van de luchtbellen kunnen uit het model worden gehaald. Vergelijking van de resultaten met die verkregen uit röntgentomografie (XRT) heeft aangetoond dat de neutronenbrekingstechniek een algemene beschrijving van het systeem geeft: de gemiddelde dikte en vervormingsgraad komen overeen met de grootste oppervlaktefractie en volumefractie van de luchtbellen. Er wordt dus geconcludeerd dat de neutronenbrekingstechniek complementair is aan XRT en de brekingsmicroscoop.

Een bijwerking van D_2O werd ontdekt toen het werd gebruikt om het contrast van de verstrooiingslengte-dichtheid (SLD) in hoofdstuk 2 te verhogen. Toen H_2O werd vervangen door D_2O tijdens monsterbereidingen, konden gesproeidroogde calciumcaseïnaat-

poeders niet langer in vezels worden omgezet, terwijl geroldeerde poeders enkele vezels begonnen te vormen. Bovendien is de vervormingsgraad van de luchtbellen afhankelijk van de H_2O tot D_2O verhouding. Deze waarnemingen suggereren duidelijk de invloed van D_2O op de dynamiek van calciumcaseïnaatpoeders, op grond waarvan het onderzoek in hoofdstuk 3 werd geïnitieerd, waarin de effecten van isotopische oplosmiddelen en droogmethoden op vezelvorming worden bestudeerd met Quasi-Elastische neutronenverstrooiing (QENS). Het IRIS instrument dat in deze studie wordt gebruikt, onderzoekt de gelokaliseerde beweging van de zijgroepen van eiwitten op picoseconden tijdschaal. De verstrooiingsfunctie wordt fenomenologisch geanalyseerd. De invloed van droogmethoden onderscheidt zich door de trend in relaxatietijd bij toenemende temperatuur. Het droge gesproeidroogde calciumcaseïnaatpoeder vertoont een hogere temperatuurgevoeligheid dan het geroldeerde poeder, hetgeen suggereert dat kortere en mildere droogprocessen de activiteit van de zijgroepen van het eiwit helpen te behouden. Door de snelle beweging toe te schrijven aan de externe, hydrofiele zijgroepen en de langzame beweging aan de voor oplosmiddelen niet-toegankelijke, hydrofobe zijgroepen, onthult de fractie van de Lorentzianen dat minder mobiele protonen en kleinere diffusiestralen beschikbaar zijn in D_2O gehydrateerde monsters, waarmee het hydrofobe effect van D_2O wordt bevestigd. Ten slotte wordt gevonden dat het H_2O gehydrateerde gesproeidroogde calciumcaseïnaat een lagere begintemperatuur van de dynamische overgang, een flexibelere structurele conformatie en de mobielste protonen heeft. Deze QENS resultaten in combinatie met de macroscopische waarneming dat het H_2O gehydrateerde gesproeidroogde calciumcaseïnaat ook de meest anisotrope vezels produceert, wijzen op een correlatie tussen de eiwitdynamica op microscopische schaal en de resulterende bulkstructuren.

Neutronenverstrooiingstechnieken worden verder toegepast op de karakterisering van vezels in calciumcaseïnaatgels. De vezels oriënteren zich langs de afschuifstromingsrichting en zijn met het blote oog zichtbaar bij scheuren. De mate van anisotropie wordt gekenmerkt door mechanische tests en varieert met de verwerkingsomstandigheden. De hypothese is dat de vezels samengesteld zijn uit bundels van microvezels op submicron lengteschaal en de anisotropie van de microvezels verantwoordelijk is voor de macroscopische anisotropie. Behalve scanning-elektronenmicroscopie (SEM) zijn er echter weinig methoden beschikbaar om kwantitatieve informatie over de vezels op microschaal te verschaffen. De Kleine Hoek Neutronenverstrooiingstechniek (SANS) komt van pas en levert onderzoeksresultaten op die in hoofdstuk 4 en 5 worden gepresenteerd. Om de elliptische verstrooiingspatronen van de vezels te analyseren, wordt een anisotroop Guinier-Porod model geconstrueerd dat het thema van hoofdstuk 4 vormt. Dit empirische model heeft geen interferentiepieken, wat het bijzonder nuttig maakt voor het analyseren van minder goed gedefinieerde objecten zonder een polydispersiteitsindex in afmetingen op te nemen. Het model kan de verstrooiing benaderen van niet alleen georiënteerde cilinders, maar ook georiënteerde ellipsoïden en het kan de verstrooiingscurven goed onderscheiden tussen de twee vormen. Daarna wordt een algemene vorm van het model voorgesteld die de flexibiliteit biedt om de verstrooiing van verschillende georiënteerde objecten te beschrijven, zolang de functie die het overgangspunt van het Guinier naar het Porod-regime bepaalt zorgvuldig is gekozen.

Het anisotrope Guinier-Porod model geeft een grondige beschrijving van de structuur van de vezels die de basis legt voor hoofdstuk 5. Analyse van de sectorintensiteit onthult dat de microvezels van caseïnaataggregaten zijn gemaakt die uit kleinere bolvormige deeltjes opgebouwd zijn. De resulterende microvezels hebben een diameter van ~100 nm en een lengte van ~300 nm; de bolvormige deeltjes hebben een maasgrootte van ~10 nm en kunnen worden gebonden door het enzym transglutaminase, wat leidt tot sterkere vezels. De toevoeging van enzym en lucht, evenals een toenemende afschuif-snelheid en tijd (tot op zekere hoogte) dragen bij aan langere en dunnere vezels, het-geen impliceert dat de anisotropie van de microvezels op een systematische manier kan worden gemanipuleerd. Door de ringvormige intensiteit te fitten met een Legend-repolynoom, wordt de mate van uitlijning van de microvezels verkregen. Het volgt dezelfde trend als de lengtedikteverhouding van de microvezels met verschillende ver-werkingsparameters. Bovendien is de trend van de mate van uitlijning ook in overeen-stemming met die van de bulk mechanische tests. De consistentie in trends leidt tot de conclusie dat de vezels in calciumcaseïnaat een hiërarchische structuur hebben en dat de microvezels inderdaad verantwoordelijk zijn voor de anisotropie op macroschaal.

Samenvattend kunnen we door het gebruik van verschillende neutronenverstrooiing-stechnieken de grootte, structuur en mate van uitlijning van zowel de luchtbellen als de vezels in calciumcaseïnaatgels bestuderen; evenals de dynamiek van calciumcaseï-naatpoeders beïnvloed door droogmethoden en isotoopoplosmiddelen. Deze studies geven een frisse kijk op het begrip van deze kandidaat voor vleesanaloog en tonen de toegevoegde waarde van neutronenverstrooiingstechnieken bij het bestuderen en heron-twerpen van voedingsmaterialen.

ACKNOWLEDGEMENTS

A PhD experience is certainly unique for everyone. What makes it so special to me is working with a group of physicists while I was trained to be a food scientist; this has probably hinted how extremely challenging this project has been for me, since I need to learn and use physics to solve food-related problems. Needless to say, the completion of this work wouldn't be possible without the help of many people, and I would like to take the opportunity to express my gratitude.

Firstly, I would like to thank my promoters. Wim, you have always shown great trust in me: from the moment you deemed me suitable as a PhD candidate when I literally knew nothing about neutrons until this very end. It is your trust and patience that have led me into the world of physics, where I learned to appreciate the beauty of it. What comes along with your trust is the freedom of conducting research, which I enjoyed the most of the time. On top of that, you have taught me the importance of looking at the bigger picture when I tend to be obsessed with details. Katia, your passion and dedication to science have truly fascinated me. Even though we only collaborated on one paper, I learned so much from you. Besides, you have always provided me with timely help and support when I needed it, which I am grateful for. When you're not doing science (which is rare), you are joyful, humorous and you try to take care of others, which makes me feel warm and relaxed. Atze Jan, you guided me into the world of science. Not only have you introduced this project to me, you have also encouraged me to collaborate with Fiona, which turned out to be a great idea and a success. You are always positive and supportive about our project and my work. This uplifting attitude really cheered me up when I was in self-doubt. You are also honest, insightful and practical, I feel lucky and honoured to have you as my supervisor. Morevover, I would like to thank other doctoral committee members for attending my defence: Prof. Lilia Ahrné, Prof. Bert Wolterbeek, Prof. Ekkes Brück, Dr. Victoria García-Sakai and Prof. Karen Edler, for providing me with in-depth comments on the thesis.

I've conducted many neutron experiments during the past four years, and this got me in contact with many extremely kind, skilful and patient beamline scientists. Thank you Rob Dalgliesh, Adam Washington, Sarah Rogers, Stephen King (especially for guides on SASView) and Victoria García-Sakai from ISIS; Elliot Gilbert, Liliana de Campo, Anna Sokolova and Jitendra Mata from ANSTO. I also enjoyed the beautiful scenery on the way to ISIS and the company of the sulphur-crested cockatoo on the way to ANSTO.

Next, I would like to express my thankfulness to the SSCANFoods team. Maaike Nieuwland and Margot Schooneveld-Bergmans, thank you for being interested in my research and providing me with alternative project ideas when I was stuck in the beginning. Arjen Bot, Erik van der Linden, Hans Tromp, John van Duynhoven and Paul Venema, thank

you for the critical and constructive comments, they certainly make my research more sound. Thanks Ruud den Adel for taking my samples to ESRF for measurements. Thank you Tatiana Nikolaeva, you have always been an eager and passionate team member. Thank you Kirsten Ampt for organizing the SSCANFoods meetings.

A majority of my research wouldn't be possible without having samples made and delivered by Fiona (Zhaojun Wang). You're responsible, positive and generous; on top of that, you have a true passion and tenacity for science. It has always been a pleasure collaborating with you. Evgenii, as you have mentioned in your acknowledgement, it's really necessary and lucky to have someone in the same boat for this journey. We shared many thoughts and views on not only our work but also life. Your openness to new things has inspired me to open my eyes for this world. Moreover, you always reminded me to relax and detach when I'm stressed. Lars, you're undoubtedly intelligent, thorough and kind. Thank you for helping me with neutron related topics in the beginning and comforting me when I feel down. Xinmin and Yifan, you are my closest friends at the RID. It goes without saying how much I enjoyed and needed our coffee breaks. We shared so many laughters and emotional moments, your support and understanding can literally make a bad day better, I really appreciate your company. Zhouzhou, I owe you many thanks in helping and discussing with me about neutron related works and matlab. Wenqin, I really admire your calmness and hospitality. Tiantian, thank you for dragging me to the gym, these exercises made me feel much energized afterwards. Beien, among your many talents and hobbies, I'm most impressed by your cooking skills, thank you for the delicious shumai. Apart from the people above, I would also like to acknowledge my PhD or postdoc fellows at the RID: Alexandros Vasileiadis, Anika Kiecana, Ankit Labh, Bowei Huang, Chao Wang, Eveline van der Maas, Fengqi Zhang, Guorui Zheng, Hamutu, Hanan Al-Kutubi, Huanhuan Liu, Ivan Batashev, Jurrian Bakker, Maxim Ariëns, Michael Maschek, Ming Liu, Qi Shen, Remco van der Jagt, Tammo Schwietert, Tomas Verhallen, Violetta Arszelewska, Viviam Marques Pereira, Zhaolong Li, with whom I have spent a nice lunch or coffee with.

Many colleagues from the RID have offered their help to me, which I'm thankful for. A special thanks goes to Jouke Heringa. To me, you are a treasure trove of information and I'm always amazed by the knowledge you possess. You helped me in so many aspects, from computer problems to maths problems and to the Dutch language problems, I am truly grateful for that. Besides, your patience really calmed me down when I'm stressed. Anton Lefering, you certainly have your way of doing things and it (sometimes to my surprise) works very well. You helped me multiple times with all kinds of experimental set-ups, from hydration chamber to DSC to sending the samples to Australia. You're kind at heart, which I really appreciate. Steven Parnell, thank you for proofreading my papers and chatting with me. Michel Steenvoorden and Frans Ooms, thank you for letting me use the ovens in the battery lab. Baukje Terpstra, thank you for helping me with the ICP-OES measurements. Adrie Laan and Folkert Geurink, thank you for letting me use the labs downstairs. Mehmet Sarilar, thank you for helping me with the freeze dryer. Chris Duif, thank you for the SESANS measurements. Martijn de Boer, thank you for helping me measuring the temperature of the experimental hall. Kees Goubitz, thank you for

CURRICULUM VITÆ

Bei TIAN

29-12-1989   Born in Beijing, China.

EDUCATION

2005–2008   High School Affiliated to Renmin University

2008–2012   Bachelor of Engineer in Food Science and Engineering & English
              China Agricultural University, China

2012–2014   Master of Science in Food Technology
              Wageningen University, the Netherlands

LIST OF PUBLICATIONS

9. **B. Tian**, Z. Wang, L. de Campo, E. P. Gilbert, R. M. Dalgliesh, E. Velichko, A. J. van der Goot, & W. G. Bouwman. *Small angle neutron scattering quantifies the hierarchical structure in fibrous calcium caseinate*, submitted for publication.

8. **B. Tian**, J. R. Heringa, & W. G. Bouwman. *The scattering from oriented objects analysed by the anisotropic Guinier-Porod model*, submitted for publication.

7. **B. Tian**, Z. Wang, A. J. van der Goot, & W. G. Bouwman. *Air bubbles in fibrous caseinate gels investigated by neutron refraction, X-ray tomography and refractive microscope.*, Food hydrocolloids **83**, 287-295 (2018).

6. **B. Tian**, V. G. Sakai, C. Pappas, A. J. van der Goot, & W. G. Bouwman. *Fibre formation in calcium caseinate influenced by solvent isotope effect and drying method–A neutron spectroscopy study*, Chemical Engineering Science **207**, 1270-1277 (2019).

5. Z. Wang, **B. Tian**, R. Boom, & A. J. van der Goot. *Air bubbles in calcium caseinate fibrous material enhances anisotropy*, Food hydrocolloids **87**, 497-505 (2019).

4. Z. Wang, **B. Tian**, R. Boom, & A. J. van der Goot. *Understanding the role of air and protein phase on mechanical anisotropy of calcium caseinate fibers*, Food Research International **121**, 862-869 (2019).

3. E. Velichko, **B. Tian**, T. Nikolaeva, J. Koning, J. van Duynhoven, & W. G. Bouwman, *A versatile shear cell for investigation of structure of food materials under shear*, Colloids and Surfaces A: Physicochemical and Engineering Aspects **566**, 21-28 (2019).

2. T. Nikolaeva, T. Rietkerk, A. Sein, R. Dalgliesh, W. Bouwman. E. Velichko, **B. Tian**, H. van As & J. van Duynhoven. *Impact of water degumming and enzymatic degumming on gum mesostructure formation in crude soybean oil*, Food Chemistry, in press (2019).

1. B. L. Dekkers, D. W. de Kort, J. G. Katarzyna, **B. Tian**, H. van As, & A. J. van der Goot. *A combined rheology and time domain NMR approach for determining water distributions in protein blends*, Food hydrocolloids **60**, 525-532 (2016).